Multi-spin analyses of Rotational Resonance (R^2) NMR using Rabi oscillations and Reduced Density Matrix theory

A Thesis

submitted by

SivaRanjan Uppala

for the partial fulfillment of the degree

of

Doctor of Philosophy

Department of Chemical Sciences

Indian Institute of Science Education and Research (IISER) Mohali

Knowledge city, Mohali, Punjab -140306, INDIA

October, 2016

Dedicated to my parents

and

well-wishers

Declaration

The work presented in this thesis entitled "**Multi-spin analyses of Rotational Resonance (R^2) NMR using Rabi oscillations and Reduced Density Matrix theory**" has been carried out by me under the supervision of **Dr. Ramesh Ramachandran** in the Department of Chemical Sciences, Indian Institute of Science Education and Research (IISER) Mohali.

This work has not been submitted in part or in full for a degree, a diploma, or a fellowship to any other university or institute. Whenever contributions of others are involved, every effort is made to indicate this clearly, with due acknowledgement of collaborative research and discussions. This thesis is a bonafide record of original work done by me and all sources listed within have been detailed in the bibliography.

Date: **SivaRanjan Uppala**

Place: Mohali (Candidate)

In my capacity as the supervisor of the candidate's thesis work, I certify that the above statements by the candidate are true to the best of my knowledge.

Date: **Dr. Ramesh Ramachandran**

Place: Mohali (Supervisor)

Acknowledgements

I would like to take this opportunity to acknowledge all the people who have helped, supported and motivated me directly or indirectly in shaping my career.

First of all, I would like to thank my thesis supervisor, **Dr. Ramesh Ramachandran** *who has turned out to be a good friend very soon. He is a good teacher, a well wisher and a person who is passionate to do science. I have learned his way of looking at the problem in a positive approach which instantly solves half of it right away. I am thankful to him for stimulating discussions both in scientific and non-scientific fields throughout my Ph.D career. In particular, I must thank him for his patience in bearing my non-academic activities even under a lot of pressure.*

I am grateful to my Doctoral committee members, **Prof. Viswanathan** *and* **Dr. Shamasunder** *for their valuable suggestions.*

I sincerely thank **Prof. Sathyamurthy**, *Director, IISER Mohali for providing all the facilities and I am pleased with his support during my partial struggle to bring good research life for all the scholars.*

I am thankful to IISER Mohali and DST India for providing the financial support during my Ph.D. Here, I must acknowledge the informatics center at IISER Mohali for providing both the library and computer facilities.

I deeply acknowledge **Dr. Bapaiah** *and* **Dr. Visakhi** *for their love and affection towards us and for creating such a beautiful atmosphere in different occasions.*

I would love to acknowledge **Dr. Manoj Kumar** *for his valuable academic support in early days of my research. I appreciate his patience and passion that are required to pursue research.*

I would miss those wonderful days with my colleagues **Subba Rao, Zeba Qadri** *and* **Vinay Ganapathy**. *They have created a fair and healthy atmosphere in our lab. I thank all my other colleagues* **Deepansh, Rajat Garg, Bharti, Manpreet,**

Lakshmi, Justin *and* **Shreyan Ganguly** *for being a part of those wonderful moments.*

When it comes to non-academics, I would be happy to recollect all those joyful days with my friends **Rajesh babu, Billa Prashanth, Raj Kumar, Kiran Kumar, Sai kumar, Satya Prakash, Praphulla, B. T. Raman, C. K. Reddy, Rama Rao, Krishna, Gayathri and Ranjit** *and their help to refresh myself.*

Since, It is difficult to find words to acknowledge **My parents**, *I simply thank them for giving me what not at the expense of their freedom and happy moments in their life. I am sure that their hard work in getting the desired things really inspired me and made me to choose the same path. I thank my loving brother,* **Vidya Sagar** *for his continuous moral support. I would love to express my gratitude to my wife,* **Triveni** *for her patience and for providing a peaceful atmosphere to focus on my work in the ending days of my Ph.D.*

IISER Mohali students and all the scholars from different parts of India, for their physical and moral support in various issues for bringing better research life to all the research scholars.

Last but not least, I remember all **my teachers** *in this happy moment for their teachings that motivated me to pursue Science.*

List of Figures

List of Tables

Notations

I	Spin quantum number
h	Planck's constant
γ	Gyromagnetic ratio
$\|Im\rangle$	Ket Eigen basis
I_x, I_y, I_z	Spin angular momentum operators
I^+, I^-	Lowering and Raising operators
ρ	Density matrix /operator
ψ	Wave function
Tr	Trace of matrix
$\left\langle \hat{O}_P \right\rangle$	Expectation value of an observable
τ_{mix}	Mixing-time
i	Iota
$\rho(0)$	Initial density operator
$\rho(t)$	Evolved density operator
ω_0	Larmor frequency
B_0	Strength of static magnetic field
υ_R	Spinning frequency
ω_{RF}	Amplitude of oscillating RF field
ω_m	Modulation frequency
${\omega_I}^{(0)}$	Isotropic chemical-shift
CSA	Chemical shift anisotropy
δ	Magnitude of Chemical-shift anisotropy
${\omega_I}^{(m)}$	Chemical-shift anisotropy in powder sample
$T^{(k)q}$	Spin Tensor
$R^{(k)-q}$	Spatial Tensor
ω_{ij}	Dipolar constant
RF	Radio frequency (Oscillating magnetic field)
MAS	Magic angle spinning
H	Hamiltonian
U	Unitary transformation

k	Rank
q	Component
$H_0^{(1)}, H_1^{(1)}, H_2^{(1)}$	Zeroth, 1st, 2nd, order Hamiltonians respectively, after first Transformation
$H_0^{(2)}, H_1^{(2)}, H_2^{(2)}$	Zeroth, 1st, 2nd, order Hamiltonians respectively, after second Transformation
S_1	Transformation function
H_{iso}	Isotropic Hamiltonian
H_{anioso}	Anisotropic Hamiltonian
H_d	Diagonal Hamiltonian
H_{od}	Off-diagonal Hamiltonian
H_F	Floquet Hamiltonian
H_{eff}	Effective Hamiltonian
^1H	NMR active isotope of Proton (I=1/2)
^{13}C	NMR active isotope of Carbon (I=1/2)
DQ	Double quantum
ZQ	Zero quantum
PAS	Principle Axis System
LAS	Lab Axis System
$MolAS$	Molecular Axis System
RAS	Rotor Axis System
BCH	Baber-Campbel-Hausderff expansion
$SSNMR$	Solid-state NMR
R^2	Rotational Resonance
CP	Cross-polarization
CW	Continuous wave
$TPPM$	Two-pulse phase modulation

Contents

Abstract

An analytic framework integrating the concept of effective Hamiltonians and Reduced density matrix theory is proposed for describing polarization transfer in solid-state NMR. Specifically, the magnetization exchange between ^{13}C nuclei in Rotational Resonance (R^2) experiments is described in the presence of coupling to protons reservoir. The factors responsible for depolarization in R^2 experiments and the role of heteronuclear decoupling schemes during the dipolar mixing are thoroughly investigated. Additionally, implementation of fractional R^2 experiments are discussed. The simulations emerging from the proposed analytic model are well substantiated through simulations emerging from exact numerical methods. The framework presented in the thesis is well-suited for describing both homonuclear and heteronuclear experiments in solid-state NMR.

Chapter 1

Introduction

1.1 Background

Although from a historical perspective, the phenomenon of nuclear magnetic resonance originated from the pioneering experiments of Rabi[1] in 1936 and culminated in the design of the NMR spectrometer in 1946[2,3], from an experimental perspective, the genesis of solid-state nuclear magnetic resonance (SSNMR) spectroscopy began only in 1958 through the discovery of Magic Angle Spinning[4,5] (MAS) experiment. In contrast to solution NMR spectroscopy, the NMR spectra in the solid-state are broadened by the anisotropic nature of the spin interactions. To overcome the spatial anisotropy imposed by the inherent restricted mobility, Andrew et al.[4] and Lowe,[5] independently proposed an ingenious approach of mechanically rotating the sample along an axis inclined at an angle 54.7° with respect to the static magnetic field. The resulting NMR spectrum under sample spinning comprises of a center-band (at frequency ω_0, determined by the isotropic parts of the spin interactions) and a series of spinning sidebands (due to anisotropic part) disposed symmetrically with respect to the center-band at integer multiples of the spinning frequency[6–8]. With increase in the spinning frequency, the anisotropic parts of the interactions get more or less averaged resulting in isotropic liquid like spectrum. In combination with the cross-polarization[9] (CP) technique, CP-MAS[10] experiments along with multiple-pulse based heteronuclear decoupling[8,11–27] methods have become an integral building block in the study of less-abundant nuclei. Nevertheless, it was soon realized that the improved spectral resolution afforded by MAS arises at the expense of the structural

information inherent in the anisotropic interactions (i.e. the anisotropic interactions get wiped out under spinning conditions). In particular, the detection of through-space contacts, which presents an attractive option to probe structural parameters in the solid-state, is averaged under MAS. Unlike solution NMR spectroscopy, where the measurement of the Overhauser effect[28] between neighboring nuclei (usually ^1H) provides the desired constraints to determine the molecular structure, the dipolar interactions in the solid-state encode the spatial information and play a central role both in the spectral assignments as well as in experiments that involve measurement of interatomic distances. Hence, reintroduction of dipolar interactions (both homonuclear and heteronuclear) under MAS conditions has remained the major emphasize in the last couple of decades.

Employing sophisticated multiple-pulse schemes (commonly referred to as dipolar recoupling experiments[29–35]), the averaging effect of MAS is partially compensated during the dipolar mixing time. Subsequently, the dipolar interactions are reintroduced under MAS conditions in a controlled fashion depending on their role in SSNMR experiments. For e.g, in the case of spectral assignment studies, the local connectivity (or correlation) between different nuclei is established through broadband dipolar recoupling sequences (all the dipolar interactions in a system are reintroduced simultaneously). By contrast, in selective dipolar recoupling methods, the dipolar interactions are reintroduced in a controlled fashion (between spin pair) and are primarily designed for measuring interatomic distances. Here in this thesis, we confine our discussion to homonuclear dipolar recoupling methods tailored towards the measurement of interatomic distances in solid samples. In particular, we restrict our attention to Rotational Resonance (R^2) experiments in solid-state NMR.

After the successful design of MAS experiments in 1958, Andrew and coworkers[36,37] reported (in 1963) an interesting effect relating the spectral line broadening and sample spinning frequency in MAS experiments. Specifically, when the sample spinning frequency (or integral multiples of it) is adjusted to match the isotropic chemical shift difference between a pair of nuclei, distorted line-shapes (corresponding to that particular pair of resonances) along with line broadening were observed. This condition is commonly referred to as the Rotational Resonance (R^2) condition in SSNMR experiments. Due to the presence of intermolecular spin interactions (^{31}P, 100% natural abundance), the distortions in the line-shape reported by Andrew et al. could

never be quantified. To address this issue, Griffin and co-workers[38–40] introduced the concept of employing labeled (^{13}C) spin pair samples (diluted in natural abundance to minimize intermolecular effects) to mimic an isolated homonuclear spin pair system. As reported earlier,[37] the resonances corresponding to the selected spin pair were broadened under Rotational Resonance (R^2) conditions (i.e. $|\upsilon_1 - \upsilon_2| = N\upsilon_R$). Since dipolar interactions were responsible for the observed broadening in the spectrum, it was realized that the R^2 experiment[41] could serve as a method for extracting interatomic distances in solid-state NMR.[42–44] To achieve this objective, monitoring the magnetization exchange between a pair of ^{13}C nuclei was employed as a strategy for extracting internuclear distance information in R^2 experiments. In a typical longitudinal magnetization exchange experiment, an initial state of difference polarization is prepared along the rotating frame z-axis, and the time-evolution of this state is examined as a function of the dipolar mixing time.

Very often, the magnetization exchange trajectory resulting from such experiments depend on several parameters that includes the dipolar coupling constant, the orientation dependence arising from the chemical shift tensors in addition to the undesired residual heteronuclear dipolar interactions (say ^{13}C-^{1}H) resulting from insufficient decoupling. Subsequently, to minimize the complexity in the data analysis, a phenomenological damping constant[45] (zero-quantum relaxation, T_{ZQ}) was employed to fit the experimental magnetization exchange trajectories in R^2 experiments. Under idealized conditions (in cases where the chemical shift tensors are known), the dipolar coupling constant along with the damping constant were employed to fit parameters required to fit the experimental trajectories. Employing this approach, $^{13}C - {}^{13}C$ distance information in the strong and intermediate coupling regimes were obtained in wide range of systems through selective labeling. Nevertheless, the extension of the R^2 method for extracting distances in the weak coupling limit is less straight forward owing to the uncertainties involved in the data analysis[46,47].

As an alternative, Costa et al.[48] proposed the rotational resonance width (R^2W) experiments to improve the accuracy of the distances estimated from R^2 experiments. In contrast to the standard mixing time experiments, the magnetization exchange in R^2W experiments were monitored as a function of the spinning frequency under constant mixing times. Employing this approach, interatomic distances in selectively labeled samples were extracted both in the weak and strong coupling regimes with im-

proved accuracy. Since extensions in larger biological systems entail the measurement of multiple constraints ($^{13}C-{}^{13}C$ and $^{13}C-{}^{15}N$ distances), the R^2W approach was subsequently integrated with two-dimensional spectroscopy for measuring multiple $^{13}C-{}^{13}C$ distance constraints in a uniformly ^{13}C, ^{15}N - labeled dipeptide.[46] Since then, rotational resonance based experiments[47,49–52] have almost become a routine for measuring $^{13}C-{}^{13}C$ distances in biological systems ranging from simple peptides[46,47,49,51] to membrane proteins.[50,52] While these experiments have found utility in the study of larger biological systems, the reliability of the constraints estimated through theoretical models based on two-spin framework (inclusive of phenomenological damping terms) deserves a careful review.

As the number of measurable constraints available in the solid state is inherently limited by resolution, the fitting of the R^2 experimental data (in the weak-coupling regime) becomes important in studies involving larger biological systems. To this end, Meier and coworkers[53] proposed an effective two-spin model that includes the dipolar coupling of interest, zero-quantum relaxation rate in addition to a phenomenological offset to account for the strongly coupled surrounding environment. In an alternate formulation, Baldus and coworkers[54] proposed the multi-spin (MS) analysis approach based on numerical methods for describing the effects of protons in R^2 experiments. Employing approximate molecular geometry (in the form of $^{13}C-{}^{1}H$ distance information), the experimental data for a given system was simulated with the dipolar coupling constant as a free-fit parameter. Although, their studies reveal the importance of neighboring protons on the exchange dynamics, the implementation of the MS analysis is time consuming and less insightful.

In a contrasting attempt, Ladizhansky and co-workers[51] demonstrated the measurement of $^{13}C-{}^{13}C$ distances in polypeptides and membrane proteins[52] using homogeneously broadened R^2 conditions. Employing moderate decoupling field strengths on the proton channel, the R^2 matching conditions were broadened and the resulting trajectories were simulated using the standard two-spin approach (inclusive of the phenomenological damping term). Interestingly, the magnitude of the damping terms employed in their studies were significantly higher in comparison to earlier studies on similar systems under identical experimental conditions.[47] This variation in the magnitude of the damping terms was also corroborated in a recent theoretical study by Ramachandran and co-workers.[55] Hence, an alternate analytic theory is indispens-

able for resolving the conflicting results reported in the literature with regard to the mode of inclusion /role of $^{13}C-{}^{1}H$ dipolar interactions in the R^2 experimental data analysis.

From a theoretical stand point, analytic description of multi-spin effects[56,57] observed in NMR experiments have always been fraught with difficulty, owing to (a) the presence of time-dependent interactions (b) the dimension of the spin system. For e.g., in the state space description[58] of the spin dynamics, the density operator is described in a vector space of dimension 2^M (where 'M' denotes the number of spins (I=1/2) present in the system), while in the operator space (or Liouville space) description, the density operator is expanded and expressed in terms of 2^{2M} operators defined in a vector space of dimension 2^{2M}. Hence, the dimensionality of the problem increases with the number of spins both in the state and operator space description of the spin dynamics. Additionally, the spin Hamiltonians in multiple-pulse based MAS experiments have complicated time-dependence owing to the simultaneous presence of sample rotation and RF pulses.

As an alternative to these treatments, an analytic theory combining the effective Hamiltonian approach with the concept of reduced density matrix[59,60] is proposed to elucidate the effects of protons in R^2 dynamics. The approach presented in the thesis is quite general and is suitable for describing both homonuclear and heteronuclear recoupling experiments in SSNMR. In the proposed method, effective Hamiltonians[61,62] to the desired order (say second-order) are derived utilizing the contact transformation procedure.[63,64] To circumvent the complexities involved in the multi-spin analysis of R^2 experimental data, effective Hamiltonian based Reduced density matrices[60] are proposed for describing the polarization transfer observed in R^2 experiments. Employing this formalism, the polarization transfer observed in R^2 experiments is described in terms of single-spin density matrices. The coupling with the proton reservoir is incorporated through the effective Hamiltonians and is included in the derivation of the density matrices for individual spins. The analytic results emerging from the proposed approach are computationally less intensive and are quite useful in the fitting of experimental trajectories. Employing suitable model systems and interaction parameters, the polarization transfer in R^2 experiments is studied theoretically and the results emerging from the analytic theory are compared and verified with simulations emerging from exact numerical methods[65,66]. A brief outline of the

thesis is presented in the following sections.

1.2 Objectives and Motivation

To determine the 3D-structure of a system, measurement of interatomic distances remain vital. In this regard, the R^2 experiment remains the only reliable technique in SSNMR for measuring $^{13}C - {}^{13}C$ distances in uniformly labeled solids. Although, many theoretical formalisms do exist in the literature,[45,47,54,55] the following issues often remain unaddressed: (i) the physical basis of phenomenological damping terms (ii) role of heteronuclear dipolar interactions and decoupling sequences during R^2 mixing times (iii) multi-spin contributions resulting from overlapping R^2 matching conditions between different spin pairs. Since the number of constraints that are available in the solid-state are limited by the resolution factor, the accuracy of the estimated constraints become very crucial in the overall refinement of the 3D-structure. From a theoretical standpoint, interpretation (or fitting) of the magnetization exchange trajectories are complicated by the presence of both the spin interactions of the system of interest as well as its coupling to the neighboring proton reservoir. Since the number of fit parameters increase with the spin system, phenomenological models have become the method of choice to minimize the computational time in such studies. As described in the previous section, the validity of such models deserve a thorough review before it becomes operationally valid. To this end, the following problems are addressed in this thesis:

1. An intuitive analytic model based on the concept of reduced density matrix is proposed for describing the magnetization exchange in R^2 experiments.

2. Employing a model system comprising of N-protons, the effect of $^{13}C - {}^{1}H$ dipolar interactions in R^2 experiments is discussed.

3. Derivation of higher order /fractional R^2 conditions in solid-state NMR experiments.

In the following section, the general methodology adopted in this thesis is outlined with few illustrative examples.

1.3 Methodology

In quantum mechanics, description of an experimental phenomenon entails the presence of a framework wherein the states of the physical system are described through parameters that are logically consistent and are of operational significance. Since measurements in NMR spectroscopy are made on bulk samples (or large collection of identical quantum mechanical systems), the density matrix formalism has remained the preferred approach for studying the dynamics of spins.

Accordingly, the state of a system is described in terms of the density operator, $\rho(t)$ and the time-evolution of the system is studied through the Quantum-Liouville equation.

$$i\hbar\frac{d\rho(t)}{dt} = [H(t), \rho(t)] \tag{1.1}$$

$$\rho(t) = e^{-\frac{i}{\hbar}\int_0^t H(t')dt'}\rho(0)e^{\frac{i}{\hbar}\int_0^t H(t')dt'} \tag{1.2}$$

In this thesis, we confine our discussion to the NMR experiments in the solid-state. In contrast to solution NMR spectroscopy, the spin Hamiltonians in SSNMR are time-dependent both due to sample rotation as well as RF irradiation. To facilitate analytic description of the spin dynamics involving time-dependent Hamiltonians, effective Hamiltonians[61,62] based on the Floquet theory[67–75] and the contact transformation methods[63,64] have been proposed in the past to describe the experiments[47] in solid-state NMR.

$$i\hbar\frac{d\rho(t)}{dt} = [H_{eff}, \rho(t)] \tag{1.3}$$

$$\rho(t) = e^{-\frac{i}{\hbar}H_{eff}t}\rho(0)e^{\frac{i}{\hbar}H_{eff}t} \tag{1.4}$$

In spite of this accomplishment, the density operator formalism remains less suitable for analytic description beyond two-spins. To overcome this limitation, we propose a solution that is built on the concepts of reduced density matrices and effective Hamiltonians.

In the reduced density matrix formalism[59], the system of interest (ψ) is constructed by the partial trace operation over all the unobserved spin variables (ϕ) present in the combined system, $\rho(t)$ (i.e., by taking the matrix elements of the total density matrix which are diagonal in the unobserved variable 'i' and summing these elements over all 'i'). The reduced density matrix, $\rho(\psi, t)$ and its elements are defined

by,

$$\langle\psi_{j'}|\,\rho(\psi,t)\,|\psi_j\rangle = \sum_i \langle\phi_i\psi_{j'}|\,\rho(t)\,|\phi_i\psi_j\rangle \tag{1.5}$$

Subsequently, the observable associated with the system of interest is calculated through single-spin density matrices as given below.

$$\langle O_p(t)\rangle = \mathrm{Tr}\,\{\rho(\psi,t)O_p\} \tag{1.6}$$

In the following sections, the utility of the reduced density matrix formalism is discussed through some known examples in the literature.

1.4 Spin interactions in NMR

To extract molecular information in NMR experiments, it is important to have a description, wherein, the evolution of the system solely guided by its own internal Hamiltonian. From a mathematical standpoint, this is accomplished through the rotating wave approximation (RWA) of Rabi. In RWA of Rabi, the internal Hamiltonians are transformed into an interaction defined by the dominant terms (Zeeman term) present in the external Hamiltonian. In this new frame, the contributions from the Zeeman interaction are absent and the terms that commute with H_Z are retained (commonly referred to as high field approximation). The Zeeman interaction represents the interaction between the nuclear spin magnetic moment and the static magnetic field and is quantum mechanically represented through the Zeeman Hamiltonian, H_Z.

$$H_Z = -\mu_z B_0 = -\hbar\gamma I_z B_0 = -\hbar\omega_0 I_z \tag{1.7}$$

where μ is the magnetic moment, $\hbar$ is the plank's constant divided by 2π, γ is the gyromagnetic ratio, B_0 is the strength of the static magnetic field and ω_0 is the Larmor frequency.

In a similar vein, the interaction of the nuclear spin with the oscillating magnetic field applied (along the x-direction) is represented through the RF Hamiltonian given below,

$$H_{RF}(t) = -2\hbar\gamma B_1 \cos(\omega_{ref}t + \phi)I_x = -2\hbar\omega_1 \cos(\omega_{ref}t + \phi)I_x \tag{1.8}$$

where $\omega_1 = \gamma B_1$ is the nutation frequency of the RF field and ϕ is the phase. Depending upon the amplitude of RF field and its duration, the excitation band width is classified into broadband (shorter duration) and selective (longer duration).

The chemical shift interaction depicts the interaction between the nuclear spin magnetic moment mediated through the surrounding electronic cloud (environment). In a typical liquid sample, the chemical shift interaction is represented by a scalar quantity and is purely isotropic.

$$H_{iso} = -\hbar\Delta\omega I_z \tag{1.9}$$

where, $\Delta\omega$ denotes the offset frequency.

In the case of solids (or polycrystalline samples), the chemical shift interaction is orientation dependent and is characterized by the anisotropy as well as the asymmetry parameter.

$$H_{cs}(t) = H_{iso} + H_{aniso}(t) \tag{1.10}$$

Under MAS conditions, the anisotropic part of the chemical shift interaction is time-dependent.

$$H_{aniso}(t) = H_{CSA}(t) = \sum_{m=-2,m\neq 0}^{2} \omega_i^{(m)} e^{im\omega_r t} I_z \tag{1.11}$$

where ω_r is the spinning frequency of the sample. The time-dependent components of the chemical shift anisotropy (CSA) interactions are represented by

$$\omega_i^{(m)} = \sum_{m_1,m_2,m=-2}^{2} R_{cs,PAS}^{(2)m_1}.D_{m_1m_2}(\Omega_{PM}).D_{m_2m}(\Omega_{MR}).d_{m0}(\beta_m) \tag{1.12}$$

with β_m denoting the magic angle.

In the above equation, $R_{cs,PAS}^{(2)m_1}$ denotes the irreducible spatial tensor defined in the PAS ($R_{csa,PAS}^{(2)0} = \delta_{aniso}$ and $R_{csa,PAS}^{(2)\pm 2} = -\frac{1}{\sqrt{6}}\delta_{aniso}\eta$ where δ_{aniso} and η are anisotropy and asymmetry parameters respectively). $D(\Omega)$ represents the Wigner rotation matrix[76] with rank=2 and Ω, the set of Euler angles employed in the transformation from the Principal axis system (PAS) to the Lab frame. A more detailed description of these interactions are well documented in literature[7,8] and have been consciously omitted in this thesis to avoid repetition.

The interaction between nuclei are often pairwise and take place either through bond or through space. Due to inherent tumbling motion, the through space interactions are generally averaged (to first order) in liquids. By contrast, the restricted mobility in the solid-state renders the through space interaction anisotropic. In MAS

experiments, the dipolar Hamiltonian is time-dependent and is represented by,

$$H_d(t) = \sum_{m=-2,m\neq 0}^{2} \omega_{12}^{(m)} e^{im\omega_r t} \left[2I_{1z}I_{2z} - \frac{1}{2}\left(I_1^+ I_2^- + I_1^- I_2^+\right)\right] \tag{1.13}$$

Analogous to the CSA interactions, the anisotropic components of the dipolar interactions are represented through Wigner rotation matrices.

$$\omega_{12}^{(m)} = \sum_{m_1,m_2,m=-2}^{2} R_{D,PAS,12}^{(2)0}.D_{0m_2}(\Omega_{PM}).D_{m_2m}(\Omega_{MR}).d_{m0}(\beta_m) \tag{1.14}$$

The only non-zero term, $R_{D,PAS,12}^{(2)0} = \sqrt{6}b_{12}(b_{12} = \mu_0\gamma_1\gamma_2\hbar/4\pi|\vec{r}_{12}|^3$ (rad/s) is the dipolar coupling constant) represents the spatial tensor in the dipolar PAS. In the case of heteronuclear dipolar interactions, the flip-flop operators in the above Hamiltonian are ignored under secular approximation.

As described in Eq. (1.2), when the Hamiltonian is time-independent, the solution to the quantum-Liouville equation reduces to a simpler form.

$$\rho(t) = e^{-\frac{i}{\hbar}Ht}\rho(0)e^{\frac{i}{\hbar}Ht} \tag{1.15}$$

with $\rho(0)$ denoting the density operator at time, $t = 0$.

Since the Hamiltonians under MAS are time-dependent, the evaluation of the density operator gets complicated. In the numerical based approaches, the evolution of a system under a time-dependent Hamiltonian is split and expressed as a product through approximate time-independent Hamiltonians. Although, such methods are computationally feasible, they are less insightful with regard to providing analytic insights into the spin dynamics.

To this end, analytic methods based on AHT[6,77,78] and Floquet theory[67–75] have formed extensive utility in the design and interpretation of experiments in SSNMR. Although, such approaches have improved our understanding of the spin dynamics, analytic description beyond two-spin framework has remained elusive.

In the state-space description of the spin dynamics, the density operator is expressed in terms of a matrix spanned by the number of spin basis states. For a system composed of 'N' coupled spin I=1/2 nuclei, the combined density matrix is constructed from the direct product between individual spin density matrices.

$$\rho = \rho_1 \otimes \rho_2 ..... \otimes \rho_N \tag{1.16}$$

In the above equation, ρ denotes the density operator for the combined system (2^N x 2^N) and ρ_N, the individual spin density matrix (2x2). In the $|Im\rangle$ basis, the density matrix for a single spin I=1/2 is represented by,

$$\begin{pmatrix} \rho_{\alpha,\alpha}(t) & \rho_{\alpha,\beta}(t) \\ \rho_{\beta,\alpha}(t) & \rho_{\beta,\beta}(t) \end{pmatrix} \tag{1.17}$$

with

$$\rho_{\alpha,\beta}(t) = \langle\alpha| e^{-\frac{i}{\hbar}Ht}\rho(0)e^{\frac{i}{\hbar}Ht} |\beta\rangle \tag{1.18}$$

representing the element of the density matrix at some arbitrary time 't' and H, the Hamiltonian of the spin system.

As depicted above, the dimension of the problem increases with the number of spins and limits the utility of the method beyond the isolated two-spin framework. By contrast, in the operator-space (or Liouville space) description of the spin dynamics, the density operator is expressed in terms of operators. For a composite system comprising of N spin I=1/2 nuclei, the density matrix is expressed in terms of 4^N operators. Subsequently, the time-evolution is described through a set of rate equations corresponding to the operators employed in the expansion of the density matrix. Consequently, analytic description of the spin dynamics gets intractable (both in the state as well as in the operator space) with the increase in the number of spins. To overcome this limitation, a solution built on the concepts of reduced density matrices and effective Hamiltonians is proposed in this thesis.

1.5 Reduced density matrix

To describe the utility of the reduced density matrix approach, we begin our discussion with a composite system comprising of two subsystems, with 'ψ' representing the subsystem of interest and 'ϕ' the other undetected /unobserved system. Let us assume that there exists some interaction between the two subsystems (or equally that the systems have interacted in the past) such that the system of interest is often in some mixed state. The states of the composite system are expressed in terms of the direct product between the basis states of the two subsystems. Employing the combined basis states, the elements of the composite density operator are constructed

as represented below.

$$\langle \Phi_{i'}\psi_{j'}|\, I(\psi)\, |\Phi_i\psi_j\rangle = \langle \psi_{j'}|\, I(\psi)\, |\psi_j\rangle \cdot \delta_{i'i} \tag{1.19}$$

Our objective in this exercise is to reconstruct the density matrix of the system of interest from the composite system. To evaluate the reduced density matrix of the system of interest, the initial step involves the evaluation of the density operator of the composite system governed by some Hamiltonian, at time 't'. Following this procedure, the reduced density matrix for the desired system is calculated by projecting the combined density matrix into the subspace of interest. In general, the reduced density matrix[59] for a given system of interest is constructed by the partial trace operation over all the unobserved spin variables present in the combined system (i.e., by taking the matrix elements of the total density matrix which are diagonal in the unobserved variable 'i' and summing these elements over all 'i'). As described earlier, the expectation value is evaluated by the following procedure.

$$\begin{aligned}
\langle I(\psi,t)\rangle =& \mathrm{Tr}\left[\rho(t)I(\psi)\right] \\
=& \sum_{i'ij'j} \langle \Phi_{i'}\psi_{j'}|\rho(t)\,|\Phi_i\psi_j\rangle\langle\Phi_i\psi_j|I(\psi)\,|\Phi_{i'}\psi_{j'}\rangle \\
=& \sum_{j'j}\left[\sum_i \langle\Phi_i\psi_{j'}|\rho(t)\,|\Phi_i\psi_j\rangle\right]\langle\psi_j|I(\psi)\,|\psi_{j'}\rangle \\
=& \sum_{j'j}\left\{\langle\psi_{j'}|\left[\sum_i\langle\Phi_i|\rho(t)\,|\Phi_i\rangle\right]|\psi_j\rangle\right\}\langle\psi_j|I(\psi)\,|\psi_{j'}\rangle \\
=& \sum_{j'j}\{\langle\psi_{j'}|\rho(\psi,t)\,|\psi_j\rangle\}\langle\psi_j|I(\psi)\,|\psi_{j'}\rangle
\end{aligned} \tag{1.20}$$

In the above representation, the reduced density matrix, $\rho(\psi,t)$ and its elements are defined by

$$\langle\psi_{j'}|\,\rho(\psi,t)\,|\psi_j\rangle = \sum_i \langle\Phi_i\psi_{j'}|\,\rho(t)\,|\Phi_i\psi_j\rangle \tag{1.21}$$

To illustrate this concept, let us consider a composite system comprising of two spin-1/2 nuclei. The composite system is represented by a matrix ($\rho(t)$) of dimension 4x4 (or in general, 2^N x 2^N). Based on the above description, the reduced density matrix for the individual spins is deduced and represented below.

$$\rho(I_1,t) = \begin{pmatrix} \rho_{\alpha\alpha,\alpha\alpha}(t)+\rho_{\alpha\beta,\alpha\beta}(t) & \rho_{\alpha\alpha,\beta\alpha}(t)+\rho_{\alpha\beta,\beta\beta}(t) \\ \\ \rho_{\beta\alpha,\alpha\alpha}(t)+\rho_{\beta\beta,\alpha\beta}(t) & \rho_{\beta\alpha,\beta\alpha}(t)+\rho_{\beta\beta,\beta\beta}(t) \end{pmatrix} \tag{1.22}$$

and

$$\rho(I_2,t) = \begin{pmatrix} \rho_{\alpha\alpha,\alpha\alpha}(t) + \rho_{\beta\alpha,\beta\alpha}(t) & \rho_{\alpha\alpha,\alpha\beta}(t) + \rho_{\beta\alpha,\beta\beta}(t) \\ \\ \rho_{\alpha\beta,\alpha\alpha}(t) + \rho_{\beta\beta,\beta\alpha}(t) & \rho_{\alpha\beta,\alpha\beta}(t) + \rho_{\beta\beta,\beta\beta}(t) \end{pmatrix} \tag{1.23}$$

In a similar vein, for a composite system comprising of three spin I=1/2 nuclei, the reduced density matrices for the individual spins are calculated as represented below.

$$\rho(I_1,t) = \begin{pmatrix} \rho_{\alpha\alpha\alpha,\alpha\alpha\alpha}(t) + \rho_{\alpha\alpha\beta,\alpha\alpha\beta}(t) & \rho_{\alpha\alpha\alpha,\beta\alpha\alpha}(t) + \rho_{\alpha\alpha\beta,\beta\alpha\beta}(t) \\ +\rho_{\alpha\beta\alpha,\alpha\beta\alpha}(t) + \rho_{\alpha\beta\beta,\alpha\beta\beta}(t) & +\rho_{\alpha\beta\alpha,\beta\beta\alpha}(t) + \rho_{\alpha\beta\beta,\beta\beta\beta}(t) \\ \\ \rho_{\beta\alpha\alpha,\alpha\alpha\alpha}(t) + \rho_{\beta\alpha\beta,\alpha\alpha\beta}(t) & \rho_{\beta\alpha\alpha,\beta\alpha\alpha}(t) + \rho_{\beta\alpha\beta,\beta\alpha\beta}(t) \\ +\rho_{\beta\beta\alpha,\alpha\beta\alpha}(t) + \rho_{\beta\beta\beta,\alpha\beta\beta}(t) & +\rho_{\beta\beta\alpha,\beta\beta\alpha}(t) + \rho_{\beta\beta\beta,\beta\beta\beta}(t) \end{pmatrix} \tag{1.24}$$

$$\rho(I_2,t) = \begin{pmatrix} \rho_{\alpha\alpha\alpha,\alpha\alpha\alpha}(t) + \rho_{\alpha\alpha\beta,\alpha\alpha\beta}(t) & \rho_{\alpha\alpha\alpha,\alpha\beta\alpha}(t) + \rho_{\alpha\alpha\beta,\alpha\beta\beta}(t) \\ +\rho_{\beta\alpha\alpha,\beta\alpha\alpha}(t) + \rho_{\beta\alpha\beta,\beta\alpha\beta}(t) & +\rho_{\beta\alpha\alpha,\beta\beta\alpha}(t) + \rho_{\beta\alpha\beta,\beta\beta\beta}(t) \\ \\ \rho_{\alpha\beta\alpha,\alpha\alpha\alpha}(t) + \rho_{\alpha\beta\beta,\alpha\alpha\beta}(t) & \rho_{\alpha\beta\alpha,\alpha\beta\alpha}(t) + \rho_{\alpha\beta\beta,\alpha\beta\beta}(t) \\ +\rho_{\beta\beta\alpha,\beta\alpha\alpha}(t) + \rho_{\beta\beta\beta,\beta\alpha\beta}(t) & +\rho_{\beta\beta\alpha,\beta\beta\alpha}(t) + \rho_{\beta\beta\beta,\beta\beta\beta}(t) \end{pmatrix} \tag{1.25}$$

and

$$\rho(I_3,t) = \begin{pmatrix} \rho_{\alpha\alpha\alpha,\alpha\alpha\alpha}(t) + \rho_{\alpha\beta\alpha,\alpha\beta\alpha}(t) & \rho_{\alpha\alpha\alpha,\alpha\alpha\beta}(t) + \rho_{\alpha\beta\alpha,\alpha\beta\beta}(t) \\ +\rho_{\beta\alpha\alpha,\beta\alpha\alpha}(t) + \rho_{\beta\beta\alpha,\beta\beta\alpha}(t) & +\rho_{\beta\alpha\alpha,\beta\alpha\beta}(t) + \rho_{\beta\beta\alpha,\beta\beta\beta}(t) \\ \\ \rho_{\alpha\alpha\beta,\alpha\alpha\alpha}(t) + \rho_{\alpha\beta\beta,\alpha\beta\alpha}(t) & \rho_{\alpha\alpha\beta,\alpha\alpha\beta}(t) + \rho_{\alpha\beta\beta,\alpha\beta\beta}(t) \\ +\rho_{\beta\alpha\beta,\beta\alpha\alpha}(t) + \rho_{\beta\beta\beta,\beta\beta\alpha}(t) & +\rho_{\beta\alpha\beta,\beta\alpha\beta}(t) + \rho_{\beta\beta\beta,\beta\beta\beta}(t) \end{pmatrix} \tag{1.26}$$

In the following section, the utility of the reduced density matrix approach in the theoretical description of NMR experiments is presented with few examples.

1.5.1 Detection of NMR signal

To begin with, let us consider a composite system comprising of two spin, I=1/2 nuclei. The Hamiltonian for such a system is represented by,

$$H = \omega_1 I_{1z} + \omega_2 I_{2z} + J_{12} I_{1z} I_{2z} \tag{1.27}$$

For the sake of illustration, the flip-flop operators are ignored in the scalar interactions. In the conventional description of the spin dynamics, the NMR signal is

calculated using the identity operator of the composite system.

$$\begin{aligned}\left\langle I_1^+(t)\right\rangle =&\mathrm{Tr}\left\{\rho(t)I_1^+\right\}\\ =&\mathrm{Tr}\left\{e^{-\frac{i}{\hbar}Ht}\rho(0)e^{\frac{i}{\hbar}Ht}.I_1^+\right\}\\ =&\sum_{i,j=1}^{4}\langle\phi_i|e^{-\frac{i}{\hbar}Ht}\rho(0)e^{\frac{i}{\hbar}Ht}\left|\phi_j\right\rangle\langle\phi_j|I_1^+\left|\phi_i\right\rangle\end{aligned} \tag{1.28}$$

where $\rho(0) = aI_{1x} + bI_{2x}$, is the initial condition of the system at time t=0. Since, the Hamiltonian is diagonal in the basis chosen, the solution to the above equation is straight forward.

$$\left\langle I_1^+(t)\right\rangle = ae^{\mathrm{i}\omega_1\mathrm{t}}\cos\left(\frac{J_{12}}{2}\right)t \tag{1.29}$$

In a similar vein, the signal corresponding to spin-2 is evaluated .

$$\begin{aligned}\left\langle I_2^+(t)\right\rangle =&\mathrm{Tr}\left\{\rho(t)I_2^+\right\}\\ =&be^{\mathrm{i}\omega_2\mathrm{t}}\cos\left(\frac{J_{12}}{2}\right)t\end{aligned} \tag{1.30}$$

Alternatively, in the reduced density matrix approach, the NMR signal for the composite system is calculated by evaluating the density operator of individual spins. Based on our earlier description, the reduced density matrices for the individual spins are calculated and represented below.

$$\rho(I_1,t) = \begin{pmatrix} 0 & ae^{-\mathrm{i}\omega_1\mathrm{t}}\cos\left(\frac{J_{12}}{2}\right)t \\ ae^{\mathrm{i}\omega_1\mathrm{t}}\cos\left(\frac{J_{12}}{2}\right)t & 0 \end{pmatrix} \tag{1.31}$$

and

$$\rho(I_2,t) = \begin{pmatrix} 0 & be^{-\mathrm{i}\omega_2\mathrm{t}}\cos\left(\frac{J_{12}}{2}\right)t \\ be^{\mathrm{i}\omega_2\mathrm{t}}\cos\left(\frac{J_{12}}{2}\right)t & 0 \end{pmatrix} \tag{1.32}$$

The signal corresponding to individual spins is evaluated separately through the Trace operation described below.

$$\begin{aligned}\left\langle I_1^+(t)\right\rangle =&\mathrm{Tr}\left\{\rho(I_1,t)I_1^+\right\}\\ =&ae^{\mathrm{i}\omega_1\mathrm{t}}\cos\left(\frac{J_{12}}{2}\right)t\end{aligned} \tag{1.33}$$

$$\begin{aligned}\left\langle I_2^+(t)\right\rangle =&\mathrm{Tr}\left\{\rho(I_2,t)I_2^+\right\}\\ =&be^{\mathrm{i}\omega_2\mathrm{t}}\cos\left(\frac{J_{12}}{2}\right)t\end{aligned} \tag{1.34}$$

1.5.2 Polarization transfer experiments in NMR

To extract molecular information (or parameters), polarization transfer experiments are routinely employed in NMR spectroscopy. The molecular parameters in such experiments are extracted by quantifying the polarization transfer /exchange among spins. For demonstrative purposes, let us consider a coupled two-spin (spin-1/2) system governed by the following zero quantum (ZQ) Hamiltonian.

$$H = \omega_1 I_{1z} + \omega_2 I_{2z} + J_{12}\left\{I_{1z}I_{2z} + \tfrac{1}{2}(I_1^+ I_2^- + I_1^- I_2^+)\right\} \tag{1.35}$$

For the sake of clarity, the above Hamiltonian is represented in a compact form as described below.

$$H = \omega_1 I_{1z} + \omega_2 I_{2z} + D_{12}^{zz} I_{1z} I_{2z} + D_{12}^{PM} I_1^+ I_2^- + D_{12}^{MP} I_1^- I_2^+ \tag{1.36}$$

where $D_{12}^{zz} = J_{12}$, $D_{12}^{PM} = \frac{J_{12}}{2}$ ('PM' for plus-minus) and $D_{12}^{MP} = \frac{J_{12}}{2}$ ('MP' for minus-plus).

Our objective in this section is to calculate the polarization transfer between the two spins. To begin with, let $\rho(0) = aI_{1z} + bI_{2z}$ represent the initial state of the composite system. In case of longitudinal polarization transfer experiments, the z-component of the magnetization is measured using the composite density matrix, $\rho(t)$.

$$\langle I_{1z}(t)\rangle = \mathrm{Tr}\left\{\rho(t) I_{1z}\right\} \tag{1.37}$$

In the above equation, $\rho(t)$ denotes the composite density matrix after time 't'. To obtain a closed form of solution, the standard BCH (Baker-Campbell-Hausdorff)[8,59] formula is employed.

$$\begin{bmatrix} \frac{(a+b)}{2} & 0 & 0 & 0 \\ 0 & (a-b)\left\{\frac{1}{2} - D_{12}^{PM} D_{12}^{MP} \frac{\sin^2 xt}{x^2}\right\} & \rho(t)_{23} & 0 \\ 0 & \rho(t)_{32} & -(a-b)\left\{\frac{1}{2} - D_{12}^{PM} D_{12}^{MP} \frac{\sin^2 xt}{x^2}\right\} & 0 \\ 0 & 0 & 0 & -\frac{(a+b)}{2} \end{bmatrix} \tag{1.38}$$

where

$$\rho(t)_{23} = -(a-b) D_{12}^{PM}\left\{\left(\tfrac{\omega_1-\omega_2}{2}\right)\tfrac{\sin^2 xt}{x^2} + i\tfrac{\sin 2xt}{2x}\right\}$$

$$\rho(t)_{32} = -(a-b) D_{12}^{MP}\left\{\left(\tfrac{\omega_1-\omega_2}{2}\right)\tfrac{\sin^2 xt}{x^2} - i\tfrac{\sin 2xt}{2x}\right\}$$

Using this result, the expectation value (i.e, the z-component of polarization) for the individual spins is calculated.

$$\begin{aligned}\langle I_{1z}(t)\rangle =& \mathrm{Tr}\left\{(\rho(t))_{4X4}(I_{1z})_{4X4}\right\}\\ =& a-(a-b)D_{12}^{PM}D_{12}^{MP}\frac{\sin^2 xt}{x^2}\end{aligned} \tag{1.39}$$

where $x=\sqrt{\left(\frac{\omega_1-\omega_2}{2}\right)^2+D_{12}^{PM}D_{12}^{MP}}$

$$\begin{aligned}\langle I_{2z}(t)\rangle =& \mathrm{Tr}\left\{[\rho(t)]_{4X4}[I_{2z}]_{4X4}\right\}\\ =& b+(a-b)D_{12}^{PM}D_{12}^{MP}\frac{\sin^2 xt}{x^2}\end{aligned} \tag{1.40}$$

From the above expression, it is clear that the flip-flop operators in the scalar Hamiltonian are primarily responsible for the propagation of polarization among spins in NMR spectroscopy. With increase in the number of spins, the above approach becomes intractable for analytic calculations. Hence, we revert to the reduced density matrix approach.

Based on our earlier description, the reduced density matrices for the individual spins are derived from the complete density matrix through the partial trace operation. For example, the first element of the reduced density matrix (refer to Eq. 1.22) is evaluated by calculating a set of matrix elements of the combined density matrix. Employing BCH expansion, the elements of the reduced density matrix are constructed from the combined density matrix as described below.

$$\rho(I_1,t)=\begin{pmatrix}\rho_{\alpha\alpha,\alpha\alpha}(t)+\rho_{\alpha\beta,\alpha\beta}(t) & \rho_{\alpha\alpha,\beta\alpha}(t)+\rho_{\alpha\beta,\beta\beta}(t)\\ \\ \rho_{\beta\alpha,\alpha\alpha}(t)+\rho_{\beta\beta,\alpha\beta}(t) & \rho_{\beta\alpha,\beta\alpha}(t)+\rho_{\beta\beta,\beta\beta}(t)\end{pmatrix} \tag{1.41}$$

For the demonstrative purpose, let us evaluate the first element, $\rho_{\alpha\alpha,\alpha\alpha}(t)+\rho_{\alpha\beta,\alpha\beta}(t)$.

$$\rho_{\alpha\alpha,\alpha\alpha}(t)=\langle\alpha\alpha|\, e^{-\frac{i}{\hbar}Ht}\rho(0)e^{\frac{i}{\hbar}Ht}\,|\alpha\alpha\rangle \tag{1.42}$$

$$\langle\alpha\alpha|\, e^{-\frac{i}{\hbar}Ht}=\left[\cos\left(\tfrac{(\omega_1+\omega_2)}{2}\right)t-i\sin\left(\tfrac{(\omega_1+\omega_2)}{2}\right)t\right]\langle\alpha\alpha| \tag{1.43}$$

$$\rho(0)=aI_{1z}+bI_{2z} \tag{1.44}$$

$$e^{\frac{i}{\hbar}Ht}\left|\alpha\alpha\right\rangle = \left[\cos\left(\tfrac{(\omega_1+\omega_2)}{2}\right)t + i\sin\left(\tfrac{(\omega_1+\omega_2)}{2}\right)t\right]\left|\alpha\alpha\right\rangle \tag{1.45}$$

Now, $\rho_{\alpha\alpha,\alpha\alpha}(t) = \frac{(a+b)}{2}$

In a similar vein,

$$\rho_{\alpha\beta,\alpha\beta}(t) = \left\langle\alpha\beta\right| e^{-\frac{i}{\hbar}Ht}\rho(0)e^{\frac{i}{\hbar}Ht}\left|\alpha\beta\right\rangle \tag{1.46}$$

$$\left\langle\alpha\beta\right| e^{-\frac{i}{\hbar}Ht} = \left[\cos xt - i\frac{(\omega_1-\omega_2)}{2x}\sin xt\right]\left\langle\alpha\beta\right| - \left[i\frac{D_{12}^{PM}}{x}\sin xt\right]\left\langle\beta\alpha\right| \tag{1.47}$$

$$\rho(0) = aI_{1z} + bI_{2z} \tag{1.48}$$

$$e^{\frac{i}{\hbar}Ht}\left|\alpha\beta\right\rangle = \left[\cos xt + i\frac{(\omega_1-\omega_2)}{2x}\sin xt\right]\left|\alpha\beta\right\rangle + \left[i\frac{D_{12}^{MP}}{x}\sin xt\right]\left|\beta\alpha\right\rangle \tag{1.49}$$

Now,

$$\begin{aligned}\rho_{\alpha\beta,\alpha\beta}(t) =& (a-b)\frac{1}{2}\left[\cos^2 xt + \frac{\left((\omega_1-\omega_2)/2\right)^2 + D_{12}^{PM}D_{12}^{MP}}{\left((\omega_1-\omega_2)/2\right)^2 + D_{12}^{PM}D_{12}^{MP}}\sin^2 xt - 2D_{12}^{PM}D_{12}^{MP}\frac{\sin^2 xt}{x^2}\right]\\ =& (a-b)\left[\frac{1}{2} - D_{12}^{PM}D_{12}^{MP}\frac{\sin^2 xt}{x^2}\right]\end{aligned} \tag{1.50}$$

where $x = \sqrt{\left(\frac{\omega_1-\omega_2}{2}\right)^2 + D_{12}^{PM}D_{12}^{MP}}$

Combining these two elements, the first element of the reduced density matrix corresponding to spin-1 is derived.

$$\rho_{\alpha\alpha,\alpha\alpha}(t) + \rho_{\alpha\beta,\alpha\beta}(t) = \frac{(a+b)}{2} + (a-b)\left[\frac{1}{2} - D_{12}^{PM}D_{12}^{MP}\frac{\sin^2 xt}{x^2}\right] \tag{1.51}$$

Following the above procedure, the reduced density matrix for the individual spins are calculated and the longitudinal single-spin polarizations are evaluated independently through their individual reduced density matrices.

$$\langle I_{1z}(t)\rangle = \mathrm{Tr}\left\{(\rho(I_1,t))_{2X2}(I_{1z})_{2X2}\right\}$$

$$= \mathrm{Tr}\left\{\begin{pmatrix} \frac{(a+b)}{2} + \\ (a-b)\left\{\frac{1}{2} - D_{12}^{PM}D_{12}^{MP}\frac{\sin^2 xt}{x^2}\right\} & 0 \\ 0 & -(a-b)\left\{\frac{1}{2} - D_{12}^{PM}D_{12}^{MP}\frac{\sin^2 xt}{x^2}\right\} - \\ & \frac{(a+b)}{2} \end{pmatrix}\begin{pmatrix} \frac{1}{2} & 0 \\ 0 & -\frac{1}{2} \end{pmatrix}\right\}$$

$$= a - (a-b)D_{12}^{PM}D_{12}^{MP}\frac{\sin^2 xt}{x^2} \tag{1.52}$$

where $x = \sqrt{\left(\frac{\omega_1-\omega_2}{2}\right)^2 + D_{12}^{PM} D_{12}^{MP}}$

Similarly the signal corresponding to spin-2 is calculated by,

$$\langle I_{2z}(t)\rangle = \mathrm{Tr}\left\{\left(\rho(I_2,t)\right)\left(I_{2z}\right)\right\}$$

$$= \mathrm{Tr}\left\{ \begin{pmatrix} \frac{(a+b)}{2} - (a-b)\left\{\frac{1}{2} - D_{12}^{PM} D_{12}^{MP} \frac{\sin^2 xt}{x^2}\right\} & 0 \\ 0 & (a-b)\left\{\frac{1}{2} - D_{12}^{PM} D_{12}^{MP} \frac{\sin^2 xt}{x^2}\right\} - \frac{(a+b)}{2} \end{pmatrix} \begin{pmatrix} \frac{1}{2} & 0 \\ 0 & -\frac{1}{2} \end{pmatrix} \right\}$$

$$= b + (a-b) D_{12}^{PM} D_{12}^{MP} \frac{\sin^2 xt}{x^2} \tag{1.53}$$

The analytic expressions for the expectation values of the individual spins calculated from the reduced density matrix approach are in accord with those employing full density matrix methods.

In contrast to the description involving the composite density matrix $(\rho(t))$, the reduced density matrix $(\rho(I,t))$ approach is comparatively less intense and its utility in the description of polarization transfer in SSNMR experiments will be discussed extensively in this thesis (refer Appendix-I(a) for expressions under DQ conditions).

1.6 Organization of the thesis

In this thesis, an analytic model integrating the concepts of effective Hamiltonians and Reduced density matrix is proposed to describe the multi-spin effects arising in SSNMR experiments. The approach presented is suitable to treat both homonuclear and heteronuclear dipolar recouping experiments and could be employed to quantify the experimental results emerging from such experiments.

For demonstrative purposes, the phenomenon of R^2 is re-examined using the reduced density matrix formalism. To date, the R^2 experiment remains the method of choice for measuring $^{13}C - {}^{13}C$ distances in uniformly labeled solids. In the R^2 experiment, the dipolar interactions between spin pairs are reintroduced in a con-

trolled fashion and have routinely been employed to measure interatomic distances in systems of varying complexities. Since the number of structural constraints available in the solid-state are restricted due to limited availability of resolution, the estimation of constraints /interpretation of experimental data become important. With this objective in mind, a thorough analysis of the magnetization exchange between spins in R^2 experiments is described in this thesis. In contrast to other existing descriptions in the literature,[45,47,49,51–55] the analytic model presented in this thesis is computationally less intense and provides a better framework for elucidating the role of residual $^{13}C-{}^{1}H$ dipolar interactions on the exchange dynamics. Through rigorous comparison with simulations emerging from exact numerical methods, the validity of the analytic results is verified.

In the second chapter, the theory of R^2 experiments is explained with in the framework of the reduced density matrix. Integrating the concepts of reduced density matrix and effective Hamiltonians, polarization transfer between a spin-pair is described analytically through expressions that resemble to those derived by Rabi.[79] Additionally, polarization transfer in band selective experiments is described using a model system comprising of three carbons.

In the third chapter, the role of $^{13}C-{}^{1}H$ dipolar interactions in R^2 experiments is discussed. In the past, the effect of protons were incorporated through phenomenological damping constants. As an alternative, employing model systems $I_1-I_2-S_N$ and $I_1-I_2-I_3-S_N$, the polarization transfer in R^2 experiments is described analytically through the reduced density matrix approach without increasing the complexity.

In the fourth chapter, the phenomenon of higher order and fractional Rotational resonance conditions are discussed. Employing multi-mode Floquet theory, the phenomenon of fractional R^2 conditions in multiple-pulse based R^2 experiments is discussed and illustrated with few examples. The results obtained in the thesis are summarized in the final chapter along with possible extensions of the present work.

1.7 Appendix-I

a. Polarization transfer in Double-quantum experiments

To describe the mechanism of polarization transfer experiments involving effective Hamiltonians involving double-quantum operators (e.g. double-quantum version of SPECIFIC CP[80,81] experiment, RRTR experiments[43,44,49] etc.), let us consider a coupled two-spin (spin-1/2) system governed by the following equation.

$$H = \omega_1 I_{1z} + \omega_2 I_{2z} + D_{12}^{zz} I_{1z} I_{2z} + D_{12}^{PP} I_1^+ I_2^+ + D_{12}^{MM} I_1^- I_2^- \tag{1.54}$$

To start with, let $\rho(0) = aI_{1z} + bI_{2z}$ be the initial state of the composite system at time, t=0. In the reduced density matrix approach, the longitudinal single-spin polarizations (corresponding to I_2 operators) are evaluated independently through their individual reduced density matrices under the DQ Hamiltonian (Eq. 1.54).

$$\langle I_{1z}(t)\rangle = \mathrm{Tr}\left\{\rho(I_1,t).I_{1z}\right\}$$

$$= \mathrm{Tr}\left\{ \begin{pmatrix} \frac{(a+b)}{2}\left\{\frac{1}{2} - D_{12}^{PP} D_{12}^{MM} \frac{\sin^2 xt}{x^2}\right\} + \frac{(a-b)}{2} & 0 \\ 0 & -\frac{(a-b)}{2} - \frac{(a+b)}{2}\left\{\frac{1}{2} - D_{12}^{PP} D_{12}^{MM} \frac{\sin^2 xt}{x^2}\right\} \end{pmatrix} \begin{pmatrix} \frac{1}{2} & 0 \\ 0 & -\frac{1}{2} \end{pmatrix} \right\}$$

$$= a - (a+b) D_{12}^{PP} D_{12}^{MM} \frac{\sin^2 xt}{x^2} \tag{1.55}$$

In a similar vein, the polarization build up on spin-2 is evaluated as given below.

$$\langle I_{2z}(t)\rangle = \mathrm{Tr}\left\{\rho(I_2,t).I_{2z}\right\}$$

$$= \mathrm{Tr}\left\{\begin{pmatrix} \frac{(a+b)}{2}\left\{\frac{1}{2}-D_{12}^{PP}D_{12}^{MM}\frac{\sin^2 xt}{x^2}\right\}- & 0 \\ 0 & \frac{(a-b)}{2}- \\ & \frac{(a+b)}{2}\left\{\frac{1}{2}-D_{12}^{PP}D_{12}^{MM}\frac{\sin^2 xt}{x^2}\right\} \end{pmatrix}\begin{pmatrix} \frac{1}{2} & 0 \\ 0 & -\frac{1}{2} \end{pmatrix}\right\}$$

$$= b-(a+b)D_{12}^{PP}D_{12}^{MM}\frac{\sin^2 xt}{x^2} \tag{1.56}$$

where $x = \sqrt{\left(\frac{\omega_1+\omega_2}{2}\right)^2 + D_{12}^{PP}D_{12}^{MM}}$. When $\rho(0) = aI_{1z}$, the above equations reduce to a much simpler form.

$$\langle I_{1z}(t)\rangle = a - aD_{12}^{PP}D_{12}^{MM}\frac{\sin^2 xt}{x^2} \tag{1.57}$$

$$\langle I_{2z}(t)\rangle = -aD_{12}^{PP}D_{12}^{MM}\frac{\sin^2 xt}{x^2} \tag{1.58}$$

In contrast to the polarization transfer in ZQ process (Eq. 1.53), the polarization transfer in DQ experiments has a negative sign (Eq. 1.58). Here, the reduced density matrix approach provides better analytic insights into the mechanism of polarization transfer in NMR experiments.

References

[1] I. I. Rabi, *Phys. Rev.*, 1936, **49**, 324–328.

[2] F. Bloch, *Phys. Rev.*, 1946, **70**, 460–474.

[3] E. M. Purcell, H. C. Torrey and R. V. Pound, *Phys. Rev.*, 1946, **69**, 37–38.

[4] E. R. Andrew, A. Bradbury and R. G. Eades, *Nature*, 1958, **182**, 1659–1659.

[5] I. J. Lowe, *Phys. Rev. Lett.*, 1959, **2**, 285–287.

[6] M. Maricq and J. S. Waugh, *J. Chem. Phys.*, 1979, **70**, 3300–3316.

[7] U. Haeberlein, *High resolution NMR in solids: selected averaging*, Acad. Press, 1976.

[8] M. Mehring, *Principles of High Resolution NMR in solids*, (Springer, Berlin, 1983), 2nd edn.

[9] S. R. Hartmann and E. L. Hahn, *Phys. Rev.*, 1962, **128**, 2042–2053.

[10] A. Pines, M. G. Gibby and J. S. Waugh, *J. Chem. Phys.*, 1973, **59**, 569–590.

[11] P. Tekely, P. Palmas and D. Canet, *J. Magn. Reson. A*, 1994, **107**, 129 – 133.

[12] A. E. Bennett, C. M. Rienstra, M. Auger, K. V. Lakshmi and R. G. Griffin, *J. Chem. Phys.*, 1995, **103**, 6951–6958.

[13] Z. Gan and R. Ernst, *Solid State Nucl. Magn. Reson.*, 1997, **8**, 153 – 159.

[14] Y. Yu and B. Fung, *J. Magn. Reson.*, 1998, **130**, 317 – 320.

[15] M. Edén and M. H. Levitt, *J. Chem. Phys.*, 1999, **111**, 1511–1519.

[16] M. Carravetta, M. Edén, X. Zhao, A. Brinkmann and M. H. Levitt, *Chem. Phys. Lett.*, 2000, **321**, 205 – 215.

[17] B. Fung, A. Khitrin and K. Ermolaev, *J. Magn. Reson.*, 2000, **142**, 97 – 101.

[18] K. Takegoshi, J. Mizokami and T. Terao, *Chem. Phys. Lett.*, 2001, **341**, 540 – 544.

[19] A. Detken, E. H. Hardy, M. Ernst and B. H. Meier, *Chem. Phys. Lett.*, 2002, **356**, 298 – 304.

[20] A. Khitrin, T. Fujiwara and H. Akutsu, *J. Magn. Reson.*, 2003, **162**, 46 – 53.

[21] G. De Paëpe, A. Lesage and L. Emsley, *J. Chem. Phys.*, 2003, **119**, 4833–4841.

[22] G. D. Paëpe, D. Sakellariou, P. Hodgkinson, S. Hediger and L. Emsley, *Chem. Phys. Lett.*, 2003, **368**, 511 – 522.

[23] G. De Paëpe, B. Eléna and L. Emsley, *J. Chem. Phys.*, 2004, **121**, 3165–3180.

[24] R. Ramachandran, V. S. Bajaj and R. G. Griffin, *J. Chem. Phys.*, 2005, **122**, 164503.

[25] R. S. Thakur, N. D. Kurur and P. Madhu, *Chem. Phys. Lett.*, 2006, **426**, 459 – 463.

[26] I. Scholz, P. Hodgkinson, B. H. Meier and M. Ernst, *J. Chem. Phys.*, 2009, **130**, 114510.

[27] J. M. Vinther, A. B. Nielsen, M. Bjerring, E. R. H. van Eck, A. P. M. Kentgens, N. Khaneja and N. C. Nielsen, *J. Chem. Phys.*, 2012, **137**, 214202.

[28] A. W. Overhauser, *Phys. Rev.*, 1953, **92**, 411–415.

[29] E. Bennett, R. G. Griffin and S. Vega, *Solid State NMR IV: Methods and Applications of Solid-State NMR, edited by B. Blumich (Springer-Verlag, Berlin, 1994), Vol. 33, pp. 1*.

[30] R. G. Griffin, *Nat. Struct. Biol.*, 1998, **5**, 508–512.

[31] S. Dusold and A. Sebald, Academic Press, 2000, vol. 41, pp. 185 – 264.

[32] M. H. Levitt, *Encyclopedia of Nuclear Magnetic Resonance, edited by D. M. Grant, and R. K. Harris (John Wiley & Sons, 2002), Vol. 9, pp. 165*.

[33] M. H. Levitt, *J. Chem. Phys.*, 2008, **128**, 052205.

[34] V. Ladizhansky, *Solid State Nucl. Magn. Reson.*, 2009, **36**, 119 – 128.

[35] G. D. Paëpe, *Annu. Rev. Phys. Chem.*, 2012, **63**, 661–684.

[36] E. Andrew, A. Bradbury, R. Eades and V. Wynn, *Phys. Lett.*, 1963, **4**, 99 – 100.

[37] E. Andrew, S. Clough, L. Farnell, T. Gledhill and I. Roberts, *Phys. Lett.*, 1966, **21**, 505 – 506.

[38] D. Raleigh, G. Harbison, T. Neiss, J. Roberts and R. Griffin, *Chem. Phys. Lett.*, 1987, **138**, 285 – 290.

[39] D. Raleigh, M. Levitt and R. Griffin, *Chem. Phys. Lett.*, 1988, **146**, 71 – 76.

[40] D. P. Raleigh, F. Creuzet, S. K. D. Gupta, M. H. Levitt and R. G. Griffin, *J. Am. Chem. Soc.*, 1989, **111**, 4502–4503.

[41] B. H. Meier and W. L. Earl, *J. Am. Chem. Soc.*, 1987, **109**, 7937–7942.

[42] M. Colombo, B. Meier and R. Ernst, *Chem. Phys. Lett.*, 1988, **146**, 189 – 196.

[43] K. Takegoshi, K. Nomura and T. Terao, *Chem. Phys. Lett.*, 1995, **232**, 424 – 428.

[44] K. Takegoshi, K. Nomura and T. Terao, *J. Magn. Reson.*, 1997, **127**, 206 – 216.

[45] M. H. Levitt, D. P. Raleigh, F. Creuzet and R. G. Griffin, *J. Chem. Phys.*, 1990, **92**, 6347–6364.

[46] R. Ramachandran, V. Ladizhansky, V. S. Bajaj, and R. G. Griffin, *J. Am. Chem. Soc.*, 2003, **125**, 15623–15629.

[47] R. Ramachandran, J. R. Lewandowski, P. C. A. van der Wel and R. G. Griffin, *J. Chem. Phys.*, 2006, **124**, 214107.

[48] P. R. Costa, B. Sun and R. G. Griffin, *J. Magn. Reson.*, 2003, **164**, 92 – 103.

[49] V. Ladizhansky, and R. G. Griffin, *J. Am. Chem. Soc.*, 2004, **126**, 948–958.

[50] P. C. A. van der Wel, M. T. Eddy, R. Ramachandran and R. G. Griffin, *ChemPhysChem*, 2009, **10**, 1656–1663.

[51] R. Janik, X. Peng and V. Ladizhansky, *J. Magn. Reson.*, 2007, **188**, 129 – 140.

[52] R. J. G. H. Xiaohu Peng, David Libich and V. Ladizhansky, *J. Am. Chem. Soc.*, 2008, **130**, 359–369.

[53] P. T. F. Williamson, A. Verhoeven, M. Ernst, and B. H. Meier, *J. Am. Chem. Soc.*, 2003, **125**, 2718–2722.

[54] L. Sonnenberg, S. Luca and M. Baldus, *J. Magn. Reson.*, 2004, **166**, 100 – 110.

[55] M. K. Pandey and R. Ramachandran, *Mol. Phys.*, 2010, **108**, 619–635.

[56] M. K. Pandey and R. Ramachandran, *Mol. Phys.*, 2011, **109**, 1545–1565.

[57] M. K. Pandey, Z. Qadri and R. Ramachandran, *J. Chem. Phys.*, 2013, **138**, 114108.

[58] C. Banwell and H. Primas, *Mol. Phys.*, 1963, **6**, 225–256.

[59] K. Blum, *Density Matrix Theory and Applications*, Plenum press, New York, 1996.

[60] U. SivaRanjan and R. Ramachandran, *J. Chem. Phys.*, 2014, **140**, 054101.

[61] R. Ramesh and M. S. Krishnan, *J. Chem. Phys.*, 2001, **114**, 5967.

[62] E. Vinogradov, P. K. Madhu and S. Vega, *J. Chem. Phys.*, 2001, **115**, 8983.

[63] J. H. Van Vleck, *Phys. Rev.*, 1929, **33**, 467–506.

[64] D. Papousek and M. R. Aliev, *Molecular Vibrational-Rotational spectra*, Elsevier, Amsterdam, 1982.

[65] M. Veshtort and R. G. Griffin, *J. Magn. Reson.*, 2006, **178**, 248 – 282.

[66] M. Bak, J. T. Rasmussen and N. C. Nielsen, *J. Magn. Reson.*, 2000, **147**, 296 – 330.

[67] G. Floquet, *Ann. Sci. Ecole Norm. Sup*, 1883, **12**, 47–89.

[68] J. H. Shirley, *Phys. Rev.*, 1965, **138**, 979–987.

[69] D. Zax, G. Goelman, D. Abramovich and S. Vega, in *Advances in Magnetic Resonance*, ed. W. S. Warren, Academic Press, 1990, vol. 14, pp. 219 – 240.

[70] S. Vega, *in Nuclear Magnetic Probes for Molecular Dynamics, edited by R. Tycko*, (Kluwer Academic, Amsterdam, 1994).

[71] S. Vega, *in Encyclopedia of NMR, edited by D. M. Grant and R. Harris*, (Wiley, New York, 1996).

[72] B. C. Filip, X. Filip, D. E. Demco and S. Hafner, *Mol. Phys.*, 1997, **92**, 757–772.

[73] R. Ramachandran and R. G. Griffin, *J. Chem. Phys.*, 2005, **122**, 164502.

[74] M. Leskes, P. Madhu and S. Vega, *Prog. Nucl. Magn. Reson. Spectrosc.*, 2010, **57**, 345 – 380.

[75] I. Scholz, J. D. van Beek and M. Ernst, *Solid State Nuclear Magnetic Resonance*, 2010, **37**, 39 – 59.

[76] A. R. Edmonds, *Angular Momentum in Quantum Mechanics, 3rd ed*, Princeton University Press, New Jeresy.

[77] M. M. Maricq, *Phys. Rev. B*, 1982, **25**, 6622–6632.

[78] M. M. Maricq, in *Advances in Magnetic Resonance*, ed. W. S. Warren, Academic Press, 1990, vol. 14, pp. 151 – 182.

[79] I. I. Rabi, *Phys. Rev.*, 1937, **51**, 652–654.

[80] M. Baldus, A. T. Petkova, J. Herzfeld and R. G. Griffin, *Mol. Phys.*, 1998, **95**, 1197–1207.

[81] M. Bjerring and N. C. Nielsen, *Chem. Phys. Lett.*, 2003, **382**, 671 – 678.

Chapter 2

Description of R^2 phenomenon using Rabi oscillations and Reduced density matrix theory

2.1 Rotational Resonance

2.1.1 Background

In 1963, Andrew and coworkers[1,2] reported an interesting phenomenon depicting the dependance of ^{31}P nuclear relaxation times on sample spinning frequency in magic angle spinning (MAS)[3,4] experiments. Under normal experimental conditions, in a magnetic field of strength 0.5 T, the spin-lattice relaxation times (T_1) of the ^{31}P nuclei in solid phosphorous pentachloride (comprising of tetrachloride and hexachloride ions) were estimated to be 6 ms and 0.6 ms, respectively. Interestingly, when the sample spinning frequency coincided with the chemical shift separation between the two ^{31}P nuclei, the measured T_1 relaxation times were identical (0.6 ms) for both the ^{31}P nuclei. However, for all other spinning frequencies, the two phosphorous nuclei in phosphorous pentachloride tend to relax independently with different relaxation times. This intriguing observation was explained in terms of the exchange of spin energy between the two ^{31}P nuclei through the flip-flop operators present in the dipolar Hamiltonian and was subsequently termed as Rotational relaxation resonance or nuclear cross-relaxation through sample rotation. Since the energy imbalance cre-

ated by the flip-flop processes was compensated through the mechanical rotation of the sample, it was proposed that this new form of rotation induced cross-relaxation should be possible in both homonuclear and heteronuclear spin systems. In addition to the T_1 relaxation time measurements, Andrew and coworkers also reported broadening of the peaks under these special conditions. Due to intermolecular spin interactions (^{31}P, 100% natural abundance), their experimental results could never be utilized for extracting any molecular parameter of interest.

After a hiatus of almost two decades, Griffin and co-workers[5–7] introduced a novel approach of employing ^{13}C- enriched spin pair samples (e.g. doubly labeled ZnAc) for replicating the line broadening effects observed by Andrew and coworkers[1,2] in MAS experiments. To mimic an isolated spin pair and minimize the intermolecular effects, the doubly labeled sample was diluted in natural abundance. In accord with earlier observations,[2] strong distortions to the line shapes along with splitting of the individual resonances were observed in the vicinity of the rotational resonance (R^2) matching conditions (i.e., $|\upsilon_1 - \upsilon_2| = N\upsilon_R$). In contrast to the experimental results reported by Andrew and coworkers, the strategy of employing magnetically dilute samples provided the luxury of quantifying the experimental observations under R^2 conditions. With this objective, Griffin and coworkers[5–7] proposed an experiment (commonly referred to as longitudinal magnetization exchange), wherein the difference magnetization between the two spins in the sample was monitored as a function of the mixing time. For the very first time in the literature, the resulting dipolar trajectories were successfully simulated using molecular parameters such as the chemical shielding tensors (magnitude and orientations) and dipolar coupling constants within an isolated two-spin framework.

In a remarkable coincidence, Ernst and coworkers[8] reported a novel method for enhancing the spin diffusion among carbons in solid state MAS NMR experiments. In a typical solid sample, spin diffusion takes place through the flip-flop operators present in the dipolar Hamiltonian and could serve as an important experimental tool for obtaining the structural information at the atomic level. Owing to the favorable chemical shift dispersion, diffusion measurements among ^{13}C nuclei were preferred in spite of its lower natural abundance and low diffusion rate constants (0.01 s^{-1}) available in the solid-state. In the conventional spin diffusion experiments (PDSD),[9,10] the energy imbalance resulting from the flip-flop processes involving carbons is pro-

vided through the interaction with the surrounding proton bath. Interestingly, when the sample spinning frequency (multiple of it) was adjusted to the chemical shift difference between specific sites, their spin diffusion rates get enhanced. Subsequently, this mode of spin diffusion was termed by Ernst and coworkers as 'rotor-driven' spin diffusion (RDSD)[8] in solid-state NMR. In contrast to the PDSD experiments, the diffusion in RDSD experiments takes place at faster time-scales and are chemical shift selective. Since the energy mismatch (resulting from the flip-flop processes) in RDSD experiments are compensated by the mechanical rotation of the sample, coupling to the proton bath is detrimental. Consequently, it was realized that MAS experiments implemented at R^2 conditions could present an attractive solution for chemical shift selective polarization transfer among nuclei and could serve as a tool for extracting interatomic homonuclear distances in solid-state NMR.

To this end, the initial attempt to describe the spin dynamics under R^2 conditions in MAS experiments was provided by Gan et al[11]. In the model proposed by Gan et al, the polarization transfer between two spins under R^2 conditions was explained through a psuedo-spin model comprising of virtual spin states. Following this approach, Levitt et al[12] presented a model for describing the spin dynamics in the Liouville space. To minimize the complexity in the Liouville space, Levitt et al proposed an approach, wherein the spin dynamics in the Liouville space is described in a reduced subspace (commonly referred to as "zero-quantum" subspace) through a simple vector model (comprising of the set of operators I_{23}^z, I_{23}^y and I_{23}^x) defined on the basis of the fictitious spin operator framework.[12] The z-component of this vector comprises of the difference longitudinal magnetization, while the transverse components comprise of the flip-flop operators. At the exact resonance condition, the longitudinal magnetization is flipped to the transverse plane and the dynamics is very similar to the standard description of single-pulse experiment using Bloch-type equations. In the transverse plane, the magnetization decays with a rate constant[12] ($r = T_{ZQ}^{-1}$) and was presumed to be similar to the T_2 spin-spin relaxation encountered in standard NMR experiments. Although, such an approach minimizes the computational time and is quite handful in the description of isolated spin pair systems, the framework presented is less suitable for quantitative purposes. Additionally, the proposed model only presents a framework for the inclusion of a phenomenological damping rate constant without any physical basis.

As an alternative to the existing descriptions based on Average Hamiltonian theory (AHT),[13–15] Vega and coworkers[16] provided a theoretical framework based on Floquet theory.[17–25] In their approach, the spin dynamics under R^2 conditions was explained through the concept of level-crossings between the dressed Floquet states. Although, the approach presented is refreshingly new, the description is semi-analytical and does not present a comprehensive framework for describing the underlying spin dynamics in R^2 experiments. In an alternate approach, Ramachandran and coworkers[26,27] proposed a model for describing the spin dynamics in R^2 experiments in the Floquet-Liouville space. Employing the multipole formulation[23,25] of Floquet theory, the polarization transfer among spins in R^2 experiments was described using a set of coupled differential equations corresponding to ZQ coherences of rank 0,1 and 2. Though the approach presents a framework for a complete description of the spin dynamics, the dimension of the problem increases drastically with the number of spins present in the system. This limitation forms the main motivation behind this thesis. To circumvent the problems encountered in other existing treatments, a new analytic method based on the reduced density matrix[28] theory is proposed[29] in this thesis. The framework outlined in this chapter is quite general to any experiment in solid-state NMR and is not limited by the number of spins present in the system. For demonstrative purpose, in this chapter we confine our discussion to the description of R^2 experiments (see Fig. 2.1) in isolated spin pair systems under idealized conditions of heteronuclear decoupling.

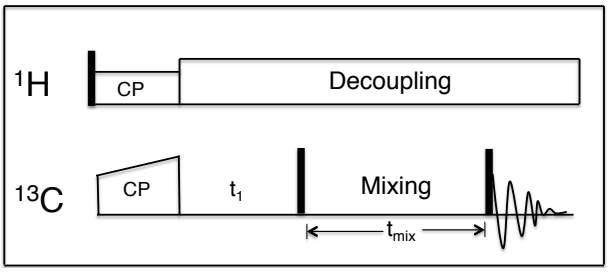

Figure 2.1: Pulse sequence depicting the Rotational resonance (R^2) experiment.

2.2 Definition of the problem

As an alternative to other existing descriptions in the literature, a sophisticated version of the density operator formalism is proposed for describing the dramatic

effects observed under R^2 conditions in MAS experiments. Since, the Hamiltonians under MAS are time-dependent and periodic, Floquet theory[17–25] is employed to describe the underlying spin dynamics. To reduce the complexity in the Floquet description, effective Floquet Hamiltonians[30,31] are derived through the method of contact transformation.[32,33] In general, the polarization transfer among a pair of spins in R^2 experiments is not an isolated phenomenon. To alleviate the complexities encountered in the brute force density matrix calculations (mainly due to the spin dimension of the problem), the concept of reduced density matrix (RDM)[28] is invoked in this thesis. Employing the effective Floquet Hamiltonians (to the desired order of accuracy), effective reduced density matrices for the individual spins are proposed[29] to describe the spin dynamics under R^2 conditions. The advantages of the proposed approach is illustrated below with a rigorous comparison with simulations emerging from exact numerical methods.

2.3 Theory

2.3.1 Description of R^2 in isolated spin pair ($I_1 - I_2$)

To describe the magnetization exchange between ^{13}C nuclei under R^2 conditions, a model system comprising of two-spins (I_1 and I_2) is employed in this section. The time-dependent MAS Hamiltonian for the same is represented by,

$$H(t) = H^{C}_{System}(t) = \sum_{i=1}^{2} \left(\omega_i^{(0)} + \omega_i(t)\right) I_{iz} + \omega_{12}(t) \left(2I_{1z}I_{2z} - \tfrac{1}{2}(I_1^+ I_2^- + I_1^- I_2^+)\right) \tag{2.1}$$

For demonstrative purposes, the residual interactions between neighboring spins are neglected in the present treatment (i.e ideal heteronuclear decoupling is assumed). In the above equation, $\omega_i^{(0)}$ represents the isotropic chemical shift and $\omega_i(t)$, the time-dependent components of the anisotropic interactions (such as chemical shift anisotropy, dipolar interactions) are represented by, $\omega_i(t) = \sum_{m=-2,m\neq 0}^{2} \omega_i^{(m)} e^{im\omega_r t}$. The components of the anisotropic interactions are discussed in chapter-1.

To deduce the R^2 matching conditions, the Hamiltonian in the rotating frame (Eq.(2.1)) is transformed into an interaction frame defined by the transformation

operator, $U_1 = e^{in\omega_r t I_{1z}} e^{-in\omega_r t I_{2z}}$.

$$\begin{aligned}\tilde{H}(t) =& U_1 H(t) U_1^{-1} \\ =& (\omega_1^{(0)} - n\omega_r) I_{1z} + (\omega_2^{(0)} + n\omega_r) I_{2z} + \sum_{i=1}^{2} \sum_{m=-2, m\neq 0}^{2} \omega_i^{(m)} e^{im\omega_r t} I_{iz} + \\ & \sum_{m=-2, m\neq 0}^{2} \omega_{12}^{(m)} \left[2 I_{1z} I_{2z} e^{im\omega_r t} - \frac{1}{2} \left(I_1^+ I_2^- e^{i(m+2n)\omega_r t} + I_1^- I_2^+ e^{i(m-2n)\omega_r t} \right) \right] \end{aligned} \quad (2.2)$$

In the interaction frame, the dipolar interactions (the flip-flop operators) have an additional time-dependence resulting from the transformation operator. When the index 'n' is adjusted to satisfy the conditions $m + 2n = 0$ or $m - 2n = 0$, one of the components of the dipolar flip-operator is time-independent and is responsible for the flip-flop processes observed under R^2 conditions.

To present an accurate description of the spin dynamics, the time-dependent components of the CSA and dipolar interactions have to be incorporated in the description. To this end, we employ an analytic approach based on Floquet theory for describing the spin dynamics under R^2 conditions. In contrast to Average Hamiltonian theory (AHT),[13–15] Floquet theory[17–25] provides a more general framework for describing time-dependent phenomenon in quantum mechanics. In the Floquet formalism, the time-dependent Hamiltonian is transformed into a time-independent Hamiltonian via Fourier series expansion. Employing the Floquet operators (which are constructed from the direct product between the spin and Fourier operator), the time-independent Floquet Hamiltonian is derived. To circumvent the complexity imposed by the infinite dimensionality in the Floquet-space, effective Hamiltonian[30,31] based on the contact transformation procedure[32,33] is employed in the present study. Since the contact transformation is an operator equivalent of the standard Rayleigh-Schrodinger perturbation theory, the Floquet Hamiltonian is split and re-expressed as a sum comprising of a zero-order and a series of perturbing terms arranged in a decreasing order of magnitude.

$$H_F = H_0 + H_1 = H_0 + (H_{1,d} + H_{1,od}) \quad (2.3)$$

In the above equation, $H_{1,d}$ and $H_{1,od}$ represent the diagonal and off-diagonal Floquet Hamiltonians, respectively. The operators that are diagonal in the Fourier dimension

are included along $H_{1,d}$, while the off-diagonal terms are included along $H_{1,od}$.

$$H_0 = \omega_r I_F \tag{2.4}$$

$$H_{1,d} = (\omega_1^{(0)} - n\omega_r)[I_{1z}]_0 + (\omega_2^{(0)} + n\omega_r)[I_{2z}]_0 + G_{12,PM}^{(0)}\left[I_1^+ I_2^-\right]_0 + G_{12,MP}^{(0)}\left[I_1^- I_2^+\right]_0 \tag{2.5}$$

$$H_{1,od} = \sum_{m=-2,m\neq 0}^{2}\sum_{i=1}^{2} G_i^{(m)}[I_{iz}]_m + \sum_{m=-2,m\neq 0}^{2} G_{12}^{(m)}[I_{1z}I_{2z}]_m + \sum_{m=-2,m\neq 0}^{2}\left(G_{12,PM}^{(m+2n)}\left[I_1^+ I_2^-\right]_{m+2n} + G_{12,MP}^{(m-2n)}\left[I_1^- I_2^+\right]_{m-2n}\right) \tag{2.6}$$

The I_F operator in Eq. (2.4) represents the identity operator in the infinite dimensional Floquet space (i.e. $I_F = \sum_{n=-\infty}^{\infty} n\,|n\rangle\langle n|$, where $|n\rangle$ represents the Fourier ket). In a similar vein, the Floquet spin operators are constructed by taking the direct product between the spin (I_α) and Fourier operators (i.e. $[I_\alpha]_m = I_\alpha \otimes \sum_{n=-\infty}^{\infty} |n\rangle\langle n+m|$). The notations and conventions are very similar to the one that is employed in reference [23].

The choice of the zero-order and perturbing Hamiltonians play an important role in determining the accuracy of the predictions /results emerging from analytic treatments based on effective Hamiltonians. In the present description, the time-independent component of the dipolar Hamiltonian (containing the flip-flop operators) is included as a diagonal term in the perturbation, H_1. The non-zero coefficients in the Floquet Hamiltonian are tabulated in Tables 2.1 & 2.2. In the contact transformation procedure, the above Floquet Hamiltonian (Eq. 2.3) is transformed by a single or a series of unitary transformations. In the present study, a single unitary transformation defined by S_1 is employed as illustrated below.

$$H_{eff} = e^{i\lambda S_1} H_F e^{-i\lambda S_1} = H_0^{(1)} + H_1^{(1)} + H_2^{(1)} + ... \tag{2.7}$$

In contrast to the Rayleigh-Schrodinger perturbation theory, the perturbation corrections in the contact transformation procedure are obtained in terms of operators (as opposed to matrix elements) resulting in effective Hamiltonians. Employing BCH (Baker-Campbell-Hausdorff) expansion and combining like terms, the various orders of correction to the effective Hamiltonians are derived systematically as illustrated

below.

$$\begin{aligned} H_0^{(1)} =& H_0 \\ H_1^{(1)} =& H_1 + i\left[S_1, H_0\right] \\ H_2^{(1)} =& H_2 + i\left[S_1, H_1\right] - \frac{1}{2}\left[S_1\left[S_1, H_0\right]\right] \end{aligned} \tag{2.8}$$

In the above equation, $H_n^{(1)}$ denotes the effective Hamiltonian to order 'n' derived from the first transformation (S_1). The transformation function, S_1 plays an important role in the effectiveness of the method and is carefully chosen to compensate the off-diagonality in $H_{1,od}$.

$$\begin{aligned} S_1 = & \sum_{m=-2,m\neq 0}^{2} i\left\{\sum_{i=1}^{2} C_i^{(m)}[I_{iz}]_m + C_{12}^{(m)}[I_{1z}I_{2z}]_m\right\}+ \\ & \sum_{m=-2,m\neq 0}^{2} i\left\{C_{12,PM}^{(m+2n)}\left[I_1^+ I_2^-\right]_{m+2n} + C_{12,MP}^{(m-2n)}\left[I_1^- I_2^+\right]_{m-2n}\right\} \end{aligned} \tag{2.9}$$

The 'G' and 'C' coefficients employed in the Floquet Hamiltonian and the transformation function, S_1 are tabulated in Tables 2.1 and 2.2.

N=1, R^2	
$G_i^{(m)} = \omega_i^{(m)}$	$G_{ij}^{(m)} = 2\omega_{ij}^{(m)}$
$G_{(12/13),PM}^{(3)} = -\frac{1}{2}\omega_{(12/13)}^{(2)}$	$G_{(12/13),MP}^{(1)} = -\frac{1}{2}\omega_{(12/13)}^{(2)}$
$G_{(12/13),PM}^{(-1)} = -\frac{1}{2}\omega_{(12/13)}^{(-2)}$	$G_{(12/13),MP}^{(-3)} = -\frac{1}{2}\omega_{(12/13)}^{(-2)}$
$G_{(12/13),PM}^{(2)} = -\frac{1}{2}\omega_{(12/13)}^{(1)}$	$G_{(12/13),MP}^{(0)} = -\frac{1}{2}\omega_{(12/13)}^{(1)}$
$G_{(12/13),PM}^{(0)} = -\frac{1}{2}\omega_{(12/13)}^{(-1)}$	$G_{(12/13),MP}^{(-2)} = -\frac{1}{2}\omega_{(12/13)}^{(-1)}$
$G_{23,PM}^{(m)} = -\frac{1}{2}\omega_{23}^{(m)}$	$G_{23,MP}^{(m)} = -\frac{1}{2}\omega_{23}^{(m)}$
$C_i^{(m)} = \frac{G_i^{(m)}}{m\omega_r}$	$C_{ij}^{(m)} = \frac{G_{ij}^{(m)}}{m\omega_r}$
$C_{ij,PM}^{(m)} = \frac{G_{ij,PM}^{(m)}}{m\omega_r}$	$C_{ij,MP}^{(m)} = \frac{G_{ij,MP}^{(m)}}{m\omega_r}$

Table 2.1: The table depicts the G and C-coefficients involved in the Floquet Hamiltonian and the transformation function, S_1, for N=1 R^2 condition.

N=2, R^2	
$G_i^{(m)} = \omega_i^{(m)}$	$G_{ij}^{(m)} = 2\omega_{ij}^{(m)}$
$G_{(12/13),PM}^{(4)} = -\frac{1}{2}\omega_{(12/13)}^{(2)}$	$G_{(12/13),MP}^{(0)} = -\frac{1}{2}\omega_{(12/13)}^{(2)}$
$G_{(12/13),PM}^{(0)} = -\frac{1}{2}\omega_{(12/13)}^{(-2)}$	$G_{(12/13),MP}^{(-4)} = -\frac{1}{2}\omega_{(12/13)}^{(-2)}$
$G_{(12/13),PM}^{(3)} = -\frac{1}{2}\omega_{(12/13)}^{(1)}$	$G_{(12/13),MP}^{(-1)} = -\frac{1}{2}\omega_{(12/13)}^{(1)}$
$G_{(12/13),PM}^{(1)} = -\frac{1}{2}\omega_{(12/13)}^{(-1)}$	$G_{(12/13),MP}^{(-3)} = -\frac{1}{2}\omega_{(12/13)}^{(-1)}$
$G_{23,PM}^{(m)} = -\frac{1}{2}\omega_{23}^{(m)}$	$G_{23,MP}^{(m)} = -\frac{1}{2}\omega_{23}^{(m)}$
$C_i^{(m)} = \frac{G_i^{(m)}}{m\omega_r}$	$C_{ij}^{(m)} = \frac{G_{ij}^{(m)}}{m\omega_r}$
$C_{ij,PM}^{(m)} = \frac{G_{ij,PM}^{(m)}}{m\omega_r}$	$C_{ij,MP}^{(m)} = \frac{G_{ij,MP}^{(m)}}{m\omega_r}$

Table 2.2: The table depicts the G and C-coefficients involved in the Floquet Hamiltonian and the transformation function, S_1, for N=2 R^2 condition.

Following the procedure described above, the second order corrections (refer Table 2.3 for more details) are evaluated and the effective Hamiltonian to second-order is derived.

$$\begin{aligned} H_{eff} &= H_0^{(1)} + H_1^{(1)} + H_2^{(1)} \\ H_1^{(1)} &= H_{1,d} \\ H_2^{(1)} &= \frac{i}{2}\left[S_1, H_{1,od}\right] \end{aligned} \tag{2.10}$$

As depicted in Eq. 2.10, the effective Floquet Hamiltonian comprises of corrections to both single-spin (longitudinal) and two-spin flip-flop operators.

$$H_{eff} = \omega_r I_F + \sum_{i=1}^{2} A_i [I_{iz}]_0 + \left[D_{12,PM}\left[I_1^+ I_2^-\right]_0 + D_{12,MP}\left[I_1^- I_2^+\right]_0\right] \tag{2.11}$$

In contrast to the untransformed Floquet Hamiltonian (Eq. 2.3), the effective Floquet Hamiltonian described above is block-diagonal in the Floquet-space. Following the standard procedure described in the literature,[23,26,27] the spin dynamics in the Floquet-space is confined to the super block corresponding to the Fourier index (n=0).

The validity of these approximations have been well tested with experimental results and have been employed in the present study.

In the brute force density matrix approach, the dimension of the problem increases with the spin dimension. For e.g. in the case of a two-spin system, the density matrix is described by a matrix of dimension 4 x 4. To minimize this complexity and provide additional insights, we employ the reduced density matrix approach. As described in chapter-1, in the reduced density matrix approach, the reduced density matrix for a particular spin 'i' is constructed from the complete density matrix by taking the partial trace over all other unobserved spins in the description. In the present case, the complete density matrix in the Floquet-space is evaluated by the following expression.

$$\rho(t) = e^{-\frac{i}{\hbar}H_{eff}t}\rho(0)e^{\frac{i}{\hbar}H_{eff}t} \tag{2.12}$$

Subsequently, the reduced density matrix for spin-1 ($\rho(1,t)$) is calculated by taking the trace over the spin-2.

$$\rho(1,t) = \begin{bmatrix} \sum_{i=1}^{2} \rho_{\alpha_1\Phi_i^{(1)},\alpha_1\Phi_i^{(1)}}(t) & \sum_{i=1}^{2} \rho_{\alpha_1\Phi_i^{(1)},\beta_1\Phi_i^{(1)}}(t) \\ \sum_{i=1}^{2} \rho_{\beta_1\Phi_i^{(1)},\alpha_1\Phi_i^{(1)}}(t) & \sum_{i=1}^{2} \rho_{\beta_1\Phi_i^{(1)},\beta_1\Phi_i^{(1)}}(t) \end{bmatrix} \tag{2.13}$$

In the above equation, $\rho_{\alpha_1\Phi_i^{(1)},\alpha_1\Phi_i^{(1)}}(t)$ represents the matrix element $\left\langle \alpha_1\Phi_i^{(1)} \right| \rho(t) \left| \alpha_1\Phi_i^{(1)} \right\rangle$ with $\Phi_i^{(1)}$ representing the spin state of the second spin, I_2 (say $\Phi_1^{(1)} = |\alpha_2\rangle, \Phi_2^{(1)} = |\beta_2\rangle$) with the superscript denoting the total number of spins other than the one observed (say I_1, in this example).

$$\rho(1,t) = \begin{bmatrix} 1 - \frac{|D_{12}|^2}{x^2}\sin^2 xt & 0 \\ 0 & -(1 - \frac{|D_{12}|^2}{x^2}\sin^2 xt) \end{bmatrix} \tag{2.14}$$

In a similar vein, the reduced density matrix for spin I_2 ($\rho(2,t)$) is derived by taking the partial trace over the spin states corresponding to I_1.

$$\rho(2,t) = \begin{bmatrix} \sum_{i=1}^{2} \rho_{\Phi_i^{(1)}\alpha_2,\Phi_i^{(1)}\alpha_2}(t) & \sum_{i=1}^{2} \rho_{\Phi_i^{(1)}\alpha_2,\Phi_i^{(1)}\beta_2}(t) \\ \sum_{i=1}^{2} \rho_{\Phi_i^{(1)}\beta_2,\Phi_i^{(1)}\alpha_2}(t) & \sum_{i=1}^{2} \rho_{\Phi_i^{(1)}\beta_2,\Phi_i^{(1)}\beta_2}(t) \end{bmatrix}$$

$$= \begin{bmatrix} \frac{|D_{12}|^2}{x^2}\sin^2 xt & 0 \\ 0 & -\frac{|D_{12}|^2}{x^2}\sin^2 xt \end{bmatrix} \tag{2.15}$$

In the present study, polarization transfer is calculated from spin I_1 to I_2 (i.e. $\rho(0) = I_{1z}$). In contrast to the standard description, the expectation value of the desired observable in the reduced density matrix approach is calculated by employing only the corresponding reduced density operator as illustrated below.

$$\langle O_I(t)\rangle = Tr[\rho(I,t).O_I] \tag{2.16}$$

Subsequently, the polarization transfer from spin I_1 to I_2 under R^2 conditions is calculated by evaluating $\langle I_z\rangle$, as illustrated below.

$$\langle I_{1z}(t)\rangle = 1 - \frac{|D_{12}|^2}{x^2}\sin^2 xt \tag{2.17}$$

$$\langle I_{2z}(t)\rangle = \frac{|D_{12}|^2}{x^2}\sin^2 xt \tag{2.18}$$

In the above equations, the coefficient 'x' comprises of the dipolar and chemical shift offset terms i.e. $x = \sqrt{|D_{12}|^2 + \left(\frac{(A_1 - A_2)}{2}\right)^2}$.

At the exact R^2 conditions, the dominant first-order contributions contained in single-spin operators tend to zero (see Table 2.3) resulting in maximum transfer of polarization. Far from the R^2 matching conditions, the contributions from the single-spin operators dominate and decrease the efficiency of transfer. The result depicted in Eq. 2.18, resembles to the one derived by Rabi[34] for an isolated two-level system. In contrast to other analytic methods, the analytic expressions (Eq. 2.17 & 2.18) are computationally less intense and provide a better picture of the resonance phenomenon in R^2 experiments.

2.3.2 Description of R^2 in three-spin ($I_1 - I_2 - I_3$) system

The next stage in our study was to describe the multi-spin effects arising from a neighbouring carbon, a situation often encountered in band-selective transfer of polarization in R^2 experiments. To this end, a model system comprising of three carbons was employed in the present study. The Hamiltonian for such a system is represented by,

$$H(t) = \sum_{i=1}^{3}\left(\omega_i^{(0)} + \omega_i(t)\right) I_{iz} + \sum_{i,j=1;i<j}^{3} \omega_{ij}(t)\left(2I_{iz}I_{jz} - \frac{1}{2}(I_i^+ I_j^- + I_i^- I_j^+)\right) \tag{2.19}$$

Accordingly, the above spin Hamiltonian is transformed into an interaction frame through an unitary transformation, $U_1 = e^{in\omega_r t I_{1z}} e^{-in\omega_r t I_{2z}} e^{-in\omega_r t I_{3z}}$. The transformed

Hamiltonian in the interaction frame is represented by, $\tilde{H}(t) = U_1 H(t) U_1^{-1}$.

$$\begin{aligned}\tilde{H}(t) =&(\omega_1^{(0)} - n\omega_r)I_{1z} + (\omega_2^{(0)} + n\omega_r)I_{2z} + (\omega_3^{(0)} + n\omega_r)I_{3z} + \sum_{i=1}^{3}\omega_i^{(m)}e^{im\omega_r t}I_{iz} \\ &\sum_{m=-2,m\neq 0}^{2}\omega_{12}^{(m)}\left[2I_{1z}I_{2z}e^{im\omega_r t} - \frac{1}{2}\left(I_1^+ I_2^- e^{i(m+2n)\omega_r t} + I_1^- I_2^+ e^{i(m-2n)\omega_r t}\right)\right] + \\ &\sum_{m=-2,m\neq 0}^{2}\omega_{13}^{(m)}\left[2I_{1z}I_{3z}e^{im\omega_r t} - \frac{1}{2}\left(I_1^+ I_3^- e^{i(m+2n)\omega_r t} + I_1^- I_3^+ e^{i(m-2n)\omega_r t}\right)\right] + \\ &\sum_{m=-2,m\neq 0}^{2}\omega_{23}^{(m)}e^{im\omega_r t}\left[2I_{2z}I_{3z} - \frac{1}{2}\left(I_2^+ I_3^- + I_2^- I_3^+\right)\right] \qquad (2.20)\end{aligned}$$

As described in the previous case, the above Hamiltonian is transformed into a time-independent Floquet Hamiltonian in which the zero order and the perturbation terms are represented by

$$H_0 = \omega_r I_F \qquad (2.21)$$

$$\begin{aligned}H_{1,d} =&(\omega_1^{(0)} - n\omega_r)[I_{1z}]_0 + (\omega_2^{(0)} + n\omega_r)[I_{2z}]_0 + (\omega_3^{(0)} + n\omega_r)[I_{3z}]_0 + \\ &\sum_{i=2}^{3}\left(G_{1i,PM}^{(0)}\left[I_1^+ I_i^-\right]_0 + G_{1i,MP}^{(0)}\left[I_1^- I_i^+\right]_0\right) \qquad (2.22)\end{aligned}$$

$$\begin{aligned}H_{1,od} =& \sum_{m=-2,m\neq 0}^{2}\sum_{i=1}^{3}G_i^{(m)}[I_{iz}]_m + \sum_{i,j=1,i<j}^{3}\sum_{m=-2,m\neq 0}^{2}G_{ij}^{(m)}[I_{iz}I_{jz}]_m + \\ &\sum_{i=2}^{3}\sum_{m=-2,m\neq 0}^{2}\left(G_{1i,PM}^{(m+2n)}\left[I_1^+ I_i^-\right]_{m+2n} + G_{1i,MP}^{(m-2n)}\left[I_1^- I_i^+\right]_{m-2n}\right) + \\ &\sum_{m=-2,m\neq 0}^{2}\left(G_{23}^{(m)}\left[I_2^+ I_3^-\right]_m + G_{23}^{(m)}\left[I_2^- I_3^+\right]_m\right) \qquad (2.23)\end{aligned}$$

The transformation function, S_1 (off-diagonal) is chosen to compensate the off-diagonal terms present in $H_{1,od}$ as represented below.

$$\begin{aligned}S_1 =& \sum_{m=-2,m\neq 0}^{2}\sum_{i=1}^{3}C_i^{(m)}[I_{iz}]_m + \sum_{i,j=1,i<j}^{3}\sum_{m=-2,m\neq 0}^{2}C_{ij}^{(m)}[I_{iz}I_{jz}]_m + \\ &\sum_{i=2}^{3}\sum_{m=-2,m\neq 0}^{2}\left(C_{1i,PM}^{(m+2n)}\left[I_1^+ I_i^-\right]_{m+2n} + C_{1i,MP}^{(m-2n)}\left[I_1^- I_i^+\right]_{m-2n}\right) + \\ &\sum_{m=-2,m\neq 0}^{2}\left(C_{23,PM}^{(m)}\left[I_2^+ I_3^-\right]_m + C_{23,MP}^{(m)}\left[I_2^- I_3^+\right]_m\right) \qquad (2.24)\end{aligned}$$

The 'G and C' coefficients involved in the Floquet Hamiltonian and the transformation function, S_1 are tabulated in Tables 2.1 and 2.2. Following the procedure described, the effective Floquet Hamiltonian for the model three-spin system is derived and represented below and see Table 2.3 for all the corrections depicted in

H_{eff}.

$$H_{eff} = \sum_{i=1}^{3} A_i I_{iz} + \sum_{j=2}^{3} \left[D_{1j,PM} I_1^+ I_j^- + D_{1j,MP} I_1^- I_j^+ \right] \tag{2.25}$$

Employing the the reduced density matrix formalism, the polarization transfer from spin I_1 to I_2 and I_3 is calculated and expressed in terms of analytic expressions given below.

$$\langle I_{1z}(t) \rangle = 1 - \frac{|D_{12}|^2}{x_{1,(12)}{}^2} \sin^2 x_{1,(12)} t - \frac{|D_{13}|^2}{x_{1,(13)}{}^2} \sin^2 x_{1,(13)} t \tag{2.26}$$

$$\langle I_{2z}(t) \rangle = \frac{|D_{12}|^2}{x_{1,(12)}{}^2} \sin^2 x_{1,(12)} t \tag{2.27}$$

$$\langle I_{3z}(t) \rangle = \frac{|D_{13}|^2}{x_{1,(13)}{}^2} \sin^2 x_{1,(13)} t \tag{2.28}$$

The 'x' coefficients in the above equations have the following definitions.

$$x_{1,(12)} = \sqrt{|D_{12}|^2 + \left(\frac{(A_1 - A_2)}{2} \right)^2} \tag{2.29}$$

$$x_{1,(13)} = \sqrt{|D_{13}|^2 + \left(\frac{(A_1 - A_3)}{2} \right)^2} \tag{2.30}$$

2.4 Results and Discussion

To substantiate the analytic theory and demonstrate its utility in the interpretation /analysis of R^2 experiments, the dipeptide N-acetyl- (U-^{13}C,^{15}N) -L-valine-L-leucine (VL) was employed (Fig. 2.2) as a model system in our studies. Being a prototype of a typical biological system, such model systems have been routinely employed in the past for testing NMR methodologies and pulse schemes. To illustrate the magnetization exchange under R^2 conditions, the model system depicted in Figure 2.2 is further split into smaller models (see Figure 2.3), representative of the strong, intermediate and weak coupling regimes encountered in R^2 experiments.

The simulations depicted in Figures 2.4 and 2.5 represent R^2 simulations in a powder sample. The powder simulations were performed using a three-angle Euler set (ZCW) comprising of 6044 crystallite orientations. The analytic expressions derived in Eqs. 2.17 & 2.18 were employed in the present study. To test the validity of the analytic simulations, simulations emerging from exact numerical methods (SPIN EVOLUTION) were employed in the present study.

Coefficients	**First - order**	**Second - order**
A_1	$\left(\omega_1^{(0)} - n\omega_r\right)$	$\underbrace{\frac{1}{2}\left(C_{12,PM}^{(m)}G_{12,MP}^{(-m)} - C_{12,MP}^{(m)}G_{12,PM}^{(-m)}\right) + \frac{1}{2}\left(C_{13,PM}^{(m)}G_{13,MP}^{(-m)} - C_{13,MP}^{(m)}G_{13,PM}^{(-m)}\right)}_{\text{Dipolar}(^{13}C-^{13}C)\times\text{Dipolar}(^{13}C-^{13}C)}$
A_2	$\left(\omega_2^{(0)} + n\omega_r\right)$	$\underbrace{-\frac{1}{2}\left(C_{12,PM}^{(m)}G_{12,MP}^{(-m)} - C_{12,MP}^{(m)}G_{12,PM}^{(-m)}\right)}_{\text{Dipolar}(^{13}C-^{13}C)\times\text{Dipolar}(^{13}C-^{13}C)}$
A_3	$\left(\omega_3^{(0)} + n\omega_r\right)$	$\underbrace{-\frac{1}{2}\left(C_{13,PM}^{(m)}G_{13,MP}^{(-m)} - C_{13,MP}^{(m)}G_{13,PM}^{(-m)}\right)}_{\text{Dipolar}(^{13}C-^{13}C)\times\text{Dipolar}(^{13}C-^{13}C)}$
$D_{12,PM}$	$-\frac{1}{2}\omega_{12}^{(k)}$	$\underbrace{\frac{1}{2}\left(C_1^{(m)}G_{12,PM}^{(-m)} - C_{12,PM}^{(m)}G_1^{(-m)}\right) - \frac{1}{2}\left(C_2^{(m)}G_{12,PM}^{(-m)} - C_{12,PM}^{(m)}G_2^{(-m)}\right)}_{\text{CSA}(^{13}C)\times\text{Dipolar}(^{13}C-^{13}C)}$
$D_{12,MP}$	$-\frac{1}{2}\omega_{12}^{(k)}$	$\underbrace{-\frac{1}{2}\left(C_1^{(m)}G_{12,MP}^{(-m)} - C_{12,MP}^{(m)}G_1^{(-m)}\right) + \frac{1}{2}\left(C_2^{(m)}G_{12,MP}^{(-m)} - C_{12,MP}^{(m)}G_2^{(-m)}\right)}_{\text{CSA}(^{13}C)\times\text{Dipolar}(^{13}C-^{13}C)}$
$D_{13,PM}$	$-\frac{1}{2}\omega_{13}^{(k)}$	$\underbrace{\frac{1}{2}\left(C_1^{(m)}G_{13,PM}^{(-m)} - C_{13,PM}^{(m)}G_1^{(-m)}\right) - \frac{1}{2}\left(C_3^{(m)}G_{13,PM}^{(-m)} - C_{13,PM}^{(m)}G_3^{(-m)}\right)}_{\text{CSA}(^{13}C)\times\text{Dipolar}(^{13}C-^{13}C)}$
$D_{13,MP}$	$-\frac{1}{2}\omega_{13}^{(k)}$	$\underbrace{-\frac{1}{2}\left(C_1^{(m)}G_{13,MP}^{(-m)} - C_{13,MP}^{(m)}G_1^{(-m)}\right) + \frac{1}{2}\left(C_3^{(m)}G_{13,MP}^{(-m)} - C_{13,MP}^{(m)}G_3^{(-m)}\right)}_{\text{CSA}(^{13}C)\times\text{Dipolar}(^{13}C-^{13}C)}$

Table 2.3: The table depicts the first-order and second-order corrections (for N=1 & 2 conditions) involved in the effective Hamiltonians (Eqns. 2.11 and 2.25). Depending on the matching conditions ($|\upsilon_1 - \upsilon_2| = N\upsilon_R$), the "k" indices are (a) N=1 (n=1/2): k= -1 and +1 (b) N=2 (n=1): k= -2 and +2 for $D_{12(13),PM}$ and $D_{12(13),MP}$ respectively. The 'G' and 'C' coefficients in the above table are identical to those listed in Tables 2.1 & 2.2.

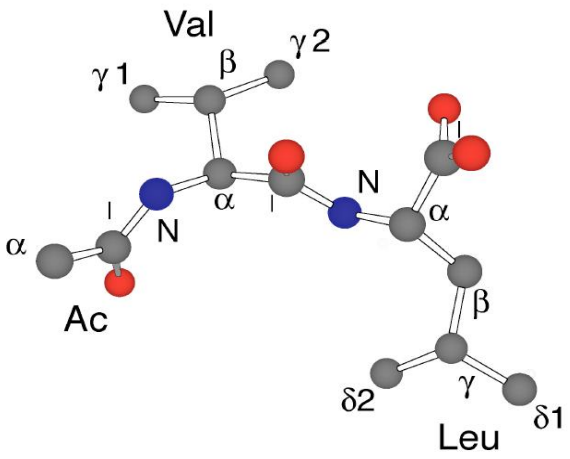

Figure 2.2: Schematic diagram of N-Acetyl-L-Valine-L-Leucine derived from the crystal structure[35].

We begin with simulations depicting the polarization transfer from spin I_1 to I_2. In the mixing time experiments, the polarization transfer is monitored as a function of mixing time under constant spinning frequency. As depicted in Figures 2.4 & 2.5, the polarization transfer profile is oscillatory in nature. This behavior is substantiated by the analytic expressions (Eqs. 2.17 & 2.18) presented in the previous section. When the magnitude of the dipolar coupling increases, the dipolar oscillations increase and the time of equilibration between the spin polarizations decreases in time (i.e. the polarization between the spins equilibrate at shorter mixing times). In contrast to the profile depicted in Fig. 2.4, the dipolar oscillations in the N=2 matching condition (Fig. 2.5) are highly oscillatory and tend to equilibrate at longer mixing times. This trend is prominent in the medium and weaker coupling regimes (panels b1, c1 in Fig. 2.5). The analytic expressions depicting the polarization transfer resemble to those derived by Rabi[34] for describing transition possibilities in a two-level system. In the original description by Rabi , the transition probability from the ground state to the excited state was calculated using time-dependent perturbation theory. In the absence of dissipation, the transition probabilities oscillate back and forth without any drop in intensity. To mimic the observations observed in experiments, Rabi proposed an approach of including an exponential damping term (exp(-t/T)) along the calculated transition probabilities. Depending on the magnitude of the damping

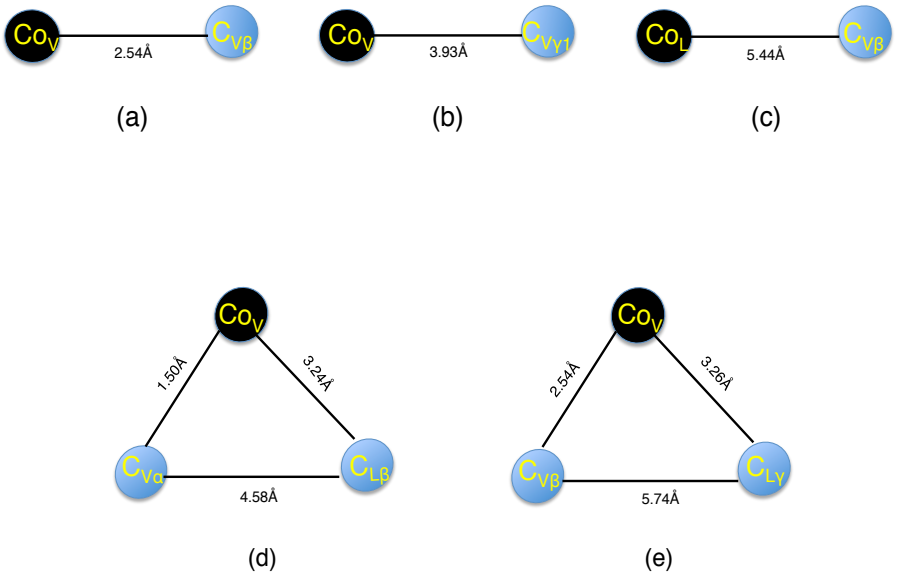

Figure 2.3: Model systems constructed from Fig. 2.2 for describing the polarization transfer in R^2 experiments among ^{13}C nuclei. The models depicted in panels (a), (b) and (c) resemble the $I_1 - I_2$ system and correspond to the strong, intermediate and weak-coupling regimes, respectively. The models depicted in panels (d) and (e) are representative of the $I_1 - I_2 - I_3$ system. The dipolar coupling constants between spin pairs are depicted in all the models.

terms, the transitions probabilities oscillate with a decrease in their amplitude with time.

Interestingly, the dipolar oscillations in the polarization transfer profile depicted in Figures 2.4 & 2.5 decrease with time. At the outset, this result (emerging from simulations) seems intriguing and counter intuitive owing to the fact that the system under consideration is an isolated two-spin system and resembles very much to the two-level system employed by Rabi in his calculations. This discrepancy results from the spatial anisotropy of the dipolar interactions in the solid-state. In a typical polycrystalline sample, due to restricted mobility, the dipolar coupling constants vary across the sample and interference effects emerging from different spin pairs (of the same kind) are responsible for the damping observed in the profiles depicted in Figures 2.4 & 2.5. To the best of our knowledge, such a description of the R^2 phenomenon does not exist in the literature.

To justify this explanation, simulations employing a single orientation are de-

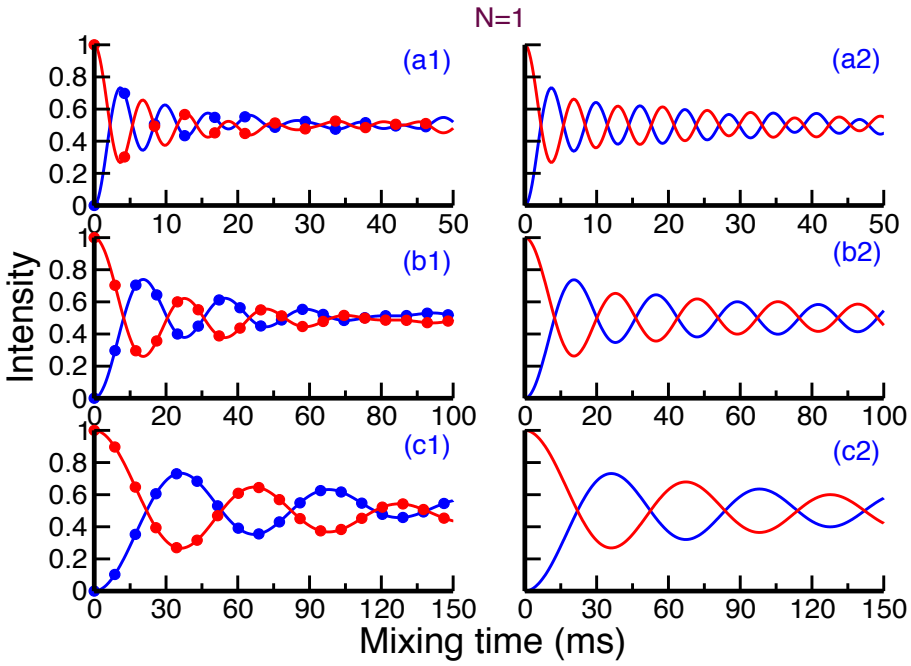

Figure 2.4: The figure depicts the polarization transfer between ^{13}C nuclei in a two-spin system (from spin-1 (red) to spin-2 (blue)) as a function of mixing time under constant spinning frequency (N=1, R^2 condition) with powder averaging. For illustrative purposes, polarization transfer in the strong ($V_{Co} \rightarrow V_{C\beta}$, 2.54 Å; panels: a1, a2), intermediate ($V_{Co} \rightarrow V_{C\gamma_1}$, 3.90 Å; panels: b1, b2) and weak ($Leu_{Co} \rightarrow V_{C\beta}$, 5.44 Å; panels: c1, c2) coupling regimes are depicted. The role of CSA contributions (absent) is highlighted in panels (a2, b2, c2). The analytic simulations (based on Eqs. (2.17) & (2.18)) are depicted through dots, while the numerical simulations are denoted by solid lines. All the simulation parameters are given in Table 2.4.

picted in Fig. (2.6). As depicted in this figure, in the absence of powder averaging (contributions from all crystallites), the polarization transfer oscillates back and forth without any damping. In accord with the simulations depicted in Figures 2.4 & 2.5, the frequency of oscillations decrease with the dipolar coupling constant. Hence, the damping observed in a typical polycrystalline sample could be interpreted as an interference effect (i.e. superposition of different sine curves) emerging from dipolar coupling constants associated with different crystallite orientations. In contrast to other existing descriptions, the present approach provides a framework for unravelling the phenomenon of decoherence frequently encountered in SSNMR experiments involving powder samples. Since, a real system comprises of other interactions result-

CSA Parameters							
Spin 1	**δ (ppm)**	**η**	**Ω_{PM} (deg)**	**Spin 2**	**δ (ppm)**	**η**	**Ω_{PM} (deg)**
V_{Co}	68.3	1.0	(160, 33, 90) (137, 25, 105) (160, 33, 90) (-100, 23, 047) (-132, 35, -4)	$V_{C\beta}$ $V_{C\gamma1}$ $V_{C\alpha}$ $L_{C\beta}$ $L_{C\gamma}$	11.3 -15.3 11.3 24.0 11.3	0.91 0.0 0.91 0.92 0.91	(119, 94, -13) (-41, 26, 48) (119, 94, -13) (-49, 48, -170) (138, 88, -75)
L_{Co}	-67.6	0.99	(104, 50, 130)	$V_{C\beta}$	11.3	0.91	(148, 89, -75)

Spin pair (^{13}C)	**Chemical shift difference (kHz)**
V_{Co} - $V_{C\beta}$	18
V_{Co} - $V_{C\gamma1}$	19
L_{Co} - $V_{C\beta}$	18
V_{Co} - $V_{C\alpha}$; V_{Co} - $L_{C\beta}$	15, 17
V_{Co} - $V_{C\beta}$; V_{Co} - $L_{C\gamma}$	18, 18.2

Table 2.4: The figure depicts the CSA and chemical shift parameters (Ref. 26) of the models depicted in Figure 2.3, used in various simulations in this thesis.

ing from insufficient heteronuclear decoupling, Levitt et al[12] introduced the inclusion of a phenomenological damping term (T_{ZQ}) to account for the depolarization (due to insufficient decoupling) observed in R^2 experiments.

In the model presented in this chapter, the damping observed in experiments could be incorporated by including an exponential damping term (as proposed by Rabi) along the final expressions in the calculations presented in the previous section (see Eqs. 2.17 & 2.18). As illustrated in Figure 2.7, inclusion of the exponential damping term decreases the intensity and amplitude of the oscillations. Although such phenomenological models yield results that resemble to those obtained from experiments, the physical basis for such effects needs to be investigated in greater detail. Additionally, from a conceptual viewpoint, inclusion of a uniform damping term for all the spin pairs in a polycrystalline sample seems highly inappropriate and unjustifiable. A more rigorous description incorporating the effects of neighboring protons will be presented in chapter-3. As depicted in Fig. 2.7, the observed damping seems to be drastic in the weak coupling regime. Since long range distances (>4Å)

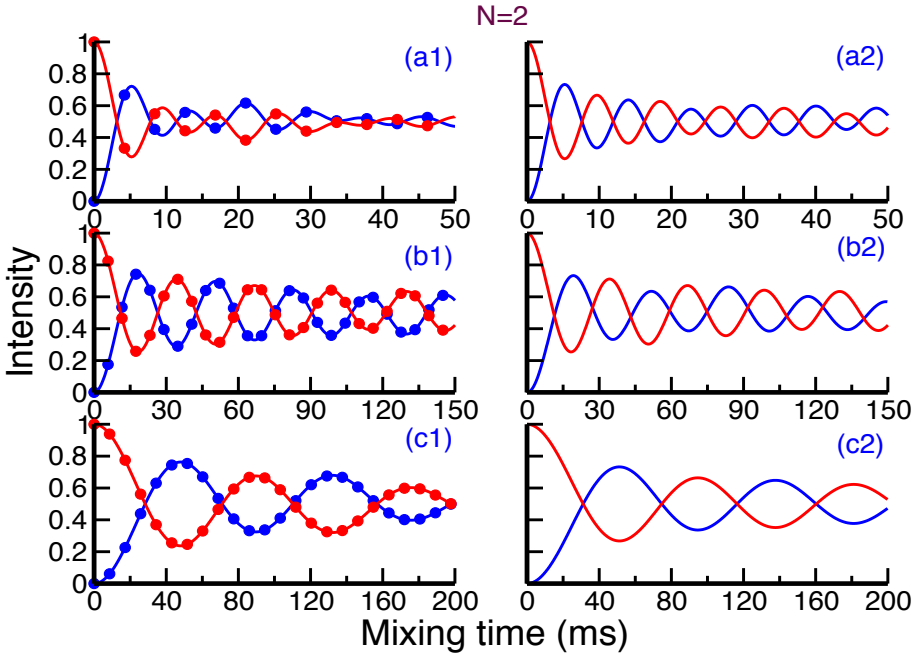

Figure 2.5: The figure depicts the polarization transfer between ^{13}C nuclei in a two-spin system (from spin-1 (red) to spin-2 (blue)) as a function of mixing time under constant spinning frequency (N=2, R^2 condition) with powder averaging. The role of CSA contributions (absent) is highlighted in panels (a2, b2, c2) and the description is similar to which is given in Figure 2.4. All the simulation parameters are given in Table 2.4.

yield important constraints in refining the side chain orientations, careful analysis of such schemes is very essential at least in the weak coupling regime.

As an alternative to mixing time experiments, Costa et al[36] proposed a method (Rotational resonance width, R^2W) wherein, the magnetization exchange is monitored as a function of sample spinning frequency under constant mixing times. The constant time experiments were presumably designed to minimize the effects of relaxation in the data analysis of R^2 experiments. In Figures 2.8 & 2.9, polarization transfer in R^2W experiment is described both for the N=1 and N=2 condition. As depicted, the width of the resonance (off-resonance magnetization exchange) increases with an increase in the coupling constant and is maximum for the N=1, R^2 condition. Far away from the R^2 condition, the detuning effect introduced by the longitudinal single-spin operators ($\omega_1 - \omega_2 + 2n\omega_r$) increases and decreases the efficiency of transfer. This effect is very similar to the detuning frequency ($\Omega = \omega - \omega_0$) defined by Rabi with regard to the transitions observed in a two-level system. As depicted, in the

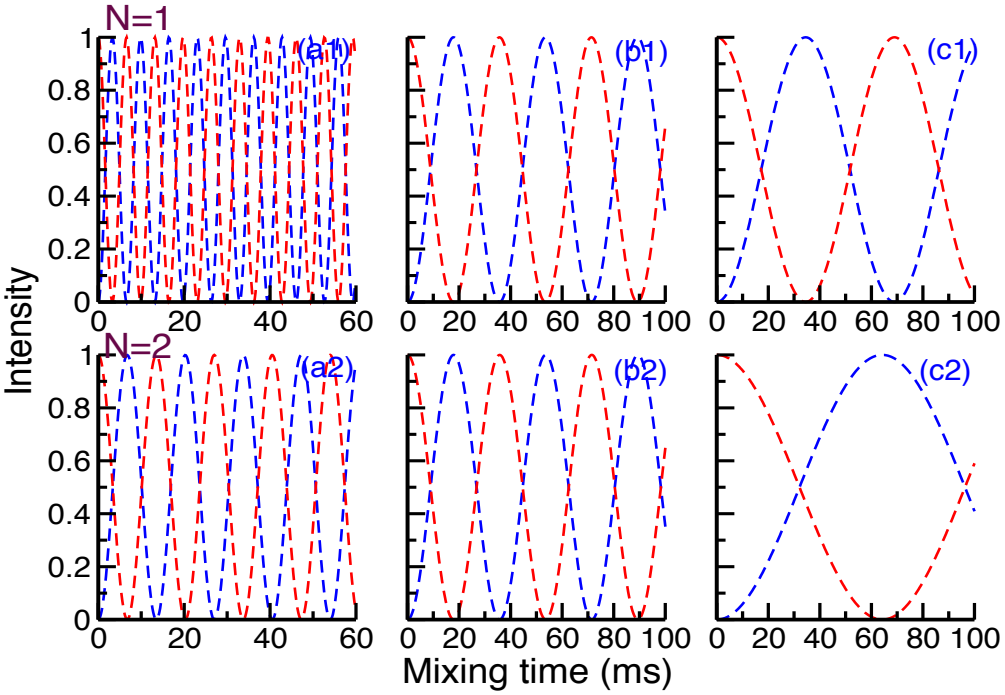

Figure 2.6: The simulations depict the polarization transfer observed in a two-spin system in R^2 experiments (both N=1 & 2) when powder averaging is ignored. In the absence of powder averaging, the polarization exchange is oscillatory and resembles to the famous Rabi oscillations. Additionally, the oscillations are periodic and undamped. All the simulation parameters are similar to those given in Fig. 2.4 and Table 2.4.

absence of the CSA interactions (see panels (a2, b2, c2) in Figures 2.4, 2.5, 2.8 & 2.9), the efficiency of transfer more or less seems unaffected. However, at higher magnetic field strengths, the second-order cross terms between CSA and dipolar interactions might reduce the efficiency of transfer between the spin pair. As discussed earlier, the inclusion of experimental damping just decreases the efficiency of transfer (Fig. 2.10).

The next stage in our study was to elucidate the role of the neighbouring carbons in the R^2 exchange dynamics. In the band-selective transfer of polarization from carbonyl carbon to aliphatic carbons, there could be an overlap of the R^2 matching conditions. In the simulations depicted in Figures 2.11 & 2.12, polarization transfer from I_1 (representative of the carbonyl carbon) to I_2, I_3 (representative of the carbons in the aliphatic region) is depicted. Since, the chemical shifts of the carbons in the aliphatic region are very similar, only band-selective transfer of polarization is

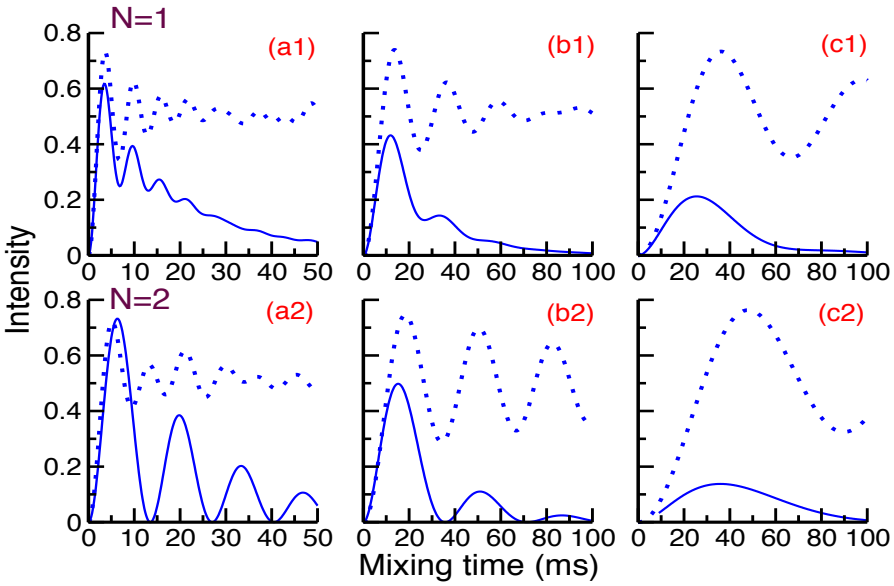

Figure 2.7: The figure depicts the role of phenomenological damping terms (solid line) on the magnetization transfer observed in R^2 experiments (both N=1 & 2). The following damping parameters have been included in the simulations: T_{ZQ}=21ms (panels: a1, a2), T_{ZQ}=23.7ms (panels: b1, b2) and T_{ZQ}=24.6ms (panels: c1, c2). The simulations depicted in dots correspond to the undamped case. All the simulation parameters are similar to those given in Fig. 2.4 and Table 2.4.

possible. The chemical shifts of the carbons present in the models depicted in Figure 2.3 (panels d, e) correspond to this situation and present an excellent system to verify the validity of our analytic theory (Eqns. 2.27 & 2.28)). In Figure 2.11, polarization transfer from the valine carbonyl carbon to the aliphatic carbons (valine alpha carbon, Leucine beta carbon ($V_{Co} \rightarrow V_{C\alpha}$, 1.50 Å and $V_{Co} \rightarrow L_{C\beta}$, 3.24 Å) is depicted (panel (d1) for N=1, (d2) for N=2).

Although, the model system (see Figure 2.3d) comprises of both a stronger and a weaker coupling, the effects of dipolar truncation are absent in the isolated three-spin system ($I_1 - I_2 - I_3$) (panels, d1 & d2). i.e, the efficiency of transfer from $V_{Co} \rightarrow L_{C\beta}$ (r=3.24 Å) remains uneffected in the presence of the stronger $V_{Co} \rightarrow V_{C\alpha}$ coupling. To further substantiate this aspect, simulations depicting polarization transfer from valine carbonyl carbon to the aliphatic carbons (valine beta carbon, Leucine gamma carbon ($V_{Co} \rightarrow V_{C\beta}$, 2.54 Å and $V_{Co} \rightarrow L_{C\gamma}$, 3.26 Å) are depicted in Figure 2.12, panels e1 (N=1) and e2 (N=2). In contrast to the previous model (Figure 2.3d), the

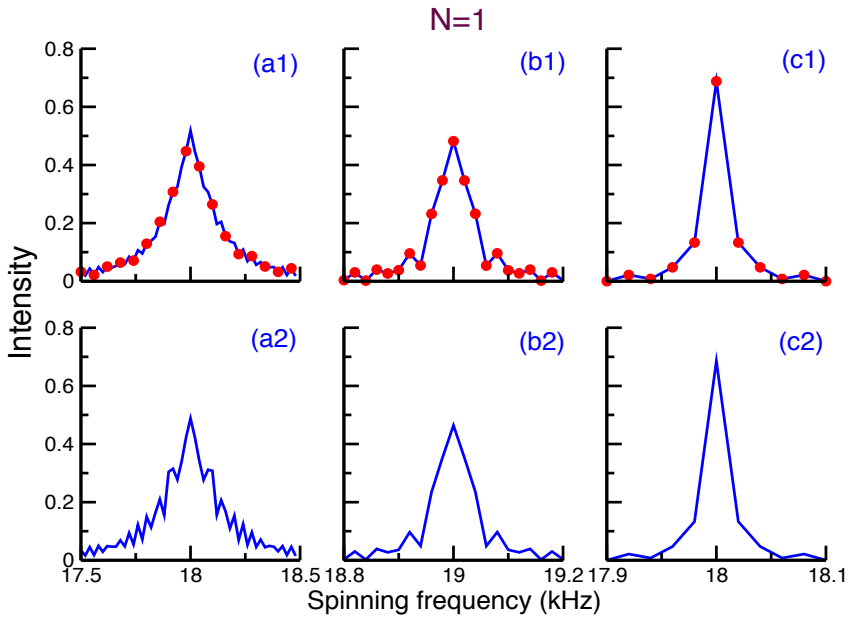

Figure 2.8: The simulations depict the spinning frequency dependent polarization in R^2W experiments (N=1) under constant mixing times. All the simulation parameters are similar to those given in Fig. 2.4 and Table 2.4.

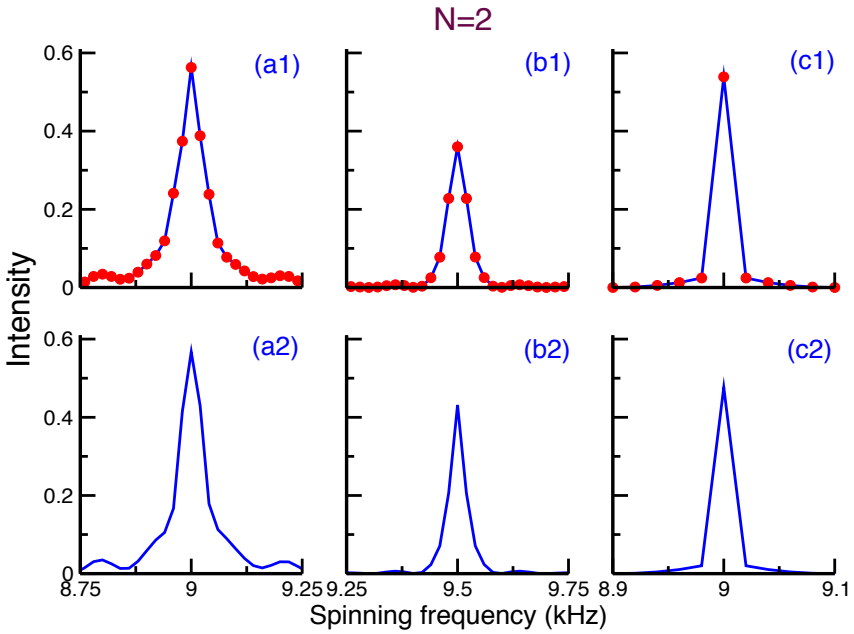

Figure 2.9: The simulations depict the spinning frequency dependent polarization in R^2W experiments (N=2) under constant mixing times. All the simulation parameters are similar to those given in Fig. 2.4 and Table 2.4.

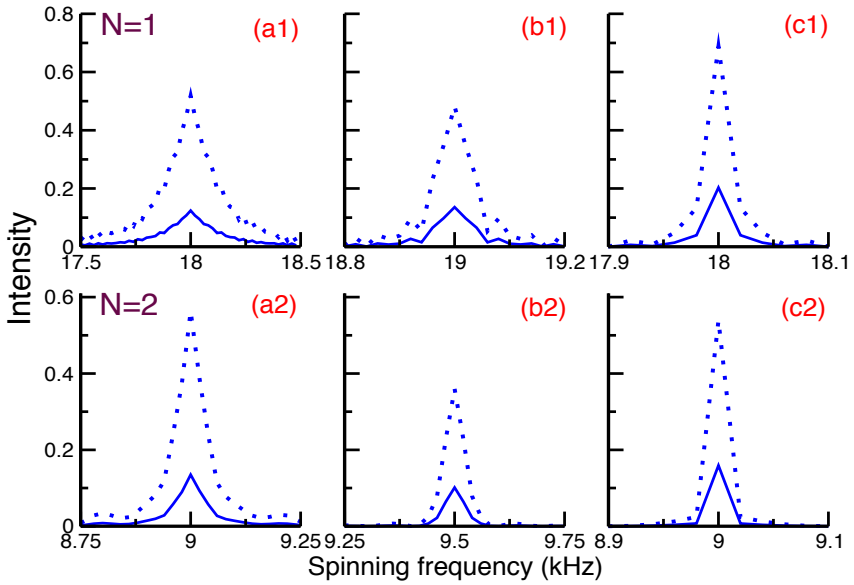

Figure 2.10: The figure depicts the role of phenomenological damping terms (solid line) on the magnetization transfer observed in R^2W experiments (both N=1 & 2). The following damping parameters have been included in the simulations: T_{ZQ}=21ms (panels: a1, a2), T_{ZQ}=23.7ms (panels: b1, b2) and T_{ZQ}=24.6ms (panels: c1, c2). The simulations depicted in dots correspond to the undamped case. All the simulation parameters are similar to those given in Fig. 2.4 and Table 2.4.

resonance conditions in the chosen system (Figure 2.3e) are highly overlapping.

As depicted, the extend of overlap decreases with an increase in the resonance condition. In contrast to other descriptions based on the Liouville space, the analytic simulations based on the reduced density matrix approach are in excellent agreement with the numerical simulations and present an attractive tool for simulating experimental data in band-selective R^2 experiments. Additionally, the simulations emerging from the reduced density matrix approach are computationally less intense and could be employed to fit experimental data with multiple fit parameters that include chemical shift anisotropic parameters (magnitude and orientation), dipolar coupling constants etc. A more detailed description of the spin dynamics in the presence of heteronuclear decoupling will be discussed in chapter-3.

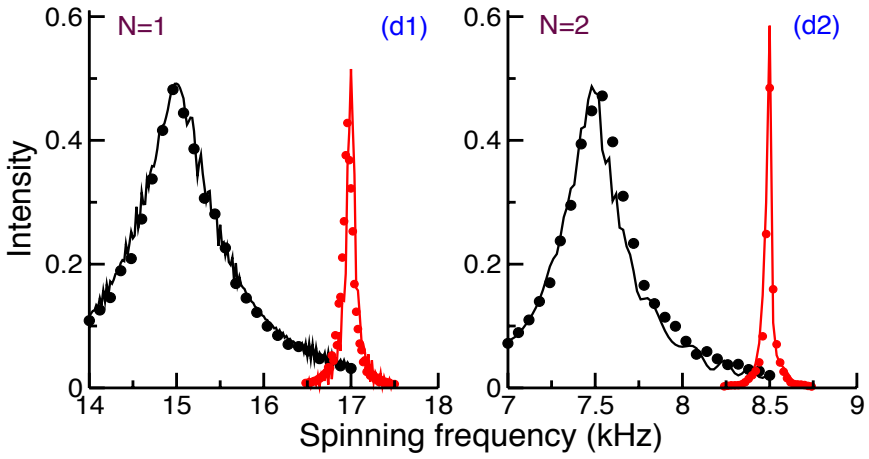

Figure 2.11: The simulations depict the role of neighboring carbons in the polarization transfer observed in R^2 experiments. The polarization transfer from valine carbonyl carbon to valine alpha carbon and leucine beta carbon ($V_{Co} \rightarrow V_{C\alpha}$, 1.50 Å and $V_{Co} \rightarrow L_{C\beta}$, 3.24 Å) as depicted in Figure 2.3(d). The numerical simulations (solid line) are from SPINEVOLUTION[37] and the analytic simulations (circles) are performed using the three-spin RDM expressions (Eqns. 2.27 & 2.28). All the simulation parameters are given in Table 2.4.

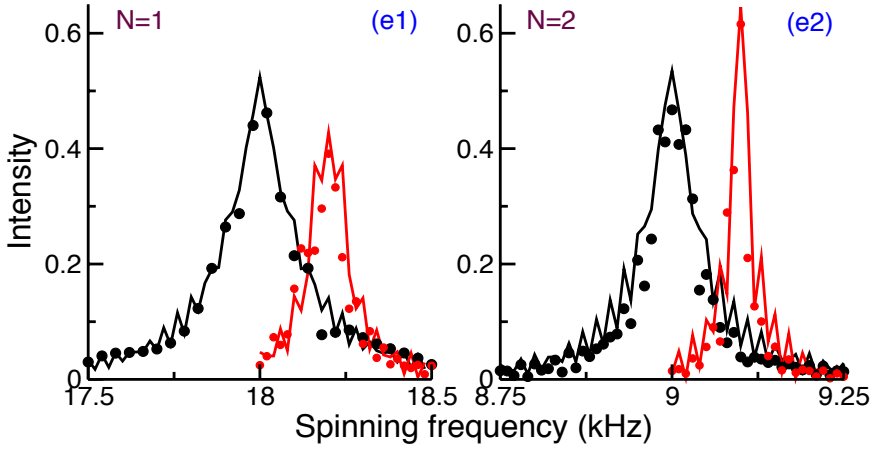

Figure 2.12: The simulations depict the role of neighboring carbons in the polarization transfer observed in R^2 experiments. The polarization transfer from valine carbonyl carbon to valine beta carbon and leucine gamma carbon ($V_{Co} \rightarrow V_{C\beta}$, 2.54 Å and $V_{Co} \rightarrow L_{C\gamma}$, 3.26 Å) as depicted in Figure 2.3(e). The numerical simulations (solid line) are from SPINEVOLUTION[37] and the analytic simulations (circles) are performed using the three-spin RDM expressions (Eqns. 2.27 & 2.28). All the simulation parameters are given in Table 2.4.

2.5 Conclusions

In summary, the reduced density matrix approach presents a simplified yet accurate description of the R^2 phenomenon observed in MAS experiments. In contrast to other existing methods, the analytic expressions resemble to those derived by Rabi and are computationally robust and facilitate simulations involving multiple fit parameters. Although, quantitative description of relaxation has not been attempted, the model presented in this chapter illustrates the shortcomings that arise from the inclusion of phenomenological damping terms. A more detailed description of the R^2 dynamics in the presence of coupling to the surrounding bath of protons will be discussed in the following chapter.

References

[1] E. Andrew, A. Bradbury, R. Eades and V. Wynn, *Phys. Lett.*, 1963, **4**, 99 – 100.

[2] E. Andrew, S. Clough, L. Farnell, T. Gledhill and I. Roberts, *Phys. Lett.*, 1966, **21**, 505 – 506.

[3] E. R. Andrew, A. Bradbury and R. G. Eades, *Nature*, 1958, **182**, 1659–1659.

[4] I. J. Lowe, *Phys. Rev. Lett.*, 1959, **2**, 285–287.

[5] D. Raleigh, G. Harbison, T. Neiss, J. Roberts and R. Griffin, *Chem. Phys. Lett.*, 1987, **138**, 285 – 290.

[6] D. Raleigh, M. Levitt and R. Griffin, *Chem. Phys. Lett.*, 1988, **146**, 71 – 76.

[7] D. P. Raleigh, F. Creuzet, S. K. D. Gupta, M. H. Levitt and R. G. Griffin, *J. Am. Chem. Soc.*, 1989, **111**, 4502–4503.

[8] M. Colombo, B. Meier and R. Ernst, *Chem. Phys. Lett.*, 1988, **146**, 189 – 196.

[9] N. Bloembergen, *Physica*, 1949, **15**, 386 – 426.

[10] A. Grommek, B. H. Meier and M. Ernst, *Chem. Phys. Lett.*, 2006, **427**, 404 – 409.

[11] Z. Gan and D. M. Grant, *Mol. Phys.*, 1989, **67**, 1419–1430.

[12] M. H. Levitt, D. P. Raleigh, F. Creuzet and R. G. Griffin, *J. Chem. Phys.*, 1990, **92**, 6347–6364.

[13] M. Maricq and J. S. Waugh, *J. Chem. Phys.*, 1979, **70**, 3300–3316.

[14] M. M. Maricq, *Phys. Rev. B*, 1982, **25**, 6622–6632.

[15] M. M. Maricq, in *Advances in Magnetic Resonance*, ed. W. S. Warren, Academic Press, 1990, vol. 14, pp. 151 – 182.

[16] A. Schmidt and S. Vega, *J. Chem. Phys.*, 1992, **96**, 2655–2680.

[17] G. Floquet, *Ann. Sci. Ecole Norm. Sup*, 1883, **12**, 47–89.

[18] J. H. Shirley, *Phys. Rev.*, 1965, **138**, 979–987.

[19] D. Zax, G. Goelman, D. Abramovich and S. Vega, in *Advances in Magnetic Resonance*, ed. W. S. Warren, Academic Press, 1990, vol. 14, pp. 219 – 240.

[20] S. Vega, *in Nuclear Magnetic Probes for Molecular Dynamics, edited by R. Tycko*, (Kluwer Academic, Amsterdam, 1994).

[21] S. Vega, *in Encyclopedia of NMR, edited by D. M. Grant and R. Harris*, (Wiley, New York, 1996).

[22] B. C. Filip, X. Filip, D. E. Demco and S. Hafner, *Mol. Phys.*, 1997, **92**, 757–772.

[23] R. Ramachandran and R. G. Griffin, *J. Chem. Phys.*, 2005, **122**, 164502.

[24] M. Leskes, P. Madhu and S. Vega, *Prog. Nucl. Magn. Reson. Spectrosc.*, 2010, **57**, 345 – 380.

[25] I. Scholz, J. D. van Beek and M. Ernst, *Solid State Nuclear Magnetic Resonance*, 2010, **37**, 39 – 59.

[26] R. Ramachandran, J. R. Lewandowski, P. C. A. van der Wel and R. G. Griffin, *J. Chem. Phys.*, 2006, **124**, 214107.

[27] M. K. Pandey and R. Ramachandran, *Mol. Phys.*, 2010, **108**, 619–635.

[28] K. Blum, *Density Matrix Theory and Applications*, Plenum press, New York, 1996.

[29] U. SivaRanjan and R. Ramachandran, *J. Chem. Phys.*, 2014, **140**, 054101.

[30] R. Ramesh and M. S. Krishnan, *J. Chem. Phys.*, 2001, **114**, 5967–5973.

[31] E. Vinogradov, P. K. Madhu and S. Vega, *J. Chem. Phys.*, 2001, **115**, 8983–9000.

[32] D. Papousek and M. R. Aliev, *Molecular Vibrational-Rotational spectra*, Elsevier, Amsterdam, 1982.

[33] J. H. Van Vleck, *Phys. Rev.*, 1929, **33**, 467–506.

[34] I. I. Rabi, *Phys. Rev.*, 1937, **51**, 652–654.

[35] P. J. Carroll, P. L. Stewart and S. J. Opella, *Acta Crystallographica Section C*, 1990, **46**, 243–246.

[36] P. R. Costa, B. Sun and R. G. Griffin, *J. Magn. Reson.*, 2003, **164**, 92 – 103.

[37] M. Veshtort and R. G. Griffin, *Journal of Magnetic Resonance*, 2006, **178**, 248 – 282.

Chapter 3

Description of multi-spin effects and the role of heteronuclear decoupling in R^2 experiments

3.1 Background

To extend the utility and reliability of R^2 experiments in structure determination, quantifying experimental data remains essential. Since the number of $^{13}C - {}^{13}C$ distance constraints estimated from R^2 experiments are limited by the lack of sufficient resolution, the precision of the measured $^{13}C - {}^{13}C$ distances play an important role in the overall structure refinement. In a real system, polarization transfer between ^{13}C nuclei under R^2 conditions takes place in the presence of abundant protons. To minimize the role of protons in the magnetization exchange, strong decoupling fields are applied on the proton channel during the R^2 dipolar mixing period.[1–4] Although such methods improve the efficiency of polarization transfer under R^2 conditions, the effects of the residual heteronuclear dipolar interactions ($^{13}C - {}^{1}H$) can not be eliminated altogether. Hence, the inclusion of a phenomenological damping term (T_{ZQ}^{-1}) in the R^2 simulations within an isolated two-spin framework was proposed as a solution. In the analytic model proposed by Levitt et al.[5], the spin dynamics under R^2 conditions is described through a vector model defined in the ZQ subspace. In the ZQ subspace, the spin dynamics is described within an isolated spin-pair framework through components of angular momentum vector defined along the x, y, z axis in

the ZQ subspace. The recoupled dipolar Hamiltonian depicts a vector in the transverse plane while the longitudinal difference polarization is defined along the z-axis. Analogous to the Bloch model of relaxation, a phenomenological damping term in the ZQ subspace is included to compensate for both experimental imperfections and inaccuracies in theoretical descriptions.

In the strong coupling regime, the exchange dynamics is predominantly influenced by the reintroduced dipolar interactions. Under near idealized decoupling conditions, the multi-spin effects seem less influential. On the contrary, in the weak-coupling regime, the efficiency of transfer is inherently slow and the effects of relaxation come into play. Since important measurements constraining the orientation of side chains with respect to backbone are contained in the long-range contacts, extreme care needs to be exercised in the interpretation of experimental data in the weaker coupling regime.[1–4] To this end, Costa et al.[6] proposed constant mixing time experiments to minimize the effects of relaxation. Although, constant mixing time experiments seem to be an attractive solution, the effects of multi-spin interactions cannot be eliminated altogether. Hence, the validity of phenomenological damping models employed in the existing treatments needs to be revisited.

3.2 Definition of the problem

To settle this issue and present a comprehensive description of the exchange dynamics under R^2 conditions, a model system (comprising of N-protons in the form of $I_1 - I_2 - S_N$ and $I_1 - I_2 - I_3 - S_N$) was employed in the present study. Employing the reduced density matrix approach, the role of different heteronuclear decoupling schemes[7–26] (during R^2 mixing period) is described analytically through effective Hamiltonians.

3.3 Theory

3.3.1 Effect of CW heteronuclear decoupling

A. $I_1 - I_2 - S_N$ system

To elucidate the role of protons in the magnetization exchange between ^{13}C nuclei in R^2 experiments, we begin our discussion with a model system ($I_1 - I_2 - S_N$)

comprising of two carbons (denoted by I) coupled to N-protons (denoted by S). Figure 3.1 depicts the CW[7–9] field employed to decouple the heteronuclear dipolar ($^{13}C - {}^{1}H$) interactions during R^2 mixing time.

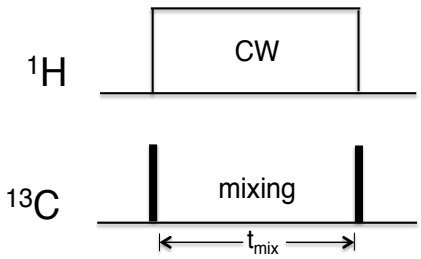

Figure 3.1: Schematic diagram depicting the CW decoupling during the R^2 mixing time.

The time-dependent MAS Hamiltonian for such a system is represented by,

$$H(t) = H^{C}_{System}(t) + H^{C-H}_{System-Bath}(t) + H^{H}_{Bath}(t) + H^{H}_{RF} \tag{3.1}$$

In the above representation, $H^{C}_{System}(t)$ denotes the Hamiltonian of the system of interest (^{13}C) comprising of the chemical shift and dipolar interactions.

$$\begin{aligned} H^{C}_{System}(t) = &\sum_{m=-2}^{2}\sum_{i=1}^{2}\omega^{(m)}_{I_i}e^{im\omega_r t}I_{iz} + \\ &\sum_{m=-2;m\neq 0}^{2}\omega^{(m)}_{I_1I_2}e^{im\omega_r t}\left(2I_{1z}I_{2z} - \tfrac{1}{2}(I^{+}_{1}I^{-}_{2} + I^{-}_{1}I^{+}_{2})\right) \end{aligned} \tag{3.2}$$

In a similar vein, $H^{H}_{Bath}(t)$ denotes the interactions present among the surrounding bath of protons.

$$\begin{aligned} H^{H}_{Bath}(t) = &\sum_{m=-2}^{2}\sum_{j=1}^{N}\omega^{(m)}_{S_j}e^{im\omega_r t}S_{jz} + \\ &\sum_{m=-2;m\neq 0}^{2}\sum_{j,k=1;j<k}^{N}\omega^{(m)}_{S_jS_k}e^{im\omega_r t}\left(2S_{jz}S_{kz} - (S_{jx}S_{kx} + S_{jy}S_{ky})\right) \end{aligned} \tag{3.3}$$

The coupling of the system with the surroundings is represented by $H^{C-H}_{System-Bath}(t)$ and comprises of the heteronuclear dipolar interactions.

$$H^{C-H}_{System-Bath}(t) = \sum_{m=-2;m\neq 0}^{2}\sum_{i=1}^{2}\sum_{j=1}^{N}\omega^{(m)}_{I_iS_j}e^{im\omega_r t}2I_{iz}S_{jz} \tag{3.4}$$

To improve the efficiency of magnetization exchange between the ^{13}C nuclei, intense RF fields (also referred to as decoupling fields) are applied along the proton channel

to minimize the interaction between the carbons and the surrounding proton bath. This action is represented quantum mechanically by

$$H_{RF}^{H} = \sum_{j=1}^{N} \omega_{rf} S_{jx} \tag{3.5}$$

To deduce the R^2 matching conditions and describe the effects of RF irradiation, the Hamiltonian in the rotating frame (Eq. (3.1)) is transformed into an interaction frame defined by the transformation operators, $U_1 = \sum_{j=1}^{N} e^{i\frac{\pi}{2}S_{jy}}$ and $U_2 = e^{in\omega_r t I_{1z}} e^{-in\omega_r t I_{2z}}$ as represented below.

$$\tilde{H}(t) = U_2 U_1 H(t) U_1^{-1} U_2^{-1} \tag{3.6}$$

$$\tilde{H}(t) = \tilde{H}_{System}^{C}(t) + \tilde{H}_{System-Bath}^{C-H}(t) + \tilde{H}_{Bath}^{H}(t) + \tilde{H}_{RF}^{H} \tag{3.7}$$

A detailed representation of the Hamiltonian in the interaction frame is given below.

$$\begin{aligned}\tilde{H}_{System}^{C}(t) =& (\omega_{I_1}^{(0)} - n\omega_r) I_{1z} + (\omega_{I_2}^{(0)} + n\omega_r) I_{2z} + \sum_{m=-2;m\neq 0}^{2} \sum_{i=1}^{2} \omega_{I_i}^{(m)} e^{im\omega_r t} I_{iz} + \\ & \sum_{m=-2;m\neq 0}^{2} \omega_{I_1 I_2}^{(m)} \left[2I_{1z} I_{2z} e^{im\omega_r t} - \tfrac{1}{2} \left(I_1^{+} I_2^{-} e^{i(m+2n)\omega_r t} + I_1^{-} I_2^{+} e^{i(m-2n)\omega_r t} \right) \right]\end{aligned} \tag{3.8}$$

$$\tilde{H}_{System-Bath}^{C-H}(t) = -\sum_{m=-2;m\neq 0}^{2} \sum_{i=1}^{2} \sum_{j=1}^{N} \omega_{I_i S_j}^{(m)} e^{im\omega_r t} 2I_{iz} S_{jx} \tag{3.9}$$

$$\begin{aligned}\tilde{H}_{Bath}^{H}(t) =& -\sum_{m=-2}^{2} \sum_{j=1}^{N} \omega_{S_j}^{(m)} e^{im\omega_r t} S_{jx} + \\ & \sum_{m=-2;m\neq 0}^{2} \sum_{j,k=1;j<k}^{N} \omega_{S_j S_k}^{(m)} e^{im\omega_r t} \left(2S_{jx} S_{kx} - (S_{jz} S_{kz} + S_{jy} S_{ky}) \right)\end{aligned} \tag{3.10}$$

$$\tilde{H}_{RF}^{H} = \sum_{j=1}^{N} \omega_{rf} S_{jz} \tag{3.11}$$

As described in chapter-2, to minimize the complexity arising from time-dependent Hamiltonians, Floquet theory is employed to transform the Hamiltonian (Eq. 3.7) into a time-independent Hamiltonian as defined below.

$$H_F = H_0 + H_1 = H_0 + (H_{1,d} + H_{1,od}) \tag{3.12}$$

In the above Floquet Hamiltonian, $H_{1,d}$ and $H_{1,od}$ represent the diagonal (diagonal in the Fourier dimension) and off-diagonal contributions and have the following definitions.

$$H_0 = \omega_r I_F + \sum_{j=1}^{N} \omega_{rf} [S_{jz}]_0 \tag{3.13}$$

$$H_{1,d} = (\omega_{I_1}^{(0)} - n\omega_r)[I_{1z}]_0 + (\omega_{I_2}^{(0)} + n\omega_r)[I_{2z}]_0 + G_{I_1I_2,PM}^{(0)}\left[I_1^+ I_2^-\right]_0 + G_{I_1I_2,MP}^{(0)}\left[I_1^- I_2^+\right]_0 \tag{3.14}$$

$$H_{1,od}^{C-C} = \sum_{m=-2,m\neq 0}^{2}\sum_{i=1}^{2} G_{I_i}^{(m)}[I_{iz}]_m + \sum_{m=-2,m\neq 0}^{2} G_{I_1I_2}^{(m)}[I_{1z}I_{2z}]_m + \sum_{m=-2,m\neq 0}^{2}\left(G_{I_1I_2,PM}^{(m+2n)}\left[I_1^+ I_2^-\right]_{m+2n} + G_{I_1I_2,MP}^{(m-2n)}\left[I_1^- I_2^+\right]_{m-2n}\right) \tag{3.15}$$

$$H_{1,od}^{C-H} = \sum_{i=1}^{2}\sum_{j=1}^{N}\sum_{m=-2,m\neq 0}^{2}\left(G_{I_iS_j,ZP}^{(m)}\left[I_{iz}S_j^+\right]_m + G_{I_iS_j,ZM}^{(m)}\left[I_{iz}S_j^-\right]_m\right) \tag{3.16}$$

$$\begin{aligned} H_{1,od}^{H-H} = &\sum_{j=1}^{N}\sum_{m=-2}^{2}\left(G_{S_j,P}^{(m)}\left[S_j^+\right]_m + G_{S_j,M}^{(m)}\left[S_j^-\right]_m\right) + \\ &\sum_{j,k=1,j<k;}^{N}\sum_{m=-2,m\neq 0}^{2}\left(G_{S_jS_k,PP}^{(m)}\left[S_j^+ S_k^+\right]_m + G_{S_jS_k,MM}^{(m)}\left[S_j^- S_k^-\right]_m\right) + \\ &\sum_{j,k=1,j<k;}^{N}\sum_{m=-2,m\neq 0}^{2}\left(G_{S_jS_k}^{(m)}[S_{jz}S_{kz}]_m + G_{S_jS_k,PM}^{(m)}\left[S_j^+ S_k^-\right]_m + G_{S_jS_k,MP}^{(m)}\left[S_j^- S_k^+\right]_m\right) \end{aligned} \tag{3.17}$$

$$\begin{aligned} S_1 = &i\sum_{m=-2,m\neq 0}^{2}\sum_{i=1}^{2} C_{I_i}^{(m)}[I_{iz}]_m + i\sum_{m=-2,m\neq 0}^{2} C_{I_1I_2}^{(m)}[I_{1z}I_{2z}]_m + \\ &i\sum_{m=-2,m\neq 0}^{2}\left(C_{I_1I_2,PM}^{(m+2n)}\left[I_1^+ I_2^-\right]_{m+2n} + C_{I_1I_2,MP}^{(m-2n)}\left[I_1^- I_2^+\right]_{m-2n}\right) + \\ &i\sum_{i=1}^{2}\sum_{j=1}^{N}\sum_{m=-2,m\neq 0}^{2}\left(C_{I_iS_j,ZP}^{(m)}\left[I_{iz}S_j^+\right]_m + C_{I_iS_j,ZM}^{(m)}\left[I_{iz}S_j^-\right]_m\right) + \\ &i\sum_{j=1}^{N}\sum_{m=-2}^{2}\left(C_{S_j,P}^{(m)}\left[S_j^+\right]_m + C_{S_j,M}^{(m)}\left[S_j^-\right]_m\right) + \\ &i\sum_{j,k=1,j<k;}^{N}\sum_{m=-2,m\neq 0}^{2}\left(C_{S_jS_k,PP}^{(m)}\left[S_j^+ S_k^+\right]_m + C_{S_jS_k,MM}^{(m)}\left[S_j^- S_k^-\right]_m\right) + \\ &i\sum_{j,k=1,j<k;}^{N}\sum_{m=-2,m\neq 0}^{2}\left(C_{S_jS_k}^{(m)}[S_{jz}S_{kz}]_m + C_{S_jS_k,PM}^{(m)}\left[S_j^+ S_k^-\right]_m + C_{S_jS_k,MP}^{(m)}\left[S_j^- S_k^+\right]_m\right) \end{aligned} \tag{3.18}$$

Employing the contact transformation procedure, the above Floquet Hamiltonian (Eq. 3.12) is diagonalised by a single unitary transformation defined by the transformation function, S_1. The 'G' and 'C' coefficients employed in the Floquet Hamiltonian and the transformation function, S_1 are tabulated in Table 3.1. The

remaining coefficients presented in Eqs. (3.12) & (3.18) are similar to those defined in chapter-2 (refer to Tables 2.1 & 2.2).

G-coefficients	C-coefficients
$G^{(m)}_{S_j,P} = -\frac{1}{2}\omega^{(m)}_{S_j}$	$C^{(m)}_{S_j,P} = \frac{G^{(m)}_{S_j,P}}{m\omega_r+\omega_{rf}}$
$G^{(m)}_{S_j,M} = -\frac{1}{2}\omega^{(m)}_{S_j}$	$C^{(m)}_{S_j,M} = \frac{G^{(m)}_{S_j,M}}{m\omega_r-\omega_{rf}}$
$G^{(m)}_{I_iS_j,ZP} = -\omega^{(m)}_{I_iS_j}$	$C^{(m)}_{I_iS_j,ZP} = \frac{G^{(m)}_{I_iS_j,ZP}}{m\omega_r+\omega_{rf}}$
$G^{(m)}_{I_iS_j,ZM} = -\omega^{(m)}_{I_iS_j}$	$C^{(m)}_{I_iS_j,ZM} = \frac{G^{(m)}_{I_iS_j,ZM}}{m\omega_r-\omega_{rf}}$
$G^{(m)}_{S_jS_k,PP} = \frac{3}{4}\omega^{(m)}_{S_jS_k}$	$C^{(m)}_{S_jS_k,PP} = \frac{G^{(m)}_{S_jS_k,PP}}{m\omega_r+2\omega_{rf}}$
$G^{(m)}_{S_jS_k,MM} = \frac{3}{4}\omega^{(m)}_{S_jS_k}$	$C^{(m)}_{S_jS_k,MM} = \frac{G^{(m)}_{S_jS_k,MM}}{m\omega_r-2\omega_{rf}}$
$G^{(m)}_{S_jS_k,PM} = \frac{1}{4}\omega^{(m)}_{S_jS_k}$	$C^{(m)}_{S_jS_k,PM} = \frac{G^{(m)}_{S_jS_k,PM}}{m\omega_r}$
$G^{(m)}_{S_jS_k,MP} = \frac{1}{4}\omega^{(m)}_{S_jS_k}$	$C^{(m)}_{S_jS_k,MP} = \frac{G^{(m)}_{S_jS_k,MP}}{m\omega_r}$
$G^{(m)}_{S_jS_k} = -\omega^{(m)}_{S_jS_k}$	$C^{(m)}_{S_jS_k} = \frac{G^{(m)}_{S_jS_k}}{m\omega_r}$

Table 3.1: The table depicts the 'G' and C-coefficients involved in the Floquet Hamiltonian (Eq. 3.12) and the transformation function, S_1 (Eq. 3.18).

Coefficients	**First - order**	**Second - order**
$D_{I_iS_j}$	0	$\underbrace{\frac{1}{2}\left(C^{(m)}_{S_j,P}G^{(-m)}_{I_iS_j,ZM} - C^{(m)}_{I_iS_j,ZM}G^{(-m)}_{S_j,P}\right) - \frac{1}{2}\left(C^{(m)}_{S_j,M}G^{(-m)}_{I_iS_j,ZP} - C^{(m)}_{I_iS_j,ZP}G^{(-m)}_{S_j,M}\right)}_{\text{CSA}(^1H)\times\text{Dipolar}(^{13}C-^1H)}$

Table 3.2: This table depicts the heteronuclear dipolar coefficients ($D_{I_iS_j}$) involved in the effective Hamiltonians (Eqs. 3.19 & 3.44). See Table 3.1 for all the 'G' and 'C' coefficients with the corresponding Fourier indices (m) in the above table.

Following the procedure described in the previous chapter, the effective Hamilto-

nian for the model $(I_1 - I_2 - S_N)$ system is derived and represented below.

$$H_{eff} = \sum_{i=1}^{2} A_{I_i}[I_{iz}]_0 + \sum_{j=1}^{N} \omega_{rf}[S_{jz}]_0 + \left[D_{I_1I_2,PM}\left[I_1^+ I_2^-\right]_0 + D_{I_1I_2,MP}\left[I_1^- I_2^+\right]_0\right] + \sum_{i=1}^{2}\sum_{j=1}^{N} D_{I_iS_j}[I_{iz}S_{jz}]_0 \tag{3.19}$$

The coefficients involved in the above effective Hamiltonian are tabulated in Tables 2.3 & 3.2. In contrast to the description involving only carbons (^{13}C), the effective Hamiltonian for the model systems involving protons (^1H), comprises of second order contributions resulting from cross-terms between the heteronuclear dipolar interactions (^{13}C-^1H) and the CSA of the protons. The role of these cross-terms will be discussed in the following sections.

To elucidate the role of protons in the exchange dynamics and demonstrate the utility of the reduced density matrix approach, we begin our discussion with a model three-spin system comprising of two carbons and a single proton $(I_1 - I_2 - S)$.

Following the procedure described in the previous chapter, the reduced density operator for I_1 ($\rho(I_1, t)$) is derived systematically by taking the partial trace over the other spin variables (I_2 and S) present in the combined system.

$$\rho(I_1,t) = \begin{bmatrix} \sum_{i=1}^{4} \rho_{\alpha_1\Phi_i^{(2)},\alpha_1\Phi_i^{(2)}}(t) & \sum_{i=1}^{4} \rho_{\alpha_1\Phi_i^{(2)},\beta_1\Phi_i^{(2)}}(t) \\ \sum_{i=1}^{4} \rho_{\beta_1\Phi_i^{(2)},\alpha_1\Phi_i^{(2)}}(t) & \sum_{i=1}^{4} \rho_{\beta_1\Phi_i^{(2)},\beta_1\Phi_i^{(2)}}(t) \end{bmatrix} \tag{3.20}$$

where $\rho_{\alpha_1\Phi_i^{(2)},\alpha_1\Phi_i^{(2)}}(t)$ represents the matrix element $\left\langle \alpha_1\Phi_i^{(2)} \right| \rho(t) \left| \alpha_1\Phi_i^{(2)} \right\rangle$ with $\Phi_i^{(2)}$ representing the spin state of the remaining spin system, $I_2\&S$ (say $\Phi_1^{(2)} = |\alpha_2\alpha_3\rangle$, $\Phi_2^{(2)} = |\alpha_2\beta_3\rangle$, $\Phi_3^{(2)} = |\beta_2\alpha_3\rangle$ and $\Phi_4^{(2)} = |\beta_2\beta_3\rangle$) with the superscript denoting the total number of spins other than the one observed. Accordingly, the polarization transfer from spin I_1 to I_2 (i.e. $\rho(0) = I_{1z}$) in the presence of a single proton is calculated.

$$\rho(I_1,t) = \begin{bmatrix} 2 - |D_{I_1I_2}|^2 \sum_{i=1}^{2} \frac{\sin^2 x_i t}{{x_i}^2} & 0 \\ 0 & -\left(2 - |D_{I_1I_2}|^2 \sum_{i=1}^{2} \frac{\sin^2 x_i t}{{x_i}^2}\right) \end{bmatrix} \tag{3.21}$$

In a similar vein, the reduced density matrix for I_2 is derived by taking the partial trace over the other spin variables (I_1 and S).

$$\rho(I_2,t) = \begin{bmatrix} \sum_{i=1}^{4} \rho_{\Phi_i^{(2)}\alpha_2,\Phi_i^{(2)}\alpha_2}(t) & \sum_{i=1}^{4} \rho_{\Phi_i^{(2)}\alpha_2,\Phi_i^{(2)}\beta_2}(t) \\ \sum_{i=1}^{4} \rho_{\Phi_i^{(2)}\beta_2,\Phi_i^{(2)}\alpha_2}(t) & \sum_{i=1}^{4} \rho_{\Phi_i^{(2)}\beta_2,\Phi_i^{(2)}\beta_2}(t) \end{bmatrix} \tag{3.22}$$

$$\rho(I_2,t) = \begin{bmatrix} |D_{I_1I_2}|^2 \sum_{i=1}^{2} \frac{\sin^2 x_i t}{{x_i}^2} & 0 \\ 0 & -|D_{I_1I_2}|^2 \sum_{i=1}^{2} \frac{\sin^2 x_i t}{{x_i}^2} \end{bmatrix} \tag{3.23}$$

Subsequently, the polarization transfer from spin I_1 to I_2 in the presence of a single proton under R^2 conditions is calculated by evaluating $\langle I_z \rangle$ as shown below (normalization factor, $(2)^{K-2}$ where K=number of spins in the system is included).

$$\langle O_I(t) \rangle = Tr[\rho(I,t).O_I] \tag{3.24}$$

$$\langle I_{1z}(t) \rangle = 1 - \frac{|D_{I_1I_2}|^2}{2} \sum_{i=1}^{2} \frac{\sin^2 x_i t}{{x_i}^2} \tag{3.25}$$

$$\langle I_{2z}(t) \rangle = \frac{|D_{I_1I_2}|^2}{2} \sum_{i=1}^{2} \frac{\sin^2 x_i t}{{x_i}^2} \tag{3.26}$$

In contrast to an isolated spin pair, additional oscillatory terms due to the residual $^{13}C - {}^1H$ dipolar interactions are present in the 'x' coefficients.

$$x_1 = \sqrt{|D_{I_1I_2}|^2 + \left(\frac{2(A_{I_1} - A_{I_2}) + (D_{I_1S_1} - D_{I_2S_1})}{4}\right)^2} \tag{3.27}$$

$$x_2 = \sqrt{|D_{I_1I_2}|^2 + \left(\frac{2(A_{I_1} - A_{I_2}) - (D_{I_1S_1} - D_{I_2S_1})}{4}\right)^2} \tag{3.28}$$

Following the above approach, the reduced density matrices for the spins I_1, I_2 surrounded by 'N' protons in the model spin system, $I_1 - I_2 - S_N$ is derived as represented below.

$$\rho(I_1,t) = \begin{bmatrix} \sum_{i=1}^{2^\lambda} \rho_{\alpha_1\Phi_i^{(\lambda)},\alpha_1\Phi_i^{(\lambda)}}(t) & \sum_{i=1}^{2^\lambda} \rho_{\alpha_1\Phi_i^{(\lambda)},\beta_1\Phi_i^{(\lambda)}}(t) \\ \sum_{i=1}^{2^\lambda} \rho_{\beta_1\Phi_i^{(\lambda)},\alpha_1\Phi_i^{(\lambda)}}(t) & \sum_{i=1}^{2^\lambda} \rho_{\beta_1\Phi_i^{(\lambda)},\beta_1\Phi_i^{(\lambda)}}(t) \end{bmatrix} \tag{3.29}$$

$$\rho(I_2,t) = \begin{bmatrix} \sum_{i=1}^{2^\lambda} \rho_{\Phi_i^{(\lambda)}\alpha_2,\Phi_i^{(\lambda)}\alpha_2}(t) & \sum_{i=1}^{2^\lambda} \rho_{\Phi_i^{(\lambda)}\alpha_2,\Phi_i^{(\lambda)}\beta_2}(t) \\ \sum_{i=1}^{2^\lambda} \rho_{\Phi_i^{(\lambda)}\beta_2,\Phi_i^{(\lambda)}\alpha_2}(t) & \sum_{i=1}^{2^\lambda} \rho_{\Phi_i^{(\lambda)}\beta_2,\Phi_i^{(\lambda)}\beta_2}(t) \end{bmatrix} \tag{3.30}$$

In the above equation, the superscript 'λ' denotes the total number of spins other than the one observed. Employing the effective Hamiltonian (Eq. 3.19), the reduced density matrices corresponding to I_1 and I_2 are evaluated.

$$\rho(I_1,t) = \begin{bmatrix} (2)^{K-2} - |D_{I_1I_2}|^2 \sum_{i=1}^{2^N} \frac{\sin^2 x_i t}{{x_i}^2} & 0 \\ 0 & -\left((2)^{K-2} - |D_{I_1I_2}|^2 \sum_{i=1}^{2^N} \frac{\sin^2 x_i t}{{x_i}^2}\right) \end{bmatrix} \tag{3.31}$$

$$\rho(I_2,t) = \begin{bmatrix} |D_{I_1I_2}|^2 \sum_{i=1}^{2^N} \frac{\sin^2 x_i t}{{x_i}^2} & 0 \\ 0 & -|D_{I_1I_2}|^2 \sum_{i=1}^{2^N} \frac{\sin^2 x_i t}{{x_i}^2} \end{bmatrix} \tag{3.32}$$

Subsequently, the polarization transfer from I_1 to I_2 in the presence of coupling to neighboring proton bath is calculated.

$$\langle I_{1z}(t)\rangle = 1 - \frac{|D_{I_1I_2}|^2}{(2)^{K-2}} \sum_{i=1}^{2^N} \frac{\sin^2 x_i t}{{x_i}^2} \tag{3.33}$$

$$\langle I_{2z}(t)\rangle = \frac{|D_{I_1I_2}|^2}{(2)^{K-2}} \sum_{i=1}^{2^N} \frac{\sin^2 x_i t}{{x_i}^2} \tag{3.34}$$

As described above (see Eqs. 3.33 & 3.34), the analytic expressions for a system coupled to N-protons comprises of 2^N 'x_i' coefficients.

$$x_i = \sqrt{|D_{I_1I_2}|^2 + \left(\frac{2(A_{I_1} - A_{I_2}) + y_i}{4}\right)^2} \tag{3.35}$$

For a given 'x_i', the corresponding 'y_i' coefficients are sequentially deduced from the scheme depicted in Fig. 3.2.

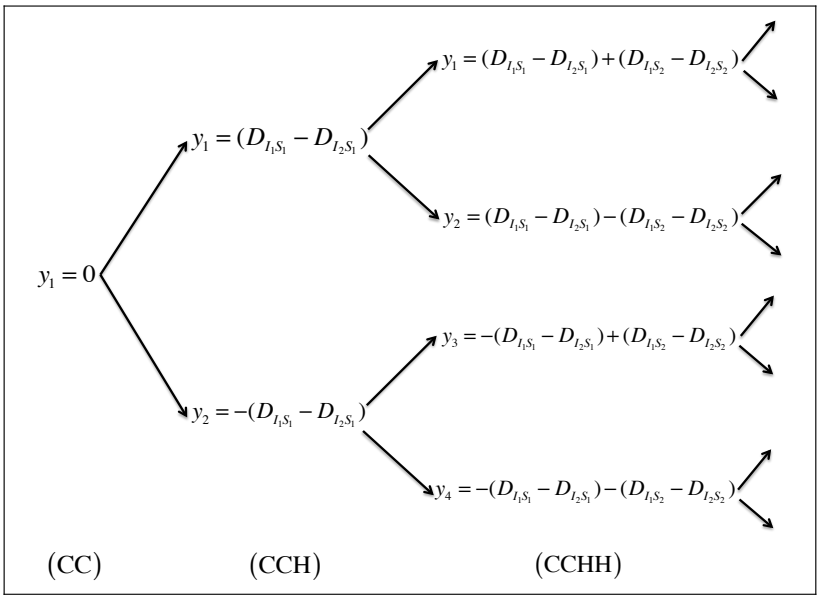

Figure 3.2: The figure depicts the flow chart for deriving the 'y' coefficients described in Eq. (3.35).

The analytic expressions depicted in Eqs. 3.33 & 3.34 could be employed to fit experimental exchange curves employing multiple fit parameters such as $^{13}C - {}^{13}C$ distance, the orientation, magnitude of CSA tensors (both carbons and protons) and $^{13}C - {}^{1}H$ distances.

B. $I_1 - I_2 - I_3 - S_N$ system

To describe the multi-spin contributions arising from neighboring spins, a model system comprising of three spins $I_1-I_2-I_3$ (all ^{13}C nuclei) coupled to 'N' protons (^1H) was employed in continuation to the ideal three-spin system ($I_1-I_2-I_3$) discussed in chapter-2. The model serves as a prototype for describing band-selective polarization transfer from the carbonyl carbons (I_1) to the aliphatic carbons (I_2, I_3) found in a typical amino acid /polypeptide sequence. Accordingly, the time-dependent MAS Hamiltonian for the model system is represented by,

$$H(t) = H^C_{System}(t) + H^{C-H}_{System-Bath}(t) + H^H_{Bath}(t) + H^H_{RF} \tag{3.36}$$

$$H^C_{System}(t) = = \sum_{i=1}^{3} \left(\omega_i^{(0)} + \omega_i(t)\right) I_{iz} + \sum_{i,j=1;i<j}^{3} \omega_{ij}(t) \left(2I_{iz}I_{jz} - \frac{1}{2}(I_i^+ I_j^- + I_i^- I_j^+)\right) \tag{3.37}$$

$$H^H_{Bath}(t) = \sum_{m=-2}^{2} \sum_{j=1}^{N} \omega^{(m)}_{S_j} e^{im\omega_r t} S_{jz} + \sum_{m=-2;m\neq 0}^{2} \sum_{j,k=1;j<k}^{N} \omega^{(m)}_{S_jS_k} e^{im\omega_r t} \left(2S_{jz}S_{kz} - (S_{jx}S_{kx} + S_{jy}S_{ky})\right) \tag{3.38}$$

$$H^{C-H}_{System-Bath}(t) = \sum_{m=-2;m\neq 0}^{2} \sum_{i=1}^{3} \sum_{j=1}^{N} \omega^{(m)}_{I_iS_j} e^{im\omega_r t} 2I_{iz}S_{jz} \tag{3.39}$$

$$H^H_{RF} = \sum_{j=1}^{N} \omega_{rf} S_{jx} \tag{3.40}$$

Analogous to the description employed in the model system ($I_1 - I_2 - S_N$), the Hamiltonian in the rotating frame (Eq. 3.36) is transformed into an interaction frame defined by the transformation operators, $U_1 = \sum_{j=1}^{N} e^{i\frac{\pi}{2}S_{jy}}$ and $U_2 = e^{in\omega_r t I_{1z}} e^{-in\omega_r t I_{2z}} e^{-in\omega_r t I_{3z}}$ and $U_3 = \sum_{j=1}^{N} e^{i\omega_{rf} t S_{jy}}$.

$$\tilde{H}(t) = U_3U_2U_1H(t)U_1^{-1}U_2^{-1}U_3^{-1} \tag{3.41}$$

$$\tilde{H}(t) = \tilde{H}^C_{System}(t) + \tilde{H}^{C-H}_{System-Bath}(t) + \tilde{H}^H_{Bath}(t) \tag{3.42}$$

A detailed representation of the Hamiltonian in the interaction frame is given below.

$$\begin{aligned}\tilde{H}(t) =&(\omega_1^{(0)} - n\omega_r)I_{1z} + (\omega_2^{(0)} + n\omega_r)I_{2z} + (\omega_3^{(0)} + n\omega_r)I_{3z} + \sum_{i=1}^{3}\omega_i^{(m)}e^{im\omega_r t}I_{iz} \\ &\sum_{m=-2,m\neq 0}^{2}\omega_{12}^{(m)}\left[2I_{1z}I_{2z}e^{im\omega_r t} - \frac{1}{2}\left(I_1^+I_2^-e^{i(m+2n)\omega_r t} + I_1^-I_2^+e^{i(m-2n)\omega_r t}\right)\right] + \\ &\sum_{m=-2,m\neq 0}^{2}\omega_{13}^{(m)}\left[2I_{1z}I_{3z}e^{im\omega_r t} - \frac{1}{2}\left(I_1^+I_3^-e^{i(m+2n)\omega_r t} + I_1^-I_3^+e^{i(m-2n)\omega_r t}\right)\right] + \\ &\sum_{m=-2,m\neq 0}^{2}\omega_{23}^{(m)}e^{im\omega_r t}\left[2I_{2z}I_{3z} - \frac{1}{2}\left(I_2^+I_3^- + I_2^-I_3^+\right)\right] \end{aligned} \tag{3.43}$$

The other spin interactions in the interaction frame remain identical to those depicted in the previous section (refer to Eqs. 3.9, 3.10 & 3.11). Following the standard procedure (Floquet theory and the contact transformation methods), the effective Hamiltonian for the model system was derived and are represented below.

$$\begin{aligned}H_{eff} =&\sum_{i=1}^{2}A_{I_i}[I_{iz}]_0 + \sum_{j=1}^{N}\omega_{rf}[S_{jz}]_0 + \sum_{j=2}^{3}\left[D_{I_1I_j,PM}\left[I_1^+I_2^-\right]_0 + D_{I_1I_j,MP}\left[I_1^-I_2^+\right]_0\right] + \\ &\sum_{i=1}^{2}\sum_{j=1}^{N}D_{I_iS_j}[I_{iz}S_{jz}]_0 \end{aligned} \tag{3.44}$$

The coefficients involved in the above effective Hamiltonian are tabulated in Tables 2.3 & 3.2.

Analogous to the description presented in the previous section, the polarization exchange in the model system ($I_1 - I_2 - I_3 - S_N$) is described using the following expressions.

$$\langle I_{1z}(t)\rangle = 1 - |D_{I_1I_2}|^2\sum_{i=1}^{2^N}\frac{\sin^2 x_{i,(I_1I_2)}t}{x_{i,(I_1I_2)}^2} - |D_{I_1I_3}|^2\sum_{i=1}^{2^N}\frac{\sin^2 x_{i,(I_1I_3)}t}{x_{i,(I_1I_3)}^2} \tag{3.45}$$

$$\langle I_{2z}(t)\rangle = |D_{I_1I_2}|^2\sum_{i=1}^{2^N}\frac{\sin^2 x_{i,(I_1I_2)}t}{x_{i,(I_1I_2)}^2} \tag{3.46}$$

$$\langle I_{3z}(t)\rangle = |D_{I_1I_3}|^2\sum_{i=1}^{2^N}\frac{\sin^2 x_{i,(I_1I_3)}t}{x_{i,(I_1I_3)}^2} \tag{3.47}$$

In the above calculation, polarization transfer from spin-1 is calculated to the other spins (I_2&I_3).

In accord with our earlier description, the inclusion of protons introduces additional oscillatory terms and are responsible for the depolarization observed in R^2 experi-

ments. The general expressions for $x_{i,(I_1I_2)}$ and $x_{i,(I_1I_3)}$ is represented by,

$$x_{i,(I_1I_2)} = \sqrt{|D_{I_1I_2}|^2 + \left(\frac{2(A_{I_1} - A_{I_2}) + \mathrm{y}_{i,(I_1I_2)}}{4}\right)^2} \tag{3.48}$$

$$x_{i,(I_1I_3)} = \sqrt{|D_{I_1I_3}|^2 + \left(\frac{2(A_{I_1} - A_{I_3}) + \mathrm{y}_{i,(I_1I_3)}}{4}\right)^2} \tag{3.49}$$

The 'y_i' coefficients depicted in Eqs. 3.48 & 3.49 could be systematically deduced from the general scheme depicted in Figures 3.3 & 3.4 respectively.

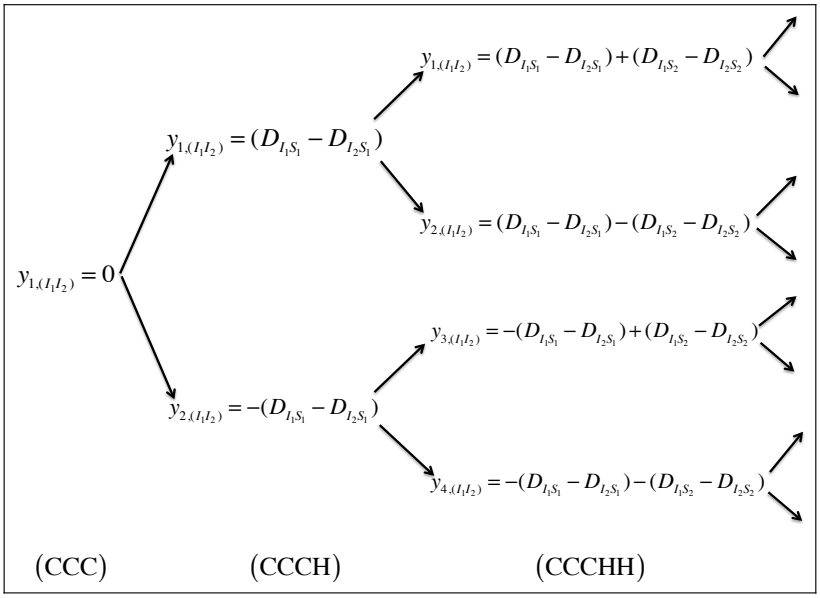

Figure 3.3: The figure depicts the flow chart for deriving the 'y' coefficients described in Eq. (3.48).

In contrast to other existing descriptions of the spin dynamics, the analytic expressions based on the reduced density matrix formulation are computationally robust and provide a simplified description of the magnetization exchange in R^2 experiments.

3.4 Results and discussion

3.4.1 R^2 phenomenon under CW decoupling

To elucidate the role of protons in R^2 experiments and to verify the validity of the analytic treatment presented in the previous sections, polarization exchange between carbon nuclei were investigated in the presence of protons through the model systems

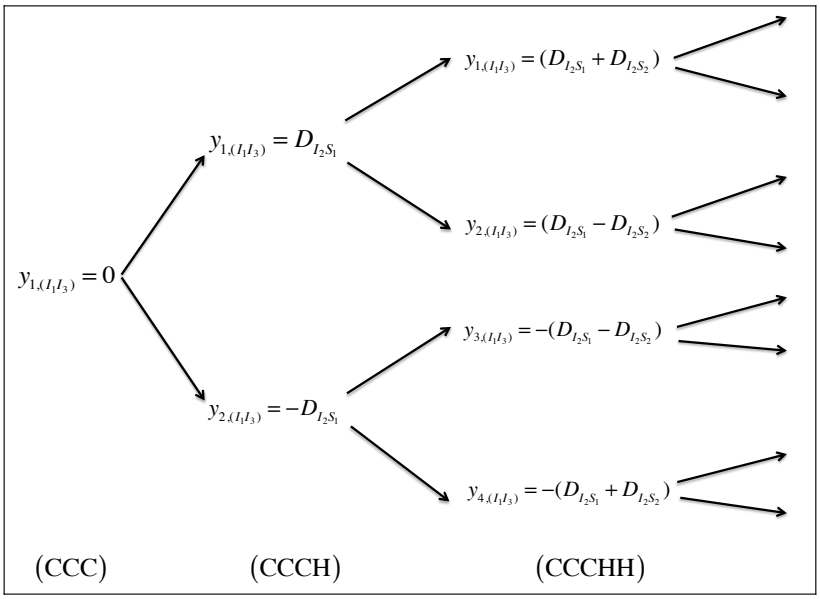

Figure 3.4: The figure depicts the flow chart for deriving the 'y' coefficients described in Eq. (3.49).

depicted in Fig. 3.5. The model systems depicted in Fig. 3.5 were constructed from the dipeptide, N-acetyl- (U-^{13}C,^{15}N) -L-valine-L-leucine (VL) (Fig.2.2). In all the simulations depicted in this section, polarization transfer from the carbonyl carbons to the aliphatic carbons were evaluated under constant mixing time by varying the sample spinning frequency. All the simulations presented in this study were performed at spectrometer frequency of 500 MHz (^1H frequency) with system parameters such as CSA, dipolar parameters obtained from Ref. (2).

To minimize the effects of protons, strong CW decoupling fields (of strength 100kHz) were employed on the proton channel during the dipolar mixing time. In Figure 3.6 (panels a, b, c), numerical simulations depicting polarization transfer in the model five-spin systems is presented. For illustrative purposes, the simulations emerging from the isolated two-spin model (panels: a1, b1, c1; dotted line) are compared with the model five-spin systems comprising of protons. Although, the simulations depicted in Figure 3.6 were performed at faster spinning frequencies (say 17-20 kHz) and involved strong decoupling fields on the proton channel, the residual ^{13}C-^1H dipolar interactions seem more influential in the weak-coupling regime (see panel c1).

Based on the analytic expressions (see Eqs. 3.33-3.35) and the coefficients listed

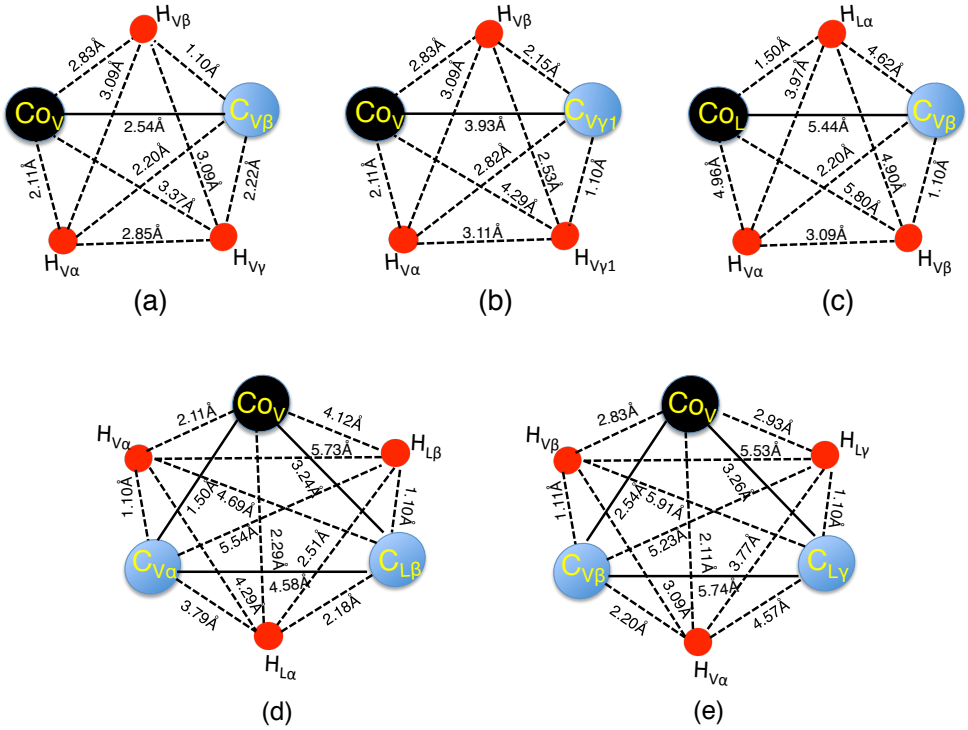

Figure 3.5: Model systems constructed from N-acetyl-L-Val-L-Leu (Figure 2.2) for describing the role of protons in R^2 experiments. The models depicted in panels (a), (b) and (c) resemble the $I_1 - I_2 - S_N$ system and correspond to the strong, intermediate and weak-coupling regimes, respectively. The models depicted in panels (d) and (e) are representative of the $I_1 - I_2 - I_3 - S_N$ system. The dipolar coupling constants between spin pairs are depicted in all the models.

in Table 3.2, this depolarization effect results from the D_{IS} coefficients associated with the longitudinal two-spin operators, $I_z S_z$. The longitudinal two-spin operators in the effective Hamiltonians (see Eq. 3.19) result from second-order cross-terms between the CSA interactions of the protons (δ_H^{CSA} = 2500Hz, η =0.3, 500MHz (^1H frequency)) and the heteronuclear ^{13}C-^1H dipolar interactions (i.e. ^1H-CSA X ^{13}C-^1H dipolar interactions). Consequently, in the absence of the ^1H-CSA interactions, the efficiency of transfer should improve at least in principle. This inference of ours is vindicated in the simulations depicted in the adjacent panel in Figure 3.6 (panels a2, b2, c2). The solid lines in the simulations (Figure 3.6, panels a2, b2, c2) represent the numerical five-spin simulations sans ^1H-CSA interactions, while the analytic simulations (dotted line) are based on the two-spin expressions derived in the chapter-2 (see Eq. 2.18). Hence, decoupling schemes that minimize /remove ^1H-CSA interactions

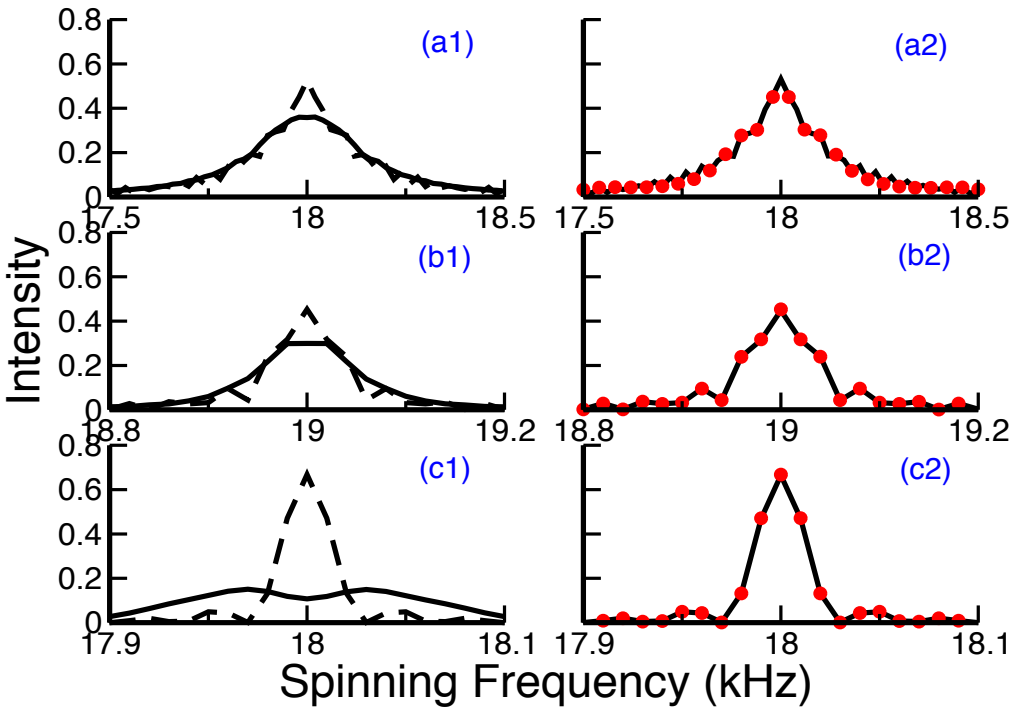

Figure 3.6: The figure depicts the role of ^1H-CSA interactions in the R^2 experiments. The solid lines (black) represent the simulations from SPINEVOLUTION,[27] while the analytic simulations (based on Eq. 3.34) are indicated by dots (red). The simulations depicted in panels (a1, a2), (b1, b2) and (c1, c2) correspond to the model systems (a), (b) and (c) depicted in Figure 3.5, respectively. The numerical simulations depicted in panels (a1, b1, c1) compare the magnetization exchange observed in the model five-spin system (solid lines) with the isolated two-spin system (broken lines) comprising of only ^{13}C nuclei. The simulations depicted in panels (a2, b2, c2) represent numerical five-spin simulations (solid lines) in the absence of ^1H-CSA interactions. In the absence of ^1H-CSA interactions (δ_H^{CSA} = 2500Hz, η =0.3, 500MHz (^1H frequency)), the simulations involving the model five-spin system resemble to that of an isolated two-spin system (indicated by red dots). In all the simulations presented, polarization transfer from the carbonyl carbon to the aliphatic carbon is calculated satisfying the appropriate N=1, R^2 conditions. All the remaining simulation perimeters are given in Table 2.4.

are beneficial in improving the polarization transfer efficiencies in R^2 experiments.

Since, ^1H-CSA interactions are non-zero in real experiments, incorporation of the CSA interactions along with the residual $^{13}C - {}^1H$ dipolar interactions is essential to quantify the magnetization exchange observed in R^2 experiments. In addition to decreasing the efficiency of transfer, the inclusion of the residual heteronuclear dipo-

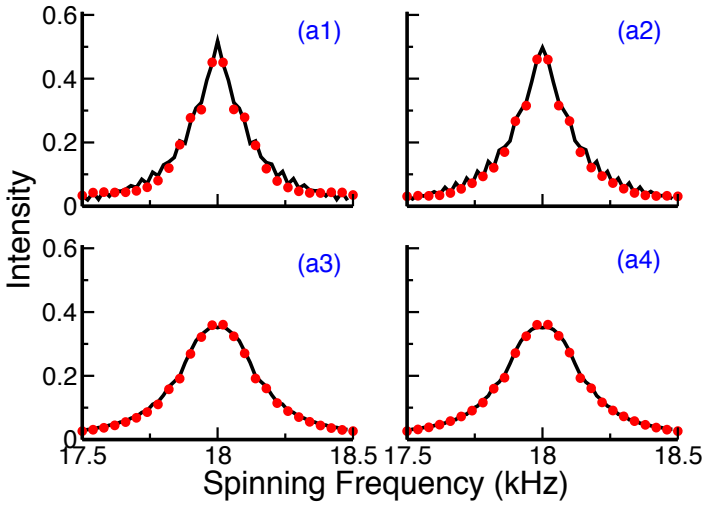

Figure 3.7: The figure depicts the polarization transfer from valine carbonyl carbon to valine beta carbon ($V_{Co} \rightarrow V_{C\beta}$, 2.54 Å) based on the model system $C_{Vo}C_{V\beta}H_{V\beta}H_{V\alpha}H_{V\gamma}$ (see Figure 3.5a). The role of protons on the exchange dynamics is illustrated through simulations comprising of two (a1, $C_{Vo}C_{V\beta}$), three (a2, $C_{Vo}C_{V\beta}H_{V\alpha}$), four (a3, $C_{Vo}C_{V\beta}H_{V\beta}H_{V\alpha}$) and five (a4, $C_{Vo}C_{V\beta}H_{V\beta}H_{V\alpha}H_{V\gamma}$) spin systems. The analytic simulations (dots) were based on Eq. (3.34) and correspond to the N=1, R^2 condition. All the remaining simulation perimeters are given in Table 2.4.

lar interactions ($^{13}C - {}^{1}H$) broadens the R^2 exchange profile. This observation is important, since, the standard approach of employing isolated two-spin models along with phenomenological damping terms does not replicate the broadening observed in the exchange trajectories in R^2 experiments. Additionally, the ambiguity associated with the magnitude of the damping terms limits the utility of such methods in the estimation of distances. Since biophysical applications of SSNMR entail the measurement of long-range interactions /couplings, interpretation of the exchange trajectories is very crucial in the weak-coupling regime. To address this issue, Baldus and co-workers[28] proposed the multi-spin (MS) analysis approach for quantifying the experimental trajectories obtained under R^2 conditions. Employing certain standard geometric parameters (that includes both the orientation and magnitude of the residual heteronuclear dipolar interactions), the exchange trajectories were numerically simulated with few neighboring protons. Interestingly, the reduced density matrix formalism presented in this thesis, provides a convenient yet accurate description of the exchange dynamics in the presence of protons. To illustrate the effects

/role of neighboring protons on the exchange trajectories, polarization transfer under different coupling environments (with regard to $^{13}C - ^{13}C$ couplings) were investigated through model systems comprising of two carbons coupled to finite number of neighboring protons i.e. $I_1 - I_2 - S_N$ system.

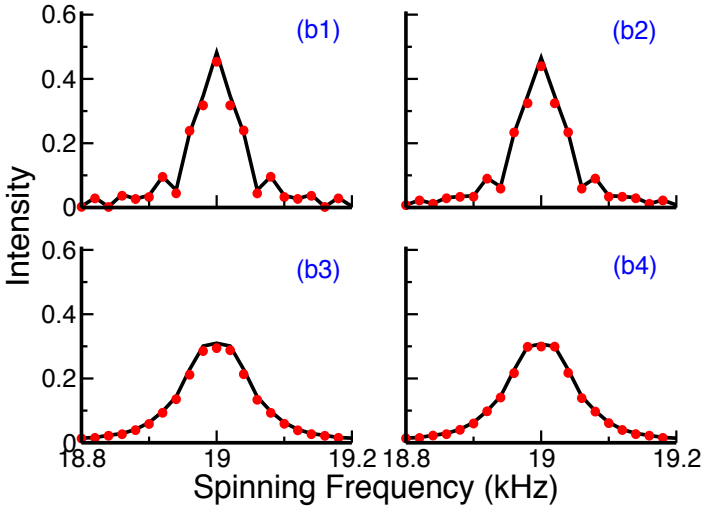

Figure 3.8: The figure depicts the polarization transfer from valine carbonyl carbon to valine gamma carbon ($V_{Co} \rightarrow V_{C\gamma_1}$, 3.90 Å) based on the model system $C_{Vo}C_{V\gamma 1}H_{V\beta}H_{V\alpha}H_{V\gamma 1}$ (see Figure 3.5b). The role of protons on the exchange dynamics is illustrated through simulations comprising of two (b1, $C_{Vo}C_{V\gamma 1}$), three (b2, $C_{Vo}C_{V\gamma 1}H_{V\beta}$), four (b3, $C_{Vo}C_{V\gamma 1}H_{V\beta}H_{V\gamma 1}$) and five (b4, $C_{Vo}C_{V\gamma 1}H_{V\beta}H_{V\alpha}H_{V\gamma 1}$) spin systems. The analytic simulations (dots) were based on Eq. (3.34) and correspond to the N=1, R^2 condition. All the remaining simulation perimeters are given in Table 2.4.

In Figure 3.7, polarization transfer from the valine carbonyl carbon to valine beta carbon ($V_{Co} \rightarrow V_{C\beta}$, 2.54 Å) in the model five-spin system (Figure 3.5a) is presented. The effect of protons on this model system is depicted methodically by increasing the number of neighboring protons through panels 'a2, a3 and a4', respectively. As depicted, the decrease in the efficiency in the presence of neighboring protons is only marginal (decreases by 20%) when compared to the isolated two-spin case (see panel a1).

To substantiate the validity of the analytic results, additional simulations depicting polarization transfer in the intermediate (transfer from valine carbonyl carbon to valine beta carbon, $V_{Co} \rightarrow V_{C\gamma_1}$, 3.90 Å) and weak-coupling regimes (transfer from leucine carbonyl carbon to valine beta carbon, $Leu_{Co} \rightarrow V_{C\beta}$, 5.44 Å) were further

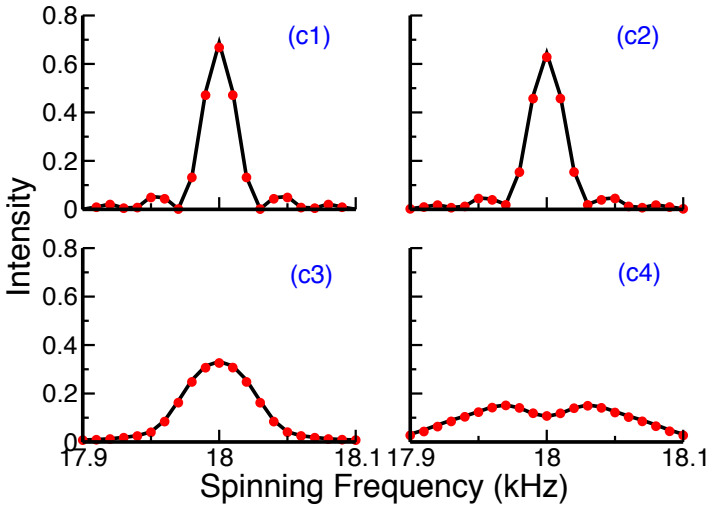

Figure 3.9: The figure depicts the polarization transfer from leucine carbonyl carbon to valine beta carbon ($Leu_{Co} \rightarrow V_{C\beta}$, 5.44 Å) based on the model system $C_{Lo}C_{V\beta}H_{V\beta}H_{V\alpha}H_{L\alpha}$ (see Figure 3.5c). The role of protons on the exchange dynamics is illustrated through simulations comprising of two (c1, $C_{Lo}C_{V\beta}$), three (c2, $C_{Lo}C_{V\beta}H_{V\alpha}$), four (c3, $C_{Lo}C_{V\beta}H_{V\beta}H_{V\alpha}$) and five (c4, $C_{Lo}C_{V\beta}H_{V\beta}H_{V\alpha}H_{L\alpha}$) spin systems. The analytic simulations (dots) were based on Eq. (3.34) and correspond to the N=1, R^2 condition. All the remaining simulation perimeters are given in Table 2.4.

investigated and are depicted in Figures 3.8 and 3.9, respectively. In contrast to the intermediate coupling regime, the depolarization effects arising from neighboring protons is severe in the weak-coupling regime. Since, the magnitude of the dipolar coupling constant decreases with increase in the interatomic distance, quantification of results in the weak-coupling regime entails accurate description of the underlying spin dynamics. Additionally, off-resonant polarization exchange (broadening of the R^2 condition) is observed prominently in the weak coupling regime.

As depicted, the analytic simulations (Figures 3.8-3.10) emerging from the reduced density matrix approach are in excellent agreement with numerical simulations. In contrast to exact numerical methods, the analytic simulations are computationally less intense and present an attractive tool for simulating exchange trajectories involving an isolated spin pair coupled to a surrounding bath of protons (model $I_1-I_2-S_N$). The damping effect introduced by the surrounding protons, depend on the magnitude of the residual ^{13}C-^1H interactions in addition to the ^1H-CSA's and vary depending on the spin topology and other external parameters (such as decoupling field

strengths, magnetic field strengths, spinning frequencies etc.) employed in the simulations. Hence, the practice of employing uniform damping constant (T_{ZQ}) for all the data points in the resonance width experiments seem inappropriate. Although, such approaches could result in appreciable results in the strong coupling regime, they are of limited utility in the weak-coupling regime and could well be the reason behind the inaccuracies reported in the measurement of long-range distances in the literature.[1–4]

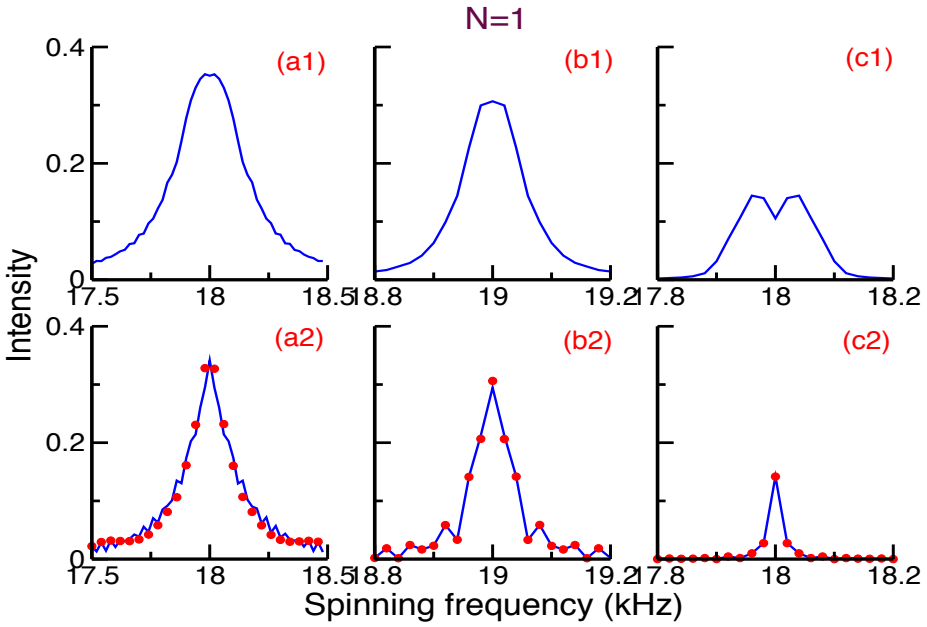

Figure 3.10: The figure depicts the polarization transfer from $V_{Co} \rightarrow V_{C\beta}$, 2.54 Å (a1, a2), $V_{Co} \rightarrow V_{C\gamma_1}$, 3.90 Å (b1, b2) an $Leu_{Co} \rightarrow V_{C\beta}$, 5.44 Å (c1, c2) correspond to the N=1, R^2 condition. The panels (a1, b1, c1) represent the polarization transfer in five-spin systems in model systems shown in Figures 3.5 (a, b, c) respectively. The panels (a2, b2, c2) represent the polarization transfer in the corresponding two-spin (C-C) systems along with the damping term, exp(-t/T), used to match the intensity in the five-spin systems (panels a1, b1, c1). The simulations in panels (a2, b2, c2) are generated using Liouville matrix (solid line) and the reduced density matrix theory (dots) (Eq. 3.34). The phenomenological damping constants (T_{zq}) used in the simulations corresponding to strong, medium and weak coupling regimes are 72 ms (a2), 61ms (b2) and 19 ms (c2) respectively. All the remaining simulation perimeters are given in Table 2.4.

To illustrate this aspect, simulations emerging from isolated two-spin models in the presence of phenomenological damping terms are compared with the chosen model

five-spin systems both in the N=1 (Fig. 3.10) and N=2 (Fig. 3.11) R^2 matching conditions. As depicted in the Figures 3.10 & 3.11, the simulations emerging from the isolated two-spin model (inclusive of phenomenological damping terms) are in complete disagreement (in particular for the N=1, R^2 conditions, see Figure 3.10) with those emerging from the model five spin systems in all the regimes. Although, the inclusion of a damping term lowers the intensity in the simulations based on the isolated two-spin framework, the broadening induced by the presence of residual heteronuclear dipolar interactions is not reproduced.

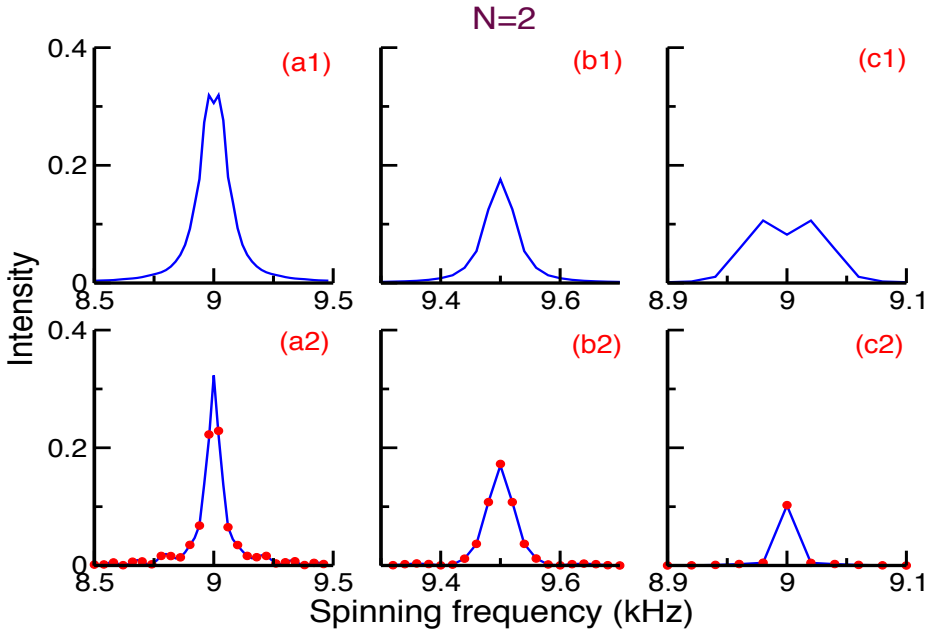

Figure 3.11: The figure depicts the polarization transfer from $V_{Co} \rightarrow V_{C\beta}$, 2.54 Å (a1, a2), $V_{Co} \rightarrow V_{C\gamma_1}$, 3.90 Å (b1, b2) an $Leu_{Co} \rightarrow V_{C\beta}$, 5.44 Å (c1, c2) correspond to the N=2, R^2 condition. The panels (a1, b1, c1) represent the polarization transfer in five-spin systems in model systems shown in Figures 3.5 (a, b, c) respectively. The panels (a2, b2, c2) represent the polarization transfer in the corresponding two-spin (C-C) systems along with the damping term, exp(-t/T), used to match the intensity in the five-spin systems (panels a1, b1, c1). The simulations in panels (a2, b2, c2) are generated using Liouville matrix (solid line) and the reduced density matrix theory (circles) (Eq. 3.34). The phenomenological damping constants (T_{zq}) used in the simulations corresponding to strong, medium and weak coupling regimes are 54 ms (a2), 40 ms (b2) and 18 ms (c2) respectively. All the remaining simulation perimeters are given in Table 2.4.

Interestingly, the simulations in the N=2, R^2 experiments, seem to have a better

agreement between the two models. Although, the discrepancy is prominent in the weaker-coupling regime (see panels c1, c2 in Fig. 3.11), the agreements are satisfactory in the strong and medium coupling regime. Since existing theoretical models employ an isolated two-spin framework for data analysis, implementation of R^2 experiments for measuring interatomic $^{13}C - ^{13}C$ distances have always been limited to the N=2 matching conditions.[1,2] Often in such descriptions, the inaccuracies in the estimation of distances in the weak-coupling regime have been incorrectly attributed to experimental imperfections and other reasons such as zero-quantum relaxation etc. The present study clearly highlights the limitations of existing theoretical models and also explicates the actual reason behind the non-implementation of the R^2 experiments at the N=1 matching conditions.

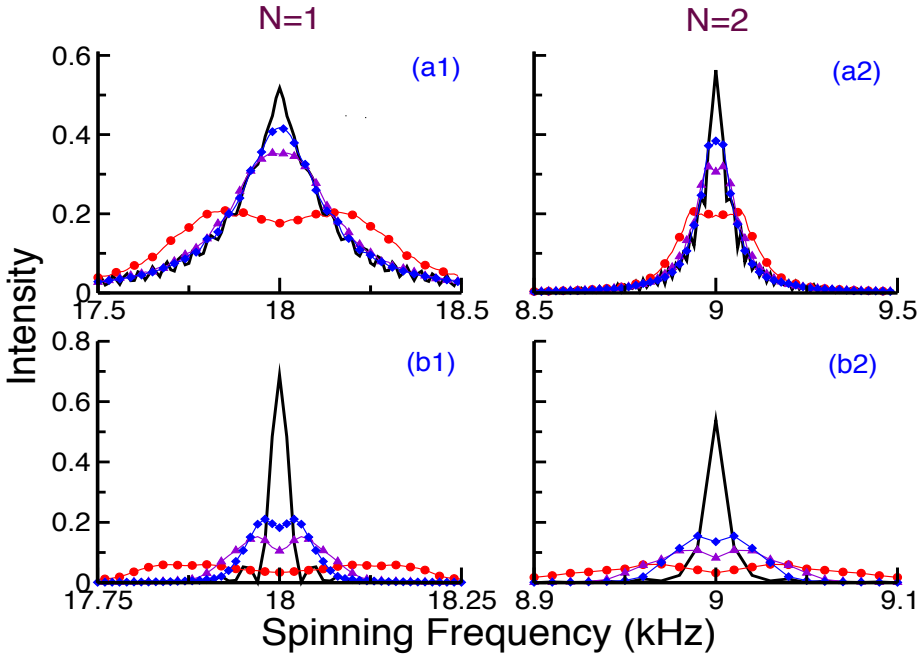

Figure 3.12: The figure depicts the polarization transfer from $V_{Co} \rightarrow V_{C\beta}$, 2.54 Å (N=1, a1; N=2, a2) in a five-spin model system (Figure 3.5a) and from $Leu_{Co} \rightarrow V_{C\beta}$, 5.44 Å (N=1, b1; N=2, b2) in a five-spin model system (Figure 3.5c) in the presence of different RF decoupling amplitudes [50kHz (circles), 100kHz (triangle up) and 150kHz (diamonds)]. For comparison purposes, polarization transfer in corresponding two-spin system (C-C) (black, solid line) are depicted in all the panels under N=1 & 2, R^2 conditions. All the remaining simulation perimeters are given in Table 2.4.

To illustrate the role of the RF amplitudes involved in heteronuclear decoupling

schemes in R^2 experiments, simulations depicting polarization transfer under different RF amplitudes is presented in Figure 3.12. As depicted, the decrease in the magnitude of the RF amplitude broadens the R^2 matching condition, and is currently termed as homogeneously broadened R^2 experiment. Employing this approach, $^{13}C - {}^{13}C$ distance measurements in proteins have recently been demonstrated by Ladhizhansky and coworkers.[3,29] Employing an isolated two-spin model and a phenomenological damping term, the polarization transfer under N=2, R^2 conditions has been employed to extract interatomic distances. The inaccuracies in their measurements have been attributed to multi-spin effects and other relaxation mechanisms during the experiments. However, our investigations contradict their claims on the inaccuracies involved in the $^{13}C - {}^{13}C$ distance measurements based on R^2 experiments.

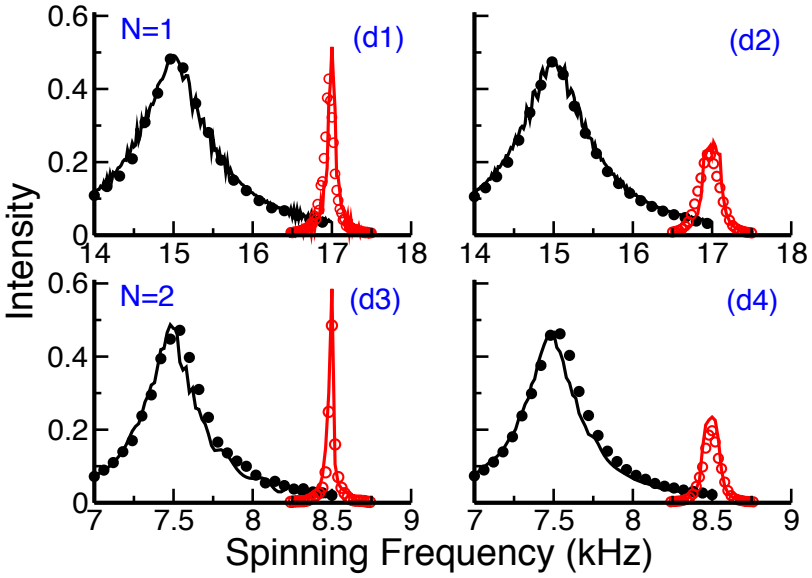

Figure 3.13: The figure depicts the polarization transfer from valine carbonyl carbon to valine alpha carbon and leucine beta carbon ($V_{Co} \rightarrow V_{C\alpha}$, 1.50 Å and $V_{Co} \rightarrow L_{C\beta}$, 3.24 Å) based on the model system $C_{Vo}C_{V\alpha}C_{L\beta}H_{L\beta}H_{L\alpha}H_{V\alpha}$ (see Figure 3.5d). To illustrate the multi-spin effects observed in band-selective experiments, polarization transfer corresponding to both N=1 (panels d1, d2) and N=2 (panels d3, d4) matching conditions are depicted. Additionally, simulations both in the absence (panels d1, d3) and presence of protons (panels d2, d4) are also depicted. The analytic simulations (dots) were performed based on Eqs. 3.46 & 3.47. All the remaining simulation perimeters are given in Table 2.4.

To further substantiate the validity of the analytic theory presented in this thesis, the role of neighboring carbons in the R^2 magnetization exchange experiments were investigated. The $I_1 - I_2 - I_3 - S_N$ spin system serves as a suitable model system for describing band-selective transfer of polarization from carbonyl carbons to the aliphatic carbons encountered in typical biological solids. In the simulations depicted below, polarization transfer from I_1 (representative of the carbonyl carbon) to I_2, I_3 (representative of the carbons in the aliphatic region) is depicted in the presence of coupling to the surrounding proton reservoir. Since the chemical shifts of the carbons in the aliphatic region are very similar, only band-selective transfer of polarization is possible.

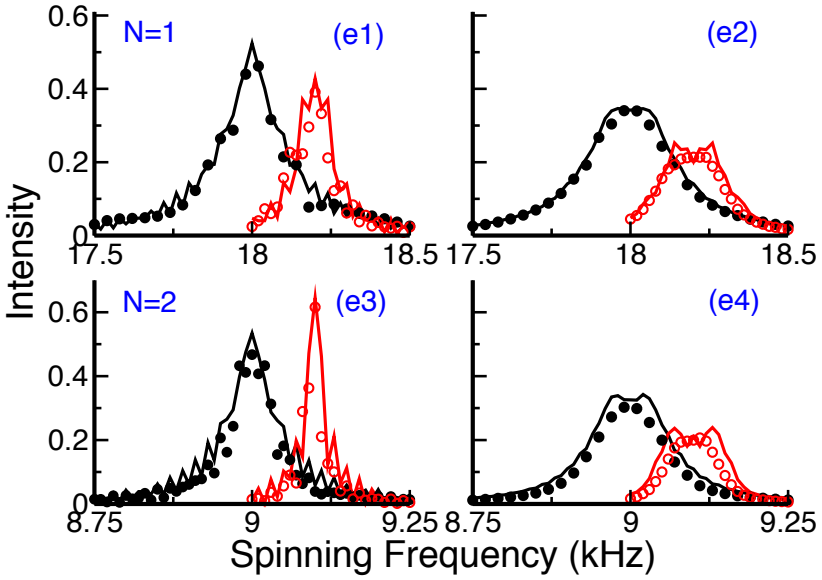

Figure 3.14: The figure depicts the polarization transfer from valine carbonyl carbon to valine beta carbon and leucine gamma carbon ($V_{Co} \rightarrow V_{C\beta}$, 2.54 Å and $V_{Co} \rightarrow L_{C\gamma}$, 3.26 Å) based on the model system $C_{Vo}C_{V\beta}C_{L\gamma}H_{V\beta}H_{L\gamma}H_{V\alpha}$ (see Figure 3.5e). To illustrate the multi-spin effects observed in band-selective experiments, polarization transfer corresponding to both N=1 (panels e1, e2) and N=2 (panels e3, e4) matching conditions are depicted. Additionally, simulations both in the absence (panels e1, e3) and presence of protons (panels, e2, e4) are also depicted. The analytic simulations (dots) were performed based on Eqs. 3.46 & 3.47. All the remaining simulation perimeters are given in Table 2.4.

The chemical shifts of the carbons present in the models depicted in Figure 3.5 (see panels d, e) correspond to this situation and present an excellent system to verify

the validity of our analytic theory (see Eqs. 3.45-3.47). In Figure 3.13, polarization transfer from the valine carbonyl carbon to the aliphatic carbons (valine alpha carbon and Leucine beta carbon, ($V_{Co} \rightarrow V_{C\alpha}$, 1.50 Å; $V_{Co} \rightarrow L_{C\beta}$, 3.24 Å)) is depicted both in the absence (see panel d1 for N=1; d3 for N=2) and presence of the neighboring protons (see panel d2 for N=1; d4 for N=2).

Although, the model system (Figure 3.5d) comprises of both a stronger and a weaker coupling, the effects of dipolar truncation are absent in the isolated three-spin system ($I_1 - I_2 - I_3$) (panels: d1, d3). However, in the presence of protons, the efficiency of transfer from $V_{Co} \rightarrow L_{C\beta}$ (r=3.24 Å) gets diminished (panels: d2, d4) owing to the residual ^{13}C-^{1}H interactions (refer to Eq. 3.47) as opposed to the stronger $V_{Co} \rightarrow V_{C\alpha}$ coupling. To further substantiate this aspect, simulations depicting polarization transfer from the valine carbonyl carbon to the aliphatic carbons (valine beta carbon, Leucine gamma carbon ($V_{Co} \rightarrow V_{C\beta}$, 2.54 Å; $V_{Co} \rightarrow L_{C\gamma}$, 3.26 Å)) is depicted is Figure 3.14, both in the absence (see panels e1, e3) and presence of neighboring protons (see panels e2, e4). In contrast to the previous model (Figure 3.5d), the resonance conditions in the chosen system (model 3.5e) are strongly overlapping. As depicted, the analytic simulations based on the reduced density matrix approach are in excellent agreement with the numerical simulations and present an attractive tool for simulating experimental data in band-selective R^2 experiments. In comparison to numerical methods and other operator-space based analytic descriptions of the spin dynamics, the simulations emerging from the reduced density matrix approach are computationally less intense and are suitable for fitting experimental data with multiple free-fit parameters inclusive of interatomic distances and CSA parameters.

3.4.2 R^2 phenomenon under TPPM decoupling

To improve the efficiency of polarization transfer, an alternate decoupling scheme in the form of TPPM[11] was employed during the R^2 mixing period. In contrast to the CW experiment, the TPPM sequence (Fig. 3.15) comprises of two pulses that are phase shifted by a constant factor ($\Delta\phi$), the flip angles of the two pulses are chosen to be 180° with a phase difference of 15°.

In Figures 3.16 (panels: a1, b1, c1) & 3.17 (panels: d1, e1, f1), polarization

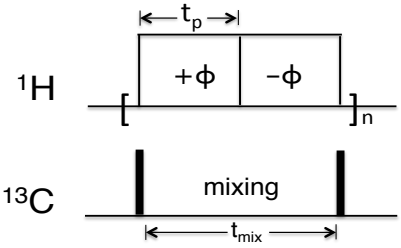

Figure 3.15: Schematic diagram depicting the TPPM[11] decoupling during mixing time in R^2 experiments

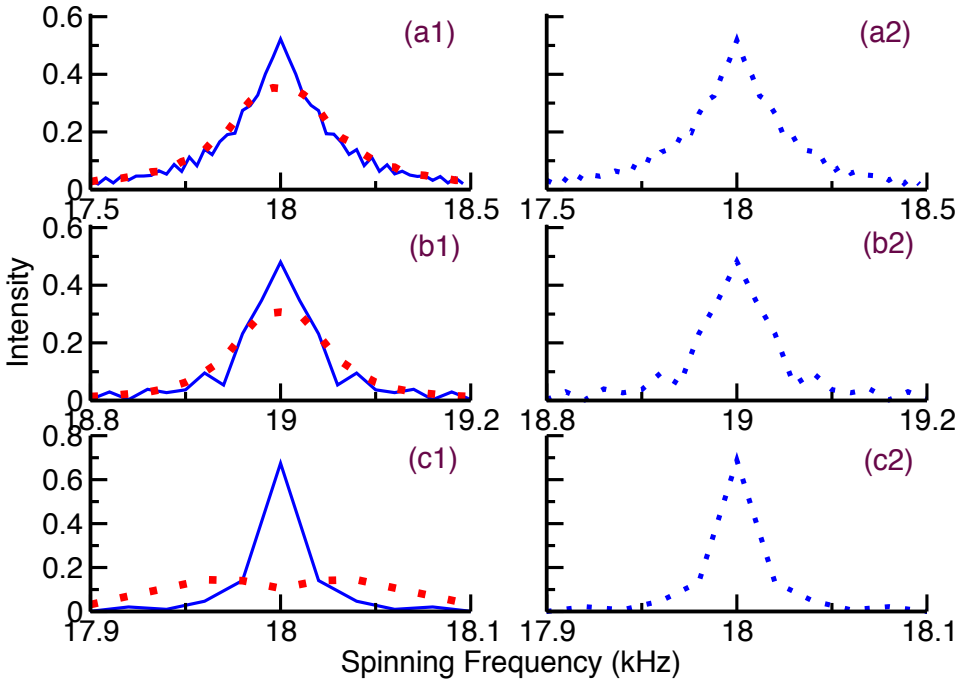

Figure 3.16: The figure depicts the polarization transfer in five-spin systems (Figure 3.5: a (panel, a1), b (panel, b1), c (panel, c1)) in the presence of TPPM decoupling on ^1H-channel under N=1, R^2 conditions. Panels (a1, b1, c1) consist of the analytic simulations generated under the TPPM (solid line) and the CW decoupling (dots) schemes in five-spin systems at the RF, 100kHz with the phase difference ($\Delta\phi$), 15°. The analytic simulations (panels: a2, b2, c2) depicting the polarization transfer in the corresponding isolated two-spin (C-C) systems are presented for comparison. All the remaining simulation perimeters are given in Table 2.4.

transfer in R^2 experiments under CW and TPPM decoupling sequences is illustrated. As depicted, the efficiency of polarization transfer is enhanced and is very similar to those obtained for an isolated spin pair (panels: a2, b2, c2 and panels: d2, e2, f2).

Specifically, the enhancement in the weak coupling limit is appreciable. The dotted lines in panels a1, b1, c1 (Figures 3.16 & 3.17) represent the transfer under CW decoupling while solid lines represent simulations from TPPM decoupling scheme. To explain the better performance of the TPPM decoupling scheme, an analytic theory is presented in the Appendix-II(a). In contrast to the description in the CW case, the RF Hamiltonian in the rotating frame is time-dependent with modulation frequency, ω_m.

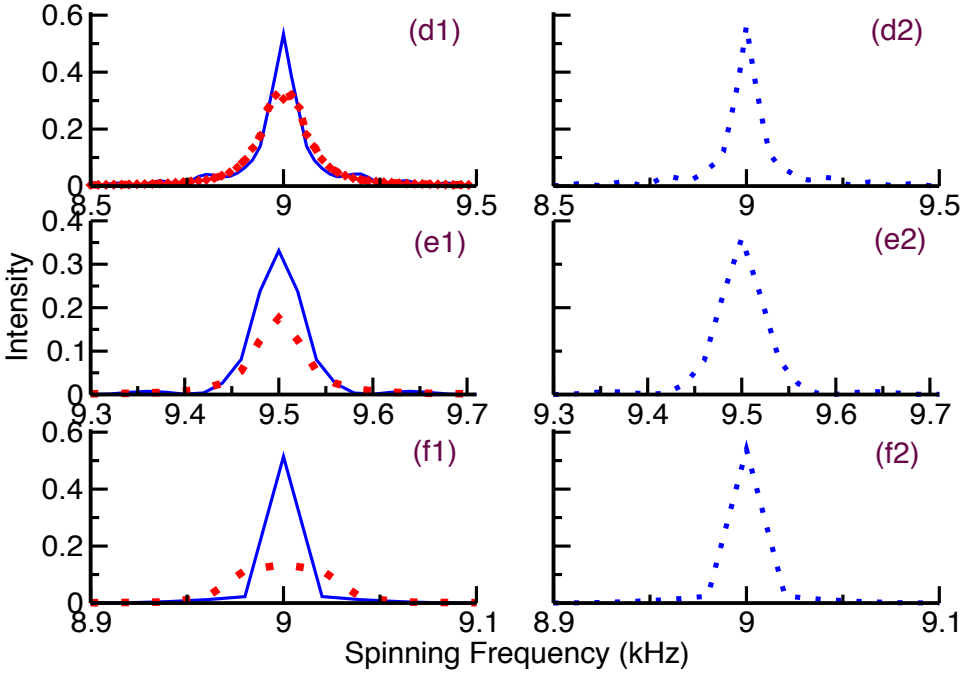

Figure 3.17: The figure depicts the polarization transfer in five-spin systems (Figure 3.5: a (panel, d1), b (panel, e1), c (panel, f1)) in the presence of TPPM decoupling on ^1H-channel under N=2, R^2 conditions. Panels (d1, e1, f1) consist of the analytic simulations generated under the TPPM (solid line) and the CW decoupling (dots) schemes in five-spin systems at the RF, 100kHz for strong and intermediate (panels: d1, e1) and 150kHz for weak C-C coupling regimes (panel, f1) with the phase difference ($\Delta\phi$), 15°. The analytic simulations (panels: d2, e2, f2) depicting the polarization transfer in the corresponding isolated two-spin (C-C) systems are presented for comparison. All the remaining simulation perimeters are given in Table 2.4.

To elucidate the role of the modulation frequency, the RF Hamiltonian on the proton channel is initially transformed using the transformation function, S_1. Employing the transformation function (S_1), the internal Hamiltonians such as heteronuclear

dipolar interactions are further transformed resulting in two modulation frequencies, ω_r & ω_m. Employing the procedure described, the effective Hamiltonian was derived (see Appendix-II(a)). As described, the residual heteronuclear dipolar interactions and the ^1H-CSA interactions are scaled significantly and are primarily responsible for improving the efficiency of transfer in R^2 experiment. As described in Figures 3.16 & 3.17, the analytic simulations emerging from the TPPM decoupled scheme yield results that are in excellent agreement with those emerging from exact numerical methods. As depicted in Figures 3.16-3.17, in the presence of TPPM decoupling, the exchange trajectories obtained in the model five-spin system resemble to that of the isolated two-spin system. Hence, in the presence of TPPM decoupling, the depolarization effects due to residual heteronuclear dipolar interactions (intramolecular) are removed from the R^2 experiments.

3.5 Conclusions

In summary, the reduced density matrix approach presented in this thesis is well suited for describing the multi-spin effects arising in the polarization transfer experiments involved in R^2 experiments. The equations are very similar to those derived for an isolated spin pair and are well suited for simulations involving multiple fit parameters. The factors responsible depolarization in CW experiments are analyzed in detail and are well described through comparisons with analytic and numerical simulations. The depolarization resulting from heteronuclear dipolar interactions are significantly removed in the TPPM decoupling scheme. Hence, the depolarization observed in experiments (under TPPM) would result from other factors such as inter-molecular effects and are presently beyond the scope of this thesis.

3.6 Appendix-II

a. Effect of TPPM decoupling

The basic TPPM[11] sequence involves two phases, $\pm\phi$ with π pulses of length, $t_p = {}^{\pi}/_{\omega_{rf}}$ (see Figure 3.15). Since, there is a phase variation on the ^1H channel during the mixing time of ^{13}C nuclei, the heteronuclear dipolar interactions are periodically modulated by both the MAS as well as the RF pulse sequence.

To describe the role of protons under TPPM decoupling in the polarization exchange between ^{13}C nuclei in R^2 experiments, a model system ($I_1{-}I_2{-}S_N$) comprising of two carbons (denoted by I) coupled to N-protons (denoted by S) was chosen. The time-dependent MAS Hamiltonian for such a system is represented by,

$$H(t) = H^{C}_{System}(t) + H^{C-H}_{System-Bath}(t) + H^{H}_{Bath}(t) + H^{H}_{RF}(t) \tag{3.50}$$

In the above Hamiltonian, $H^{C}_{System}(t)$ denotes the Hamiltonian of the system of interest ($^{13}C - {}^{13}C$) comprising mainly of the chemical shift and dipolar interactions. In a similar vein, $H^{H}_{Bath}(t)$ denotes the interactions present among the surrounding bath of protons. The coupling of the system with the surroundings is represented by $H^{C-H}_{System-Bath}(t)$ and comprises of the heteronuclear dipolar interactions. The quantum mechanical representation of all these interactions are similar as given in the previous sections.

The time-dependent RF Hamiltonian with the Fourier series form of the two phase modulation is represented by

$$H^{H}_{RF}(t) = \omega_{rf}\cos\phi\sum_{j=1}^{N} S_{jx} + \frac{4}{\pi}\sin\phi\sum_{j=1}^{N}\sum_{n=-\infty,odd}^{\infty}\frac{1}{n}\sin(n\omega_m t)S_{jy} \tag{3.51}$$

To deduce the R^2 matching conditions and describe the effects of phase modulated decoupling, the Hamiltonian in the rotating frame (Eq. 3.50) is transformed into an interaction frame defined by the transformation operators, $U_1 = e^{in\omega_r t I_{1z}}e^{-in\omega_r t I_{2z}}$ and $U_2 = \sum_{j=1}^{N} e^{i\frac{\pi}{2}S_{jy}}$ as represented below.

$$\tilde{H}(t) = U_2 U_1 H(t) U_1^{-1} U_2^{-1} \tag{3.52}$$

$$\tilde{H}(t) = \tilde{H}^{C}_{System}(t) + \tilde{H}^{C-H}_{System-Bath}(t) + \tilde{H}^{H}_{Bath}(t) + \tilde{H}^{H-H}_{Bath}(t) + \tilde{H}^{H}_{RF} \tag{3.53}$$

A detailed representation of the RF Hamiltonian after the transformation defined above is given below.

$$\tilde{H}^H_{RF}(t) = \omega_{rf}\cos\phi\sum_{j=1}^{N} S_{jz} + \frac{4}{\pi}\sin\phi\sum_{j=1}^{N}\sum_{n=-\infty,odd}^{\infty}\frac{1}{n}\sin(n\omega_m t)S_{jy} \tag{3.54}$$

All the representations corresponding to the remaining interactions are similar to those given in the earlier sections.

Under the assumption that the modulation frequency (ω_m) is equal to the static part of the RF Hamiltonian, the Hamiltonian in Eq. (3.53) is transformed into the modulation frequency frame defined by the transformation operator, $U_3 = \sum_{j=1}^{N} e^{i\omega_m t S_{jz}}$ as represented below.

$$\tilde{\tilde{H}}(t) = U_3 H(t) U_3^{-1} \tag{3.55}$$

$$\tilde{\tilde{H}}(t) = \tilde{H}^C_{System}(t) + \tilde{\tilde{H}}^{C-H}_{System-Bath}(t) + \tilde{\tilde{H}}^H_{Bath}(t) + \tilde{\tilde{H}}^{H-H}_{Bath}(t) + \tilde{\tilde{H}}^H_{RF} \tag{3.56}$$

The detailed form of an each interaction is given below.

$$\tilde{\tilde{H}}^{C-H}_{System-Bath}(t) = -\sum_{m=-2;\neq 0}^{2}\sum_{i=1}^{2}\sum_{j=1}^{N}\omega^{(m)}_{I_i S_j} e^{im\omega_r t} 2\left[I_{iz}S_{jx}\cos\omega_m t - I_{iz}S_{jy}\sin\omega_m t\right] \tag{3.57}$$

$$\tilde{\tilde{H}}^H_{Bath}(t) = -\sum_{m=-2}^{2}\sum_{j=1}^{N}\omega^{(m)}_{S_j} e^{im\omega_r t}\left(S_{jx}\cos\omega_m t - S_{jy}\sin\omega_m t\right) \tag{3.58}$$

$$\begin{aligned}\tilde{\tilde{H}}^{H-H}_{Bath}(t) = &\sum_{m=-2;\neq 0}^{2}\sum_{j,k=1;j<k}^{N}\omega^{(m)}_{S_jS_k} e^{im\omega_r t}\left[-S_{jz}S_{kz} - \tfrac{3}{2}\sin 2\omega_m t\left(S_{jx}S_{ky} + S_{jy}S_{kx}\right)\right] + \\ &\sum_{m=-2;\neq 0}^{2}\sum_{j,k=1;j<k}^{N}\omega^{(m)}_{S_jS_k} e^{im\omega_r t}\left[\sin^2\omega_m t\left(2S_{jy}S_{ky} - S_{jx}S_{kx}\right)\right] + \\ &\sum_{m=-2;\neq 0}^{2}\sum_{j,k=1;j<k}^{N}\omega^{(m)}_{S_jS_k} e^{im\omega_r t}\left[\cos^2\omega_m t\left(2S_{jx}S_{kx} - S_{jy}S_{ky}\right)\right]\end{aligned} \tag{3.59}$$

$$\begin{aligned}\tilde{\tilde{H}}^H_{RF}(t) = &\frac{2}{\pi}\sin\phi\sum_{j=1}^{N}S_{jx} + \\ &\frac{2}{\pi}\sin\phi\sum_{j=1}^{N}\sum_{n=-\infty,odd}^{\infty}\frac{1}{n}\left[\sin(n+1)\omega_m t + \sin(n-1)\omega_m t\right]S_{jy} + \\ &\frac{2}{\pi}\sin\phi\sum_{j=1}^{N}\sum_{n=-\infty,odd}^{\infty}\frac{1}{n}\left[\cos(n-1)\omega_m t - \cos(n+1)\omega_m t\right]S_{jx}\end{aligned} \tag{3.60}$$

where $|n-1| \neq 0$ $(n \neq 1)$ in the above RF Hamiltonian.

To simplify the description, the Hamiltonian is transformed by an unitary transformation function, $U_4 = \sum_{j=1}^{N} e^{i\frac{\pi}{2}S_{jy}}$.

$$\tilde{\tilde{\tilde{H}}}(t) = U_4 H(t) U_4^{-1} \tag{3.61}$$

$$\tilde{\tilde{\tilde{H}}}(t) = \tilde{H}^{C}_{System}(t) + \tilde{\tilde{\tilde{H}}}^{C-H}_{System-Bath}(t) + \tilde{\tilde{\tilde{H}}}^{H}_{Bath}(t) + \tilde{\tilde{\tilde{H}}}^{H-H}_{Bath}(t) + \tilde{\tilde{\tilde{H}}}^{H}_{RF} \tag{3.62}$$

The detailed form of an each interaction is given below.

$$\tilde{\tilde{\tilde{H}}}^{C-H}_{System-Bath}(t) = -\sum_{m=-2;\neq 0}^{2}\sum_{i=1}^{2}\sum_{j=1}^{N}\omega^{(m)}_{I_iS_j}e^{im\omega_r t}2\left[I_{iz}S_{jz}\cos\omega_m t - I_{iz}S_{jy}\sin\omega_m t\right] \tag{3.63}$$

$$\tilde{\tilde{\tilde{H}}}^{H}_{Bath}(t) = -\sum_{m=-2}^{2}\sum_{j=1}^{N}\omega^{(m)}_{S_j}e^{im\omega_r t}\left(S_{jz}\cos\omega_m t - S_{jy}\sin\omega_m t\right) \tag{3.64}$$

$$\begin{aligned}\tilde{\tilde{\tilde{H}}}^{H-H}_{Bath}(t) = &\sum_{m=-2;\neq 0}^{2}\sum_{j,k=1;j<k}^{N}\omega^{(m)}_{S_jS_k}e^{im\omega_r t}\left[\frac{3}{2}S_{jz}S_{kz} - \frac{3}{2}S_{jy}S_{ky} - S_{jx}S_{kx}\right] - \\ &\sum_{m=-2;\neq 0}^{2}\sum_{j,k=1;j<k}^{N}\omega^{(m)}_{S_jS_k}e^{im\omega_r t}\frac{3}{2}\left[\sin 2\omega_m t\left(S_{jz}S_{ky} + S_{jy}S_{kz}\right)\right] + \\ &\sum_{m=-2;\neq 0}^{2}\sum_{j,k=1;j<k}^{N}\omega^{(m)}_{S_jS_k}e^{im\omega_r t}\frac{1}{2}\left[\cos 2\omega_m t\left(S_{jz}S_{kz} + S_{jy}S_{ky}\right)\right]\end{aligned} \tag{3.65}$$

$$\begin{aligned}\tilde{\tilde{\tilde{H}}}^{H}_{RF}(t) = &\frac{2}{\pi}\sin\phi\sum_{j=1}^{N}S_{jz} + \\ &\frac{2}{\pi}\sin\phi\sum_{j=1}^{N}\sum_{n=-\infty,odd}^{\infty}\frac{1}{n}\left[\sin(n+1)\omega_m t + \sin(n-1)\omega_m t\right]S_{jy} + \\ &\frac{2}{\pi}\sin\phi\sum_{j=1}^{N}\sum_{n=-\infty,odd}^{\infty}\frac{1}{n}\left[\cos(n-1)\omega_m t - \cos(n+1)\omega_m t\right]S_{jz}\end{aligned} \tag{3.66}$$

where $|n-1| \neq 0$ $(n \neq 1)$ in the RF Hamiltonian.

The time independent Hamiltonian after employing the Floquet theory is represented by

$$H_F = H_0 + H_1 + H_2 = H_0 + H_1 + (H_{2,d} + H_{2,od}) \tag{3.67}$$

where H_1 and H_2 are the perturbation Hamiltonians coming from RF phase modulation and the MAS respectively.

$$H_0 = \omega_r I_F^{(m)} + \omega_m I_F^{(n)} + G^{(0,0)}_{H_j,Z}S_{jz} \tag{3.68}$$

$$H_1 = \sum_{j=1}^{N}\sum_{n_1=even}\left(G^{(0,n_1)}_{S_j,P}S_j^{+} + G^{(0,n_1)}_{S_j,M}S_j^{-} + G^{(0,n_1)}_{S_j,Z}S_{jz}\right) \tag{3.69}$$

$$H_{2,d} = (\omega_{I_1}^{(0)} - n\omega_r)I_{1z} + (\omega_{I_2}^{(0)} + n\omega_r)I_{2z} + G_{I_1I_2,PM}^{(0,0)} I_1^+ I_2^- + G_{I_1I_2,MP}^{(0,0)} I_1^- I_2^+ \tag{3.70}$$

$$\begin{aligned} H_{2,od}^{C-C} = & \sum_{m=-2,\neq 0}^{2} \sum_{i=1}^{2} G_{I_i}^{(m,0)} I_{iz} + \sum_{m=-2,\neq 0}^{2} G_{I_1I_2}^{(m,0)} I_{1z}I_{2z} + \\ & \sum_{m=-2,\neq 0}^{2} \left(G_{I_1I_2,PM}^{(m+2n,0)} I_1^+ I_2^- + G_{I_1I_2,MP}^{(m-2n,0)} I_1^- I_2^+ \right) \end{aligned} \tag{3.71}$$

$$H_{2,od}^{C-H} = \sum_{i=1}^{2}\sum_{j=1}^{N}\sum_{m=-2,\neq 0}^{2}\sum_{n=\pm 1} \left(G_{I_iS_j,ZZ}^{(m,n)} I_{iz}S_{jz} + G_{I_iS_j,ZP}^{(m,n)} I_{iz}S_j^+ + G_{I_iS_j,ZM}^{(m,n)} I_{iz}S_j^- \right) \tag{3.72}$$

$$H_{2,od}^{H} = \sum_{j=1}^{N}\sum_{m=-2}^{2}\sum_{n=\pm 1} \left(G_{S_j,Z}^{(m,n)} S_{jz} + G_{S_j,P}^{(m,n)} S_j^+ + G_{S_j,M}^{(m,n)} S_j^- \right) \tag{3.73}$$

$$\begin{aligned} H_{2,od}^{H-H} = & \sum_{j,k=1,j<k;}^{N}\sum_{m=-2,\neq 0}^{2}\sum_{n=0,\pm 2} \left(G_{S_jS_k,ZZ}^{(m,n)} S_{jz}S_{kz} + G_{S_jS_k,PM}^{(m,n)} S_j^+ S_k^- \right) + \\ & \sum_{j,k=1,j<k;}^{N}\sum_{m=-2,\neq 0}^{2}\sum_{n=0,\pm 2} \left(G_{S_jS_k,MP}^{(m,n)} S_j^- S_k^+ \right) + \\ & \sum_{j,k=1,j<k;}^{N}\sum_{m=-2,\neq 0}^{2}\sum_{n=0,\pm 2} \left(G_{S_jS_k,PP}^{(m,n)} S_j^+ S_k^+ + G_{S_jS_k,MM}^{(m,n)} S_j^- S_k^- \right) + \\ & \sum_{j,k=1,j<k;}^{N}\sum_{m=-2,\neq 0}^{2}\sum_{n=\pm 2} \left(G_{S_jS_k,ZP}^{(m,n)} S_{jz}S_k^+ + G_{S_jS_k,ZM}^{(m,n)} S_{jz}S_k^- \right) + \\ & \sum_{j,k=1,j<k;}^{N}\sum_{m=-2,\neq 0}^{2}\sum_{n=\pm 2} \left(G_{S_jS_k,PZ}^{(m,n)} S_j^+ S_{jz} + G_{S_jS_k,MZ}^{(m,n)} S_j^- S_{jz} \right) \end{aligned} \tag{3.74}$$

The 'G' coefficients employed in the Floquet Hamiltonian and the transformation function, S_1 are tabulated in Table 3.3 and the remaining coefficients (related to $I-I$) presented in Eq. (3.67) are similar to those defined in Tables 2.1 & 2.2 in chapter-2.

The Hamiltonian (Eq. 3.69), H_1 is a part of the Floquet Hamiltonian and their G-coefficients are derived from the time-dependent RF Hamiltonian (Eq. 3.66). The index n_1 has $\pm(n+1)$ and $\pm(n-1)$ values where $n \neq 1$ when $n_1 = |n-1|$.

Employing the contact transformation procedure, an unitary transformation defined by the transformation function, S_1 is performed to go into the RF interaction frame (Eq. 3.69).

$$\tilde{H}_F = e^{i\lambda S_1} H_F e^{-i\lambda S_1} \tag{3.75}$$

G-coefficients	
Single-spin (S)	$G^{(m,n)}_{S_j,P} = -\frac{1}{4}\frac{n}{\lvert n\rvert}\omega^{(m)}_{H_j}; G^{(m,n)}_{S_j,M} = \frac{1}{4}\frac{n}{\lvert n\rvert}\omega^{(m)}_{H_j}; G^{(m,n)}_{S_j,Z} = -\frac{1}{2}\omega^{(m)}_{H_j}; G^{(0,0)}_{S_j,Z} = \frac{2}{\pi}\sin\phi$
Two-spin $(I-S)$	$G^{(m,n)}_{I_iS_j,ZP} = -\frac{1}{2}\frac{n}{\lvert n\rvert}\omega^{(m)}_{S_j}; G^{(m,n)}_{I_iS_j,ZM} = \frac{1}{2}\frac{n}{\lvert n\rvert}\omega^{(m)}_{S_j}; G^{(m,n)}_{I_iS_j,ZPZ} = -\omega^{(m)}_{S_j}$
Two-spin $(S-S)$	$G^{(m,0)}_{S_jS_k,ZZ} = \frac{3}{2}\omega^{(m)}_{S_jS_k}; G^{(m,0)}_{S_jS_k,PM} = -\frac{5}{8}\omega^{(m)}_{S_jS_k}; G^{(m,0)}_{S_jS_k,MP} = -\frac{5}{8}\omega^{(m)}_{S_jS_k}$ $G^{(m,0)}_{S_jS_k,PP} = \frac{1}{8}\omega^{(m)}_{S_jS_k}; G^{(m,0)}_{S_jS_k,MM} = \frac{1}{8}\omega^{(m)}_{S_jS_k}$ $G^{(m,n)}_{S_jS_k,ZP} = -\frac{3}{8}\frac{n}{\lvert n\rvert}\omega^{(m)}_{S_jS_k}; G^{(m,n)}_{S_jS_k,ZM} = \frac{3}{8}\frac{n}{\lvert n\rvert}\omega^{(m)}_{S_jS_k}$ $G^{(m,n)}_{S_jS_k,PZ} = -\frac{3}{8}\frac{n}{\lvert n\rvert}\omega^{(m)}_{S_jS_k}; G^{(m,n)}_{S_jS_k,MZ} = \frac{3}{8}\frac{n}{\lvert n\rvert}\omega^{(m)}_{S_jS_k}$ $G^{(m,n)}_{S_jS_k,ZZ} = \frac{1}{4}\omega^{(m)}_{S_jS_k}; G^{(m,n)}_{S_jS_k,PM} = \frac{1}{16}\omega^{(m)}_{S_jS_k}; G^{(m,n)}_{S_jS_k,MP} = \frac{1}{16}\omega^{(m)}_{S_jS_k}$ $G^{(m,n)}_{S_jS_k,PP} = -\frac{1}{16}\omega^{(m)}_{S_jS_k}; G^{(m,n)}_{S_jS_k,MM} = -\frac{1}{16}\omega^{(m)}_{S_jS_k}$
C-coefficients	
$C^{(0,n_1)}_{S_j,P} = \frac{G^{(0,n_1)}_{S_j,P}}{n_1\omega_m - G^{(0,0)}_{H_j,Z}}; C^{(0,n_1)}_{S_j,M} = \frac{G^{(0,n_1)}_{S_j,M}}{n_1\omega_m + G^{(0,0)}_{H_j,Z}}; C^{(0,n_1)}_{S_j,Z} = \frac{G^{(0,n_1)}_{S_j,Z}}{n_1\omega_m}$	

Table 3.3: The table depicts the G-coefficients involved in the Floquet Hamiltonian (Eq. 3.67).

where the transformation function, S_1 is represented by

$$S_1 = i\sum_{j=1}^{N}\sum_{n_1=even}\left(C^{(0,n_1)}_{S_j,Z}S_{jz} + C^{(0,n_1)}_{S_j,P}S^{+}_{j} + C^{(0,n_1)}_{S_j,M}S^{-}_{j}\right) \tag{3.76}$$

The index n_1 in S_1 is same as that of H_1 and the C-coefficients are given in the Table 3.3.

Accordingly, the transformed Floquet Hamiltonian $(\tilde{H}_F)$ in the RF interaction frame is represented by,

$$\tilde{H}_F = \tilde{H}_0 + (\tilde{H}_{2,d} + \tilde{H}_{2,od}) \tag{3.77}$$

where

$$\tilde{H}_0 = \omega_r I^{(m)}_F + \omega_m I^{(n)}_F + \left(G^{(0,0)}_{H_j,Z} + R^{(0,0)}_{H_j,Z}\right)S_{jz} \tag{3.78}$$

$$\tilde{H}_{2,d} = (\omega^{(0)}_{I_1} - n\omega_r)I_{1z} + (\omega^{(0)}_{I_2} + n\omega_r)I_{2z} + G^{(0,0)}_{I_1I_2,PM}I^{+}_1I^{-}_2 + G^{(0,0)}_{I_1I_2,MP}I^{-}_1I^{+}_2 \tag{3.79}$$

$$\tilde{H}_{2,od}^{C-C} = \sum_{m=-2,\neq 0}^{2}\sum_{i=1}^{2} G_{I_i}^{(m,0)} I_{iz} + \sum_{m=-2,\neq 0}^{2} G_{I_1 I_2}^{(m,0)} I_{1z} I_{2z} + \sum_{m=-2,\neq 0}^{2} \left(G_{I_1 I_2, PM}^{(m+2n,0)} I_1^+ I_2^- + G_{I_1 I_2, MP}^{(m-2n,0)} I_1^- I_2^+ \right) \tag{3.80}$$

$$\tilde{H}_{2,od}^{C-H} = \sum_{i=1}^{2}\sum_{j=1}^{N}\sum_{m=-2,\neq 0}^{2}\sum_{n_2=-\infty,\neq 0}^{\infty,odd} \left(R_{I_i S_j, ZZ}^{(m,n_2)} I_{iz} S_{jz} + R_{I_i S_j, ZP}^{(m,n_2)} I_{iz} S_j^+ + R_{I_i S_j, ZM}^{(m,n_2)} I_{iz} S_j^- \right) \tag{3.81}$$

$$\tilde{H}_{2,od}^{H} = \sum_{j=1}^{N}\sum_{m=-2}^{2}\sum_{n_2=-\infty,\neq 0}^{\infty,odd} \left(R_{S_j, Z}^{(m,n_2)} S_{jz} + R_{S_j, P}^{(m,n_2)} S_j^+ + R_{S_j, M}^{(m,n_2)} S_j^- \right) \tag{3.82}$$

$$\begin{aligned}\tilde{H}_{2,od}^{H-H} = &\sum_{j,k=1,j<k;}^{N}\sum_{m=-2,\neq 0}^{2}\sum_{n_2=-\infty}^{\infty,even} \left(R_{S_j S_k, ZZ}^{(m,n_2)} S_{jz} S_{kz} + R_{S_j S_k, PM}^{(m,n_2)} S_j^+ S_k^- + R_{S_j S_k, MP}^{(m,n_2)} S_j^- S_k^+ \right) \\ &+ \sum_{j,k=1,j<k;}^{N}\sum_{m=-2,\neq 0}^{2}\sum_{n_2=-\infty}^{\infty,even} \left(R_{S_j S_k, PP}^{(m,n_2)} S_j^+ S_k^+ + R_{S_j S_k, MM}^{(m,n_2)} S_j^- S_k^- \right) + \\ &\sum_{j,k=1,j<k;}^{N}\sum_{m=-2,\neq 0}^{2}\sum_{n_2=-\infty}^{\infty,even} \left(R_{S_j S_k, ZP}^{(m,n_2)} S_{jz} S_k^+ + R_{S_j S_k, ZM}^{(m,n_2)} S_{jz} S_k^- \right) + \\ &\sum_{j,k=1,j<k;}^{N}\sum_{m=-2,\neq 0}^{2}\sum_{n_2=-\infty}^{\infty,even} \left(R_{S_j S_k, PZ}^{(m,n_2)} S_j^+ S_{jz} + R_{S_j S_k, MZ}^{(m,n_2)} S_j^- S_{jz} \right)\end{aligned} \tag{3.83}$$

In order to carryout the second transformation and to derive the effective Hamiltonian, the transformed Floquet Hamiltonian ($\tilde{H}_F$) is re-written as given below.

$$\begin{aligned}\tilde{H}_F =& \tilde{H}_0 + \tilde{H}_1 \\ =& \tilde{H}_0 + (\tilde{H}_{1,d} + \tilde{H}_{1,od})\end{aligned} \tag{3.84}$$

In the above equation, $\tilde{H}_{1,d} = \tilde{H}_{2,d}$ and $\tilde{H}_{1,od} = \tilde{H}_{2,od}$.

Employing the Contact transformation method again, the second transformation (S_2) was performed in order to derive the effective Hamiltonian which is diagonal in both the MAS (m) as well as the phase modulation (n) indices.

$$H_{eff} = e^{i\lambda S_2} \tilde{H}_F e^{-i\lambda S_2} \tag{3.85}$$

Here the second transformation function (S_2) was chosen to diagonalyse the off-diagonal terms ($\tilde{H}_{1,od}$) in the transformed Floquet Hamiltonian ($\tilde{H}_F$). The function,

S_2 is defined as given below.

$$\begin{aligned}
S_2 =& i\sum_{m=-2,m\neq 0}^{2}\sum_{i=1}^{2} C_{I_i}^{(m,0)} I_{iz} + i\sum_{m=-2,m\neq 0}^{2} C_{I_1I_2}^{(m,0)} I_{1z}I_{2z} + \\
& i\sum_{m=-2,m\neq 0}^{2}\left(C_{I_1I_2,PM}^{(m+2n,0)} I_1^+ I_2^- + C_{I_1I_2,MP}^{(m-2n,0)} I_1^- I_2^+\right) + \\
& i\sum_{i=1}^{2}\sum_{j=1}^{N}\sum_{m=-2,\neq 0}^{2}\sum_{n_2=-\infty,\neq 0}^{\infty,odd}\left(C_{I_iS_j,ZZ}^{(m,n_2)} I_{iz}S_{jz} + C_{I_iS_j,ZP}^{(m,n_2)} I_{iz}S_j^+ + C_{I_iS_j,ZM}^{(m,n_2)} I_{iz}S_j^-\right) + \\
& i\sum_{j=1}^{N}\sum_{m=-2,\neq 0}^{2}\sum_{n_2=-\infty,\neq 0}^{\infty,odd}\left(C_{S_j,Z}^{(m,n_2)} S_{jz} + C_{S_j,P}^{(m,n_2)} S_j^+ + C_{S_j,M}^{(m,n_2)} S_j^-\right) + \\
& i\sum_{j,k=1,j<k;}^{N}\sum_{m=-2,\neq 0}^{2}\sum_{n_2=-\infty}^{\infty,even}\left(C_{S_jS_k,ZZ}^{(m,n_2)} S_{jz}S_{kz} + C_{S_jS_k,PM}^{(m,n_2)} S_j^+ S_k^- + C_{S_jS_k,MP}^{(m,n_2)} S_j^- S_k^+\right) + \\
& i\sum_{j,k=1,j<k;}^{N}\sum_{m=-2,\neq 0}^{2}\sum_{n_2=-\infty}^{\infty,even}\left(C_{S_jS_k,PP}^{(m,n_2)} S_j^+ S_k^+ + C_{S_jS_k,MM}^{(m,n_2)} S_j^- S_k^-\right) + \\
& i\sum_{j,k=1,j<k;}^{N}\sum_{m=-2,\neq 0}^{2}\sum_{n_2=-\infty}^{\infty,even}\left(C_{S_jS_k,ZP}^{(m,n_2)} S_{jz}S_k^+ + C_{S_jS_k,ZM}^{(m,n_2)} S_{jz}S_k^-\right) + \\
& i\sum_{j,k=1,j<k;}^{N}\sum_{m=-2,\neq 0}^{2}\sum_{n_2=-\infty}^{\infty,even}\left(C_{S_jS_k,PZ}^{(m,n_2)} S_j^+ S_{jz} + C_{S_jS_k,MZ}^{(m,n_2)} S_j^- S_{jz}\right)
\end{aligned} \tag{3.86}$$

The 'R' coefficients of the Floquet Hamiltonian (Eq. 3.77 & Eq. 3.84) and the 'C' coefficients of the transformation function, S_2 (Eq. 3.86) are tabulated in Tables 3.4 and 3.5 respectively.

Following the Contact transformation procedure described in the previous chapter, the effective Hamiltonian under TPPM decoupling is derived.

$$H_{eff} = \sum_{i=1}^{2} A_{I_i} I_{iz} + \left[D_{I_1I_2,PM} I_1^+ I_2^- + D_{I_1I_2,MP} I_1^- I_2^+\right] + \sum_{i=1}^{2}\sum_{j=1}^{N} B_{I_iS_j} I_{iz}S_{jz} \tag{3.87}$$

The coefficients involved in the above effective Hamiltonian (Eq. 3.87) are given in Table 3.6.

R-coefficients	
$R^{(m,n_2)}_{S_j,Z}$	$G^{(m,\pm1)}_{S_j,Z}\left[1+2C^{(0,n_1{}')}_{S_j,P}C^{(0,n_1)}_{S_j,M}+...\right]+$ $G^{(m,\pm1)}_{S_j,P}\left[C^{(0,n_1{}')}_{S_j,M}\left\{2C^{(0,n_1)}_{S_j,P}-C^{(0,n_1)}_{S_j,Z}\right\}+\frac{1}{3}\left\{C^{(0,n_1{}'')}_{S_j,M}\left(C^{(0,n_1{}')}_{S_j,Z}C^{(0,n_1)}_{S_j,Z}+4C^{(0,n_1{}')}_{S_j,P}C^{(0,n_1)}_{S_j,M}\right)\right\}+...\right]-$ $G^{(m,\pm1)}_{S_j,M}\left[C^{(0,n_1{}')}_{S_j,P}\left\{2C^{(0,n_1)}_{S_j,M}+C^{(0,n_1)}_{S_j,Z}\right\}+\frac{1}{3}\left\{C^{(0,n_1{}'')}_{S_j,P}\left(C^{(0,n_1{}')}_{S_j,Z}C^{(0,n_1)}_{S_j,Z}+4C^{(0,n_1{}')}_{S_j,P}C^{(0,n_1)}_{S_j,M}\right)\right\}+...\right]$
$R^{(m,n_2)}_{S_j,P}$	$G^{(m,\pm1)}_{S_j,Z}\left[C^{(0,n_1)}_{S_j,P}-\frac{1}{2}C^{(0,n_1{}')}_{S_j,Z}C^{(0,n_1)}_{S_j,P}+\frac{1}{6}\left\{C^{(0,n_1{}'')}_{S_j,P}\left(4C^{(0,n_1{}')}_{S_j,P}C^{(0,n_1)}_{S_j,M}+C^{(0,n_1{}')}_{S_j,Z}C^{(0,n_1)}_{S_j,Z}\right)\right\}-...\right]+$ $G^{(m,\pm1)}_{S_j,P}\left[1-C^{(0,n_1)}_{S_j,Z}+\left\{C^{(0,n_1{}')}_{S_j,P}C^{(0,n_1)}_{S_j,M}+\frac{1}{2}C^{(0,n_1{}')}_{S_j,Z}C^{(0,n_1)}_{S_j,Z}\right\}-\frac{1}{6}\left\{C^{(0,n_1{}'')}_{S_j,Z}\left(C^{(0,n_1{}')}_{S_j,Z}C^{(0,n_1)}_{S_j,Z}+4C^{(0,n_1{}')}_{S_j,P}C^{(0,n_1)}_{S_j,M}\right)\right\}+...\right]+$ $G^{(m,\pm1)}_{S_j,M}\left[-C^{(0,n_1{}')}_{S_j,P}C^{(0,n_1)}_{S_j,P}+...\right]$
$R^{(m,n_2)}_{S_j,M}$	$G^{(m,\pm1)}_{S_j,Z}\left[-C^{(0,n_1)}_{S_j,M}-\frac{1}{2}C^{(0,n_1{}')}_{S_j,Z}C^{(0,n_1)}_{S_j,M}-\frac{1}{6}\left\{C^{(0,n_1{}'')}_{S_j,M}\left(4C^{(0,n_1{}')}_{S_j,P}C^{(0,n_1)}_{S_j,M}+C^{(0,n_1{}')}_{S_j,Z}C^{(0,n_1)}_{S_j,Z}\right)\right\}-...\right]+$ $G^{(m,\pm1)}_{S_j,P}\left[-C^{(0,n_1{}')}_{S_j,M}C^{(0,n_1)}_{S_j,M}+...\right]+$ $G^{(m,\pm1)}_{S_j,M}\left[1+C^{(0,n_1)}_{S_j,Z}+\left\{C^{(0,n_1{}')}_{S_j,P}C^{(0,n_1)}_{S_j,M}+\frac{1}{2}C^{(0,n_1{}')}_{S_j,Z}C^{(0,n_1)}_{S_j,Z}\right\}+\frac{1}{6}\left\{C^{(0,n_1{}'')}_{S_j,Z}\left(C^{(0,n_1{}')}_{S_j,Z}C^{(0,n_1)}_{S_j,Z}+4C^{(0,n_1{}')}_{S_j,P}C^{(0,n_1)}_{S_j,M}\right)\right\}+...\right]$
$R^{(m,n_2)}_{I_iS_j,ZZ}$	$G^{(m,\pm1)}_{I_iS_j,ZZ}\left[1+2C^{(0,n_1{}')}_{S_j,P}C^{(0,n_1)}_{S_j,M}+...\right]+$ $G^{(m,\pm1)}_{I_iS_j,ZP}\left[C^{(0,n_1{}')}_{S_j,M}\left\{2C^{(0,n_1)}_{S_j,P}-C^{(0,n_1)}_{S_j,Z}\right\}+\frac{1}{3}\left\{C^{(0,n_1{}'')}_{S_j,M}\left(C^{(0,n_1{}')}_{S_j,Z}C^{(0,n_1)}_{S_j,Z}+4C^{(0,n_1{}')}_{S_j,P}C^{(0,n_1)}_{S_j,M}\right)\right\}+...\right]-$ $G^{(m,\pm1)}_{I_iS_j,ZM}\left[C^{(0,n_1{}')}_{S_j,P}\left\{2C^{(0,n_1)}_{S_j,M}+C^{(0,n_1)}_{S_j,Z}\right\}+\frac{1}{3}\left\{C^{(0,n_1{}'')}_{S_j,P}\left(C^{(0,n_1{}')}_{S_j,Z}C^{(0,n_1)}_{S_j,Z}+4C^{(0,n_1{}')}_{S_j,P}C^{(0,n_1)}_{S_j,M}\right)\right\}+...\right]$
$R^{(m,n_2)}_{I_iS_j,ZP}$	$G^{(m,\pm1)}_{I_iS_j,ZZ}\left[C^{(0,n_1)}_{S_j,P}-\frac{1}{2}C^{(0,n_1{}')}_{S_j,Z}C^{(0,n_1)}_{S_j,P}+\frac{1}{6}\left\{C^{(0,n_1{}'')}_{S_j,P}\left(4C^{(0,n_1{}')}_{S_j,P}C^{(0,n_1)}_{S_j,M}+C^{(0,n_1{}')}_{S_j,Z}C^{(0,n_1)}_{S_j,Z}\right)\right\}-...\right]+$ $G^{(m,\pm1)}_{I_iS_j,ZP}\left[1-C^{(0,n_1)}_{S_j,Z}+\left\{C^{(0,n_1{}')}_{S_j,P}C^{(0,n_1)}_{S_j,M}+\frac{1}{2}C^{(0,n_1{}')}_{S_j,Z}C^{(0,n_1)}_{S_j,Z}\right\}-\frac{1}{6}\left\{C^{(0,n_1{}'')}_{S_j,Z}\left(C^{(0,n_1{}')}_{S_j,Z}C^{(0,n_1)}_{S_j,Z}+4C^{(0,n_1{}')}_{S_j,P}C^{(0,n_1)}_{S_j,M}\right)\right\}+...\right]+$ $G^{(m,\pm1)}_{I_iS_j,ZM}\left[-C^{(0,n_1{}')}_{S_j,P}C^{(0,n_1)}_{S_j,P}+...\right]$
$R^{(m,n_2)}_{I_iS_j,ZM}$	$G^{(m,\pm1)}_{I_iS_j,ZZ}\left[-C^{(0,n_1)}_{S_j,M}-\frac{1}{2}C^{(0,n_1{}')}_{S_j,Z}C^{(0,n_1)}_{S_j,M}-\frac{1}{6}\left\{C^{(0,n_1{}'')}_{S_j,M}\left(4C^{(0,n_1{}')}_{S_j,P}C^{(0,n_1)}_{S_j,M}+C^{(0,n_1{}')}_{S_j,Z}C^{(0,n_1)}_{S_j,Z}\right)\right\}-...\right]+$ $G^{(m,\pm1)}_{I_iS_j,ZP}\left[-C^{(0,n_1{}')}_{S_j,M}C^{(0,n_1)}_{S_j,M}+...\right]+$ $G^{(m,\pm1)}_{I_iS_j,ZM}\left[1+C^{(0,n_1)}_{S_j,Z}+\left\{C^{(0,n_1{}')}_{S_j,P}C^{(0,n_1)}_{S_j,M}+\frac{1}{2}C^{(0,n_1{}')}_{S_j,Z}C^{(0,n_1)}_{S_j,Z}\right\}+\frac{1}{6}\left\{C^{(0,n_1{}'')}_{S_j,Z}\left(C^{(0,n_1{}')}_{S_j,Z}C^{(0,n_1)}_{S_j,Z}+4C^{(0,n_1{}')}_{S_j,P}C^{(0,n_1)}_{S_j,M}\right)\right\}+...\right]$

Table 3.4: The table depicts the R-coefficients involved in the Floquet Hamiltonian (Eqs. 3.77 & 3.84).

C-coefficients	
$C^{(m,n_2)}_{S_j,Z} = \frac{R^{(m,n_2)}_{S_j,Z}}{m\omega_r+n_2\omega_m}$	$C^{(m,n_2)}_{I_iS_j,ZZ} = \frac{R^{(m,n_2)}_{I_iS_j,ZZ}}{m\omega_r+n_2\omega_m}$
$C^{(m,n_2)}_{S_j,P} = \frac{R^{(m,n_2)}_{S_j,P}}{m\omega_r+n_2\omega_m-\left(G^{(0,0)}_{H_j,Z}+R^{(0,0)}_{H_j,Z}\right)}$	$C^{(m,n_2)}_{I_iS_j,ZP} = \frac{R^{(m,n_2)}_{I_iS_j,ZP}}{m\omega_r+n_2\omega_m-\left(G^{(0,0)}_{H_j,Z}+R^{(0,0)}_{H_j,Z}\right)}$
$C^{(m,n_2)}_{S_j,M} = \frac{R^{(m,n_2)}_{S_j,M}}{m\omega_r+n_2\omega_m+\left(G^{(0,0)}_{H_j,Z}+R^{(0,0)}_{H_j,Z}\right)}$	$C^{(m,n_2)}_{I_iS_j,ZM} = \frac{R^{(m,n_2)}_{I_iS_j,ZM}}{m\omega_r+n_2\omega_m+\left(G^{(0,0)}_{H_j,Z}+R^{(0,0)}_{H_j,Z}\right)}$

Table 3.5: The table depicts the R-coefficients involved in the second transformation function, S_2 (Eq. 3.86).

Coefficients	First - order	Second - order
$B_{I_iS_j}$	0	$\frac{1}{2}\left(C^{(m,n_2)}_{S_j,P}R^{(-m,-n_2)}_{I_iS_j,ZM} - C^{(m,n_2)}_{I_iS_j,ZM}R^{(-m,-n_2)}_{S_j,P}\right) -$ $\frac{1}{2}\left(C^{(m,n_2)}_{S_j,M}R^{(-m,-n_2)}_{I_iS_j,ZP} - C^{(m,n_2)}_{I_iS_j,ZP}R^{(-m,-n_2)}_{S_j,M}\right)$ } CSA (^1H) × Dipolar $(^{13}C{-}^1H)$

Table 3.6: This table depicts the heteronuclear dipolar coefficients ($B_{I_iS_j}$) involved in the effective Hamiltonian (Eq. 3.87). See Table 2.3 in chapter-2 for all the remaining A-coefficients.

References

[1] R. Ramachandran, V. Ladizhansky, V. S. Bajaj, and R. G. Griffin, *J. Am. Chem. Soc.*, 2003, **125**, 15623–15629.

[2] R. Ramachandran, J. R. Lewandowski, P. C. A. van der Wel and R. G. Griffin, *J. Chem. Phys.*, 2006, **124**, 214107.

[3] R. Janik, X. Peng and V. Ladizhansky, *J. Magn. Reson.*, 2007, **188**, 129 – 140.

[4] P. C. A. van der Wel, M. T. Eddy, R. Ramachandran and R. G. Griffin, *ChemPhysChem*, 2009, **10**, 1656–1663.

[5] M. H. Levitt, D. P. Raleigh, F. Creuzet and R. G. Griffin, *J. Chem. Phys.*, 1990, **92**, 6347–6364.

[6] P. R. Costa, B. Sun and R. G. Griffin, *J. Magn. Reson.*, 2003, **164**, 92 – 103.

[7] M. Mehring, *Principles of High Resolution NMR in Solids*, (Springer, Berlin, 1983), 2nd edn.

[8] U. Haeberlen, *High Resolution NMR in Solids: Selective Averaging*, (Academic Press, New York, 1976).

[9] K. Schmidt-Rohr and H. W. Spiess, *Multidimensional Solid- State NMR and Polymers*, (Academic Press, London, 1994).

[10] P. Tekely, P. Palmas and D. Canet, *J. Magn. Reson. A*, 1994, **107**, 129 – 133.

[11] A. E. Bennett, C. M. Rienstra, M. Auger, K. V. Lakshmi and R. G. Griffin, *J. Chem. Phys.*, 1995, **103**, 6951–6958.

[12] Z. Gan and R. Ernst, *Solid State Nucl. Magn. Reson.*, 1997, **8**, 153 – 159.

[13] Y. Yu and B. Fung, *J. Magn. Reson.*, 1998, **130**, 317 – 320.

[14] M. Edén and M. H. Levitt, *J. Chem. Phys.*, 1999, **111**, 1511–1519.

[15] M. Carravetta, M. Edén, X. Zhao, A. Brinkmann and M. H. Levitt, *Chem. Phys. Lett.*, 2000, **321**, 205 – 215.

[16] B. Fung, A. Khitrin and K. Ermolaev, *J. Magn. Reson.*, 2000, **142**, 97 – 101.

[17] K. Takegoshi, J. Mizokami and T. Terao, *Chem. Phys. Lett.*, 2001, **341**, 540 – 544.

[18] A. Detken, E. H. Hardy, M. Ernst and B. H. Meier, *Chem. Phys. Lett.*, 2002, **356**, 298 – 304.

[19] A. Khitrin, T. Fujiwara and H. Akutsu, *J. Magn. Reson.*, 2003, **162**, 46 – 53.

[20] G. De Paëpe, A. Lesage and L. Emsley, *J. Chem. Phys.*, 2003, **119**, 4833–4841.

[21] G. D. Paëpe, D. Sakellariou, P. Hodgkinson, S. Hediger and L. Emsley, *Chem. Phys. Lett.*, 2003, **368**, 511 – 522.

[22] G. De Paëpe, B. Eléna and L. Emsley, *J. Chem. Phys.*, 2004, **121**, 3165–3180.

[23] R. Ramachandran, V. S. Bajaj and R. G. Griffin, *J. Chem. Phys.*, 2005, **122**, 164503.

[24] R. S. Thakur, N. D. Kurur and P. Madhu, *Chem. Phys. Lett.*, 2006, **426**, 459 – 463.

[25] I. Scholz, P. Hodgkinson, B. H. Meier and M. Ernst, *J. Chem. Phys.*, 2009, **130**, 114510.

[26] J. M. Vinther, A. B. Nielsen, M. Bjerring, E. R. H. van Eck, A. P. M. Kentgens, N. Khaneja and N. C. Nielsen, *J. Chem. Phys.*, 2012, **137**, 214202.

[27] M. Veshtort and R. G. Griffin, *Journal of Magnetic Resonance*, 2006, **178**, 248.

[28] L. Sonnenberg, S. Luca and M. Baldus, *J. Magn. Reson.*, 2004, **166**, 100 – 110.

[29] R. J. G. H. Xiaohu Peng, David Libich and V. Ladizhansky, *J. Am. Chem. Soc.*, 2008, **130**, 359–369.

Chapter 4

Description of higher-order and fractional R^2 experiments

4.1 Background

The next stage in our study was to explore the possibility altering the resonance conditions in R^2 experiments. In the first-order based R^2 experiments (N=1, 2), the resonance conditions are highly dependent on the isotropic chemical shift differences between nuclei. Such stringent conditions are detrimental in cases where the chemical shift separation is much smaller than the CSA interactions. To address this issue, experiments such as Rotational Resonance in the tilted rotating frame[1] (R^2TR) were conceived in the past. In contrast to the conventional R^2 experiments, a weak RF field (to preserve the selectivity) was employed in the R^2TR experiments to facilitate polarization transfer under modified resonance conditions. In addition to zero-quantum (ZQ) matching conditions, new matching conditions corresponding to single-quantum and double-quantum were identified in such experiments. Due to lower scaling factors, the R^2TR experiments were of limited utility in the estimation of $^{13}C - {}^{13}C$ distances in uniformly labeled solids. In a contrasting attempt, experiments such as DARR[2] (Dipolar Assisted Rotational Resonance) were proposed to broaden the matching conditions in R^2 experiments. To facilitate broadband transfer of polarization, the amplitude of the CW fields employed in such experiments were chosen to be integer multiples of the sample spinning frequency. Although, the DARR experiments have found extensive applications in multi-dimensional spectral

assignment studies, their extension in the estimation of $^{13}C - ^{13}C$ distances was limited due to the presence of multiple-spin interactions in the exchange dynamics. As an alternative, the possibility of employing multiple-pulse sequences is discussed in this chapter. The motivation for the present study stems from the multiple-pulse experiments[3,4] of Griffin and coworkers[5] in 1994. In their experiment, the stringent conditions on the sample spinning frequency (imposed by the chemical shift difference in R^2 experiment) were modified through periodic multiple-pulse sequences. By careful choice of the RF amplitudes, flip angles and the cycle time of the pulse sequence, modified resonance conditions (hereby referred to as 'fractional resonance' conditions) were proposed with chemical shift selectivity. To minimize the effects of sample spinning during the multiple pulse sequence, the cycle time of the sequence was deliberately chosen shorter than that of the MAS rotor period. The feasibility and practical implementation of such schemes would be described in this section.

4.2 Definition of the problem

To develop a general framework for describing multiple-pulse based rotational resonance experiments in solid-state MAS experiments. Employing the concept of effective Hamiltonians, the optimal conditions (that includes the choice of the spinning frequency, modulation frequency, flip angles of the pulses) that are required for the implementation of such schemes would be discussed.

4.3 Theory

4.3.1 Higher-order Rotational resonance (N=3, 4)

To describe the magnetization exchange between ^{13}C nuclei under higher-order R^2 conditions (N>2), we begin our discussion with a model system comprising of two-spins (I_1 and I_2). In contrast to the N=1& 2, R^2 experiments, the dipolar interactions are averaged out to first-order in higher-order R^2 experiments. Following the general procedure[6–14] described in chapter-2, the Floquet Hamiltonian is derived and is re-expressed as illustrated.

$$H_F = H_0 + H_1 = H_0 + (H_{1,d} + H_{1,od}) \tag{4.1}$$

$$H_0 = \omega_r I_F \tag{4.2}$$

$$H_{1,d} = (\omega_1^{(0)} - n\omega_r)[I_{1z}]_0 + (\omega_2^{(0)} + n\omega_r)[I_{2z}]_0 \tag{4.3}$$

$$\begin{aligned} H_{1,od} = & \sum_{m=-2,m\neq 0}^{2} \sum_{i=1}^{2} G_{I_i}^{(m)} [I_{iz}]_m + \sum_{m=-2,m\neq 0}^{2} G_{I_1 I_2}^{(m)} [I_{1z} I_{2z}]_m + \\ & \sum_{m=-2,m\neq 0}^{2} \left(G_{I_1 I_2, PM}^{(m+2n)} \left[I_1^+ I_2^- \right]_{m+2n} + G_{I_1 I_2, MP}^{(m-2n)} \left[I_1^- I_2^+ \right]_{m-2n} \right) \end{aligned} \tag{4.4}$$

In the above equation, for the N=3 & 4 matching conditions (i.e. $\omega_1 - \omega_2 = N\omega_r$), the corresponding 'n' values are 3/2, 2 respectively. The diagonal part of the Hamiltonian comprises of only single-spin longitudinal operators. Employing the transformation function, S_1, the off-diagonal part of the Hamiltonian is folded through the standard procedure described in the previous chapters.

$$\begin{aligned} S_1 = & \sum_{m=-2,m\neq 0}^{2} i \left\{ \sum_{i=1}^{2} C_{I_i}^{(m)} [I_{iz}]_m + C_{I_1 I_2}^{(m)} [I_{1z} I_{2z}]_m \right\} + \\ & \sum_{m=-2,m\neq 0}^{2} i \left\{ C_{I_1 I_2, PM}^{(m+2n)} \left[I_1^+ I_2^- \right]_{m+2n} + C_{I_1 I_2, MP}^{(m-2n)} \left[I_1^- I_2^+ \right]_{m-2n} \right\} \end{aligned} \tag{4.5}$$

The form of the 'G' and 'C' coefficients present in the Floquet Hamiltonian and the transformation function, S_1 are tabulated in Tables 4.1 and 4.2.

Accordingly, the effective Hamiltonian[15,16] to second order are evaluated through the higher-order expressions /terms in the contact transformation procedure[17,18].

$$\begin{aligned} H_{eff} &= H_0^{(1)} + H_1^{(1)} + H_2^{(1)} \\ H_1^{(1)} &= H_{1,d} \\ H_2^{(1)} &= \frac{i}{2} [S_1, H_1] \end{aligned} \tag{4.6}$$

Analogous to our earlier description, the effective Hamiltonian comprises of single-spin and two-spin operators.

$$H_{eff} = \sum_{i=1}^{2} A_{I_i} I_{iz} + \left[D_{I_1 I_2, PM} I_1^+ I_2^- + D_{I_1 I_2, MP} I_1^- I_2^+ \right] \tag{4.7}$$

In contrast to first-order based R^2 experiments (N=1, 2), the two-spin operators in the effective Hamiltonian result from second-order cross-terms between the CSA (of carbons) and the dipolar interactions. When the chemical shift difference between the spins is equal to $3\omega_r$ (i.e. $\omega_1 - \omega_2 = 2n\omega_r = N\omega_r$; for n=3/2 or N=3), both the m=1, 2 components of the CSA and dipolar interactions play an important role in

G-coefficients	
$G^{(m)}_{I_i} = \omega^{(m)}_{I_i}$	$G^{(m)}_{I_1I_2} = 2\omega^{(m)}_{I_1I_2}$
$G^{(5)}_{I_1I_2,PM} = -\frac{1}{2}\omega^{(2)}_{I_1I_2}$	$G^{(4)}_{I_1I_2,PM} = -\frac{1}{2}\omega^{(1)}_{I_1I_2}$
$G^{(1)}_{I_1I_2,PM} = -\frac{1}{2}\omega^{(-2)}_{I_1I_2}$	$G^{(2)}_{I_1I_2,PM} = -\frac{1}{2}\omega^{(-1)}_{I_1I_2}$
$G^{(-1)}_{I_1I_2,MP} = -\frac{1}{2}\omega^{(2)}_{I_1I_2}$	$G^{(-2)}_{I_1I_2,MP} = -\frac{1}{2}\omega^{(1)}_{I_1I_2}$
$G^{(-5)}_{I_1I_2,MP} = -\frac{1}{2}\omega^{(-2)}_{I_1I_2}$	$G^{(-4)}_{I_1I_2,MP} = -\frac{1}{2}\omega^{(-1)}_{I_1I_2}$
C-coefficients	
$C^{(m)}_{I_i} = \frac{G^{(m)}_{I_i}}{m\omega_r}$	$C^{(m)}_{I_1I_2} = \frac{G^{(m)}_{I_1I_2}}{m\omega_r}$
$C^{(m)}_{I_1I_2,PM} = \frac{G^{(m)}_{I_1I_2,PM}}{m\omega_r}$	$C^{(m)}_{I_1I_2,MP} = \frac{G^{(m)}_{12,MP}}{m\omega_r}$

Table 4.1: The table depicts the G and C-coefficients involved in the Floquet Hamiltonian and the transformation function, S_1, for N=3, R^2 condition

G-coefficients	
$G^{(m)}_{I_i} = \omega^{(m)}_{I_i}$	$G^{(m)}_{I_1I_2} = 2\omega^{(m)}_{I_1I_2}$
$G^{(6)}_{I_1I_2,PM} = -\frac{1}{2}\omega^{(2)}_{I_1I_2}$	$G^{(5)}_{I_1I_2,PM} = -\frac{1}{2}\omega^{(1)}_{I_1I_2}$
$G^{(2)}_{I_1I_2,PM} = -\frac{1}{2}\omega^{(-2)}_{I_1I_2}$	$G^{(3)}_{I_1I_2,PM} = -\frac{1}{2}\omega^{(-1)}_{I_1I_2}$
$G^{(-2)}_{I_1I_2,MP} = -\frac{1}{2}\omega^{(2)}_{I_1I_2}$	$G^{(-3)}_{I_1I_2,MP} = -\frac{1}{2}\omega^{(1)}_{I_1I_2}$
$G^{(-6)}_{I_1I_2,MP} = -\frac{1}{2}\omega^{(-2)}_{I_1I_2}$	$G^{(-5)}_{I_1I_2,MP} = -\frac{1}{2}\omega^{(-1)}_{I_1I_2}$
C-coefficients	
$C^{(m)}_{I_i} = \frac{G^{(m)}_{I_i}}{m\omega_r}$	$C^{(m)}_{I_1I_2} = \frac{G^{(m)}_{I_1I_2}}{m\omega_r}$
$C^{(m)}_{I_1I_2,PM} = \frac{G^{(m)}_{I_1I_2,PM}}{m\omega_r}$	$C^{(m)}_{I_1I_2,MP} = \frac{G^{(m)}_{I_1I_2,MP}}{m\omega_r}$

Table 4.2: The table depicts the G and C-coefficients involved in the Floquet Hamiltonian and the transformation function, S_1, for N=4, R^2 condition

the reintroduction of the dipolar interactions. In a similar vein, when the chemical shift difference equals to $4\omega_r$ (i.e. $\omega_1 - \omega_2 = 2n\omega_r = N\omega_r$; for n=2 or N=4), the cross-terms between the $m = \pm 2$ component of the CSA and the $m = \pm 2$ component of the dipolar interactions are responsible for the two-spin operators in the effective Hamiltonian. Hence, the CSA interactions play an important role in the higher-order (integer) resonance conditions.

The coefficients contained in the effective Hamiltonian (Eq. 4.7) are listed in Table 4.3. Employing the reduced density matrix theory, the polarization transfer from spin I_1 to I_2 is described through the equations illustrated in chapter-3. The higher-order R^2 conditions described in this section rely on the CSA interactions. As an alternative, the possibility of higher-order R^2 matching conditions through multiple pulses will be discussed in the following section.

Coefficients	First - order	Second - order
A_{I_1}	$\left(\omega_{I_1}^{(0)} - n\omega_r\right)$	$\underbrace{\frac{1}{2}\left(C_{I_1I_2,PM}^{(m)}G_{I_1I_2,MP}^{(-m)} - C_{I_1I_2,MP}^{(m)}G_{I_1I_2,PM}^{(-m)}\right) + \frac{1}{2}\left(C_{I_1I_3,PM}^{(m)}G_{I_1I_3,MP}^{(-m)} - C_{I_1I_3,MP}^{(m)}G_{I_1I_3,PM}^{(-m)}\right)}_{\mathrm{Dipolar}(^{13}C-^{13}C)\times\mathrm{Dipolar}(^{13}C-^{13}C)}$
A_{I_2}	$\left(\omega_{I_2}^{(0)} + n\omega_r\right)$	$\underbrace{-\frac{1}{2}\left(C_{I_1I_2,PM}^{(m)}G_{I_1I_2,MP}^{(-m)} - C_{I_1I_2,MP}^{(m)}G_{I_1I_2,PM}^{(-m)}\right)}_{\mathrm{Dipolar}(^{13}C-^{13}C)\times\mathrm{Dipolar}(^{13}C-^{13}C)}$
$D_{I_1I_2,PM}$	0	$\underbrace{\frac{1}{2}\left(C_{I_1}^{(m)}G_{I_1I_2,PM}^{(-m)} - C_{I_1I_2,PM}^{(m)}G_{I_1}^{(-m)}\right) - \frac{1}{2}\left(C_{I_2}^{(m)}G_{I_1I_2,PM}^{(-m)} - C_{I_1I_2,PM}^{(m)}G_{I_2}^{(-m)}\right)}_{\mathrm{CSA}(^{13}C)\times\mathrm{Dipolar}(^{13}C-^{13}C)}$
$D_{I_1I_2,MP}$	0	$\underbrace{-\frac{1}{2}\left(C_{I_1}^{(m)}G_{I_1I_2,MP}^{(-m)} - C_{I_1I_2,MP}^{(m)}G_{I_1}^{(-m)}\right) + \frac{1}{2}\left(C_{I_2}^{(m)}G_{I_1I_2,MP}^{(-m)} - C_{I_1I_2,MP}^{(m)}G_{I_2}^{(-m)}\right)}_{\mathrm{CSA}(^{13}C)\times\mathrm{Dipolar}(^{13}C-^{13}C)}$

Table 4.3: This table depicts the first-order and second-order corrections for N=3 and N=4, R^2 conditions involved in the Eq. (4.7). For all the 'G' and 'C' coefficients and the Fourier indices (m) in the above table, see the Tables 4.1 & 4.2 for N=3 and N=4, R^2 conditions, respectively.

4.3.2 Fractional Rotational resonance

To derive alternate matching conditions, multiple pulse schemes were employed to interfere with the rotor induced magnetization exchange. The feasibility of such schemes (see Fig. 4.1) is discussed below in this section.

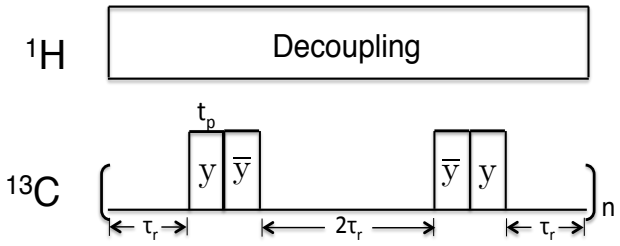

Figure 4.1: The figure depicts the pulse sequence employed for the implementation of fractional R^2 experiments. The sequence involves four pulses of flip angle $\beta = \omega_1 t_p$ and opposite phases with a total cycle time, $\tau_m = 4\tau_r + 4t_p$.

To begin with, the Hamiltonian for an isolated spin pair in the presence of a periodic multiple-pulse scheme is depicted by,

$$H(t) = \sum_{m=-2,m\neq 0}^{2} \sum_{i=1}^{2} \left[\omega_i^{(0)} + \omega_i^{(m)} e^{im\omega_r t}\right] I_{iz} + \sum_{m=-2,m\neq 0}^{2} \omega_{12}^{(m)} e^{im\omega_r t} \left[2I_{1z}I_{2z} - (I_{1x}I_{2x} + I_{1y}I_{2y})\right] + H_{RF}(t) \tag{4.8}$$

In the above equation, $H_{RF}(t)$ represents the Fourier series expansion of the multiple-pulse sequence depicted in Fig. (4.1). For the pulse sequence depicted in Figure 4.1, the Fourier series expansion is depicted below.

$$H_{RF}(\mathrm{t}) = \frac{8\omega_{RF}}{\pi} \sum_{n=1,3,5..} (i)^{n+1} \frac{1}{n} \sin^2\left(\frac{n\omega_m t_p}{2}\right) \cos(n\omega_m t) \left[I_{1y} + I_{2y}\right] \tag{4.9}$$

In the above equation, 't_p' represents the duration of the pulse, ω_{RF} is the amplitude and ω_m, the modulation frequency of the multiple-pulse sequence ($\omega_m = \frac{2\pi}{\tau_m}$, where $\tau_m = 4\tau_r + 4t_p$, is the cycle time of the pulse sequence). In contrast to the description presented in the previous section, the presence of a multiple-pulse sequence alters both the resonance condition and the behavior of the spin system. Consequently, the evolution of the system is governed by an effective Hamiltonian that is different from the internal Hamiltonian of the system. From an experimental perspective, the form of this effective Hamiltonian could be tailored by the appropriate choice of the spinning frequency, RF amplitude, duration of the pulse and the cycle time of the experiment. In this section, we present an analytic approach to deduce the matching conditions through effective Hamiltonians.

To describe the effects of the multiple-pulse scheme on the internal spin interactions, the Hamiltonian in the rotating frame is transformed into an interaction frame

defined by the RF interaction. In the past, Average Hamiltonian theory (AHT)[19–21] was employed to describe the spin dynamics under certain conditions. To facilitate analytic description, the cycle time (τ_m) of the pulse sequence is often synchronized with the MAS rotor period, τ_r. As an alternative, a more general framework (without synchronization conditions) based on Floquet theory[6–14] is presented in this section. In the Floquet framework, the time-dependent Hamiltonian is recast into a time-independent Hamiltonian, as represented below.

$$\begin{aligned} H_F =& \omega_r I_{F_1} + \omega_m I_{F_2} + \omega_1^{(0)}[I_{1z}]_{0,0} + \omega_2^{(0)}[I_{2z}]_{0,0} + \\ & \sum_{m=-2,m\neq 0}^{2} G_1^{(m)}[I_{1z}]_{m,0} + \sum_{m=-2,m\neq 0}^{2} G_2^{(m)}[I_{2z}]_{m,0} + \\ & \sum_{m=-2,m\neq 0}^{2} \left\{ G_{ZZ}^{(m)}[I_{1z}I_{2z}]_{m,0} + G_{XX}^{(m)}[I_{1x}I_{2x}]_{m,0} + G_{YY}^{(m)}[I_{1y}I_{2y}]_{m,0} \right\} + \\ & \sum_{n=\pm 1,\pm 3,\pm 5..}^{\infty} G_{RF}^{(n)} \left\{ [I_{1y}]_{0,n} + [I_{2y}]_{0,n} \right\} \end{aligned} \tag{4.10}$$

The Fourier indices, 'm, n' in the above Floquet Hamiltonian are representative of the modulations imposed by MAS and multiple pulses, respectively.

To illustrate the effects of the RF modulation on the internal Hamiltonians, the RF Hamiltonian in the Floquet framework is transformed using the transformation function, S_1. The procedure described below is the Floquet equivalent of the RF interaction frame transformation in NMR spectroscopy. To realize this, the Floquet Hamiltonian represented in Eq. (4.10) is re-expressed as a sum of two terms.

$$H_F = H_F^{\text{int}} + H_F^{RF} \tag{4.11}$$

The effective RF Hamiltonian is derived by re-expressing the H_F^{RF} in terms of a zero-order (H_0^{RF}) and perturbing Hamiltonians (H_1^{RF}) as illustrated below.

$$\begin{aligned} H_F^{RF} =& H_0^{RF} + H_1^{RF} \\ H_0^{RF} =& \omega_m I_{F_2} \\ H_1^{RF} =& \sum_{n=\pm 1,\pm 3,\pm 5..}^{\infty} G_{RF}^{(n)} \left\{ [I_{1y}]_{0,n} + [I_{2y}]_{0,n} \right\} \end{aligned} \tag{4.12}$$

To compensate the off-diagonality in H_1^{RF}, a suitable transformation function in the form of S_1 is employed.

$$S_1 = i \sum_{n=\pm 1,\pm 3,\pm 5..}^{\infty} C_{RF}^{(n)} \left\{ [I_{1y}]_{0,n} + [I_{2y}]_{0,n} \right\} \tag{4.13}$$

where $C_{RF}^{(n)} = \frac{G_{RF}^{(n)}}{n\omega_m}$.

The effective RF Hamiltonian is obtained by transforming the untransformed Floquet Hamiltonian, as illustrated below.

$$H_{F,eff}^{RF} = e^{i\lambda S_1} H_F^{RF} e^{-i\lambda S_1} \tag{4.14}$$

In this framework, the effective Hamiltonian describing the RF interaction reduces to a much simpler from, $H_{F,eff}^{RF} = \omega_m I_F^{(n)}$.

To describe the effects of the multiple-pulse scheme, the internal Floquet Hamiltonian (H_{int}^F) is transformed by S_1.

$$\tilde{H}_F^{\text{int}} = e^{i\lambda S_1} H_F^{\text{int}} e^{-i\lambda S_1} \tag{4.15}$$

In the RF interaction frame, the internal Hamiltonians are modulated by both MAS and the modulation frequency (ω_m) imposed by the multiple pulse scheme. Consequently, the internal Floquet Hamiltonian in the RF interaction frame is labeled through indices 'm,n' (representative of the ω_r and ω_m modulations). For illustrative purposes, the derivation of the internal Floquet Hamiltonians in the RF interaction frame is described below.

i. Isotropic chemical shift:

In the RF interaction frame, the isotropic part of the chemical shift acquires time-dependence due to the multiple pulse scheme. The unmodulated part of the chemical shift interaction is represented through the $[I_z]_0$ operator, while the modulated part is represented by $[I_z]_{0,n}$ & $[I_x]_{0,n}$ operators.

$$H_{F,iso} = \omega_1^{(0)}[I_{1z}]_0 + \omega_2^{(0)}[I_{2z}]_0 \tag{4.16}$$

$$\begin{aligned}\tilde{H}_{F,iso} =& e^{i\lambda S_1} H_{F,iso} e^{-i\lambda S_1} \\ =& H_{F,iso} + i\lambda\left[S_1, H_{F,iso}\right] + \frac{(i\lambda)^2}{2!}\left[S_1\left[S_1, H_{F,iso}\right]\right] + ...\end{aligned} \tag{4.17}$$

The unmodulated part of the isotropic chemical shift interaction is scaled by the multiple-pulse sequence with the scaling factor derived by evaluating the even terms in Eq. (4.17).

$$[I_z]_{0,0}\left\{1 + \frac{(i\lambda)^2}{2!}C_{RF}^{n_1}C_{RF}^{n_2} + \frac{(i\lambda)^4}{4!}C_{RF}^{n_1}C_{RF}^{n_2}C_{RF}^{n_3}C_{RF}^{n_4} + ...\right\} \tag{4.18}$$

The coefficients are chosen such that the conditions $n_1 + n_2 = 0$ and $n_1 + n_2 + n_3 + n_4 = 0$ (with $n_i = \pm 1, \pm 3, \pm 5..$) are satisfied. In addition to the $[I_z]_{0,0}$ operator, additional operators in the form $[I_z]_{0,n'}$ (where $n_i = \pm 2, \pm 3..$) do exist and become operationally valid depending on their scaling factors.

In a similar vein, transverse components of the chemical shift interaction are derived by evaluating the odd-terms present in Eq. (4.17).

$$[I_x]_{0,n'} \left\{ (i\lambda) [S_1, [I_z]_0] + \frac{(i\lambda)^3}{3!} [S_1 [S_1 [S_1, [I_z]_0]]] + ... \right\} \tag{4.19}$$

The description presented above is equally valid for the chemical shift anisotropic (CSA) interactions. In addition to the MAS modulation, the CSA interactions in the RF interaction frame are modulated by the RF-pulses and are represented through $[I_z]_{m,0}$, $[I_z]_{m,n'}$ and $[I_x]_{m,n''}$ operators. The coefficients corresponding to these operators are derived systematically from Eq. (4.17). The final form of the chemical shift interaction in the RF interaction frame along with scaling factors is represented below.

$$\begin{aligned} \tilde{H}_{F,iso} =& k\omega_1^{(0)}[I_{1z}]_{0,0} + k_1^{n'}\omega_1^{(0)}[I_{1z}]_{0,n'} + k_2^{n''}\omega_1^{(0)}[I_{1x}]_{0,n''} + \\ & k\omega_2^{(0)}[I_{2z}]_{0,0} + k_1^{n'}\omega_2^{(0)}[I_{2z}]_{0,n'} + k_2^{n''}\omega_2^{(0)}[I_{2x}]_{0,n''} \end{aligned} \tag{4.20}$$

In a similar vein, the CSA Hamiltonian in the RF interaction frame is derived and expressed below.

$$\begin{aligned} \tilde{H}_{F,CSA} =& k\omega_1^{(m)}[I_{1z}]_{m,0} + k_1^{n'}\omega_1^{(m)}[I_{1z}]_{m,n'} + k_2^{n''}\omega_1^{(m)}[I_{1x}]_{m,n''} + \\ & k\omega_2^{(m)}[I_{2z}]_{m,0} + k_1^{n'}\omega_2^{(m)}[I_{2z}]_{m,n'} + k_2^{n''}\omega_2^{(m)}[I_{2x}]_{m,n''} \end{aligned} \tag{4.21}$$

ii. Dipolar Hamiltonian

Analogous to the description in the previous section, the dipolar Hamiltonian in the RF interaction has operators with Fourier indices associated with MAS and multiple pulse modulations. A brief description of this procedure is illustrated below.

$$\tilde{H}_{F,dip} = e^{i\lambda S_1} H_{F,dip} e^{-i\lambda S_1} \tag{4.22}$$

In the rotating frame, the dipolar Hamiltonian comprises of the $[I_{1z}I_{2z}]_{m,0}$, $[I_{1x}I_{2x}]_{m,0}$ and $[I_{1y}I_{2y}]_{m,0}$ operators. In the RF interaction frame, the $[I_{1y}I_{2y}]_{m,0}$ operators remain

invariant (since $\left[S_1, [I_{1y}I_{2y}]_{m,0}\right] = 0$), while the transformed $\widetilde{[I_{1z}I_{2z}]}_{m,0}$ and $\widetilde{[I_{1x}I_{2x}]}_{m,0}$ are evaluated by the procedure described below.

$$\begin{aligned}\widetilde{[I_{1z}I_{2z}]}_{m,0} =& e^{i\lambda S_1}[I_{1z}I_{2z}]_{m,0}e^{-i\lambda S_1}\\ =& kG_{ZZ}^{(m)}[I_{1z}I_{2z}]_{m,0} + k_1^{n'}G_{ZZ}^{(m)}[I_{1z}I_{2z}]_{m,n'} + k_2^{n''}G_{ZZ}^{(m)}\left\{[I_{1x}I_{2z}]_{m,n''} + [I_{1z}I_{2x}]_{m,n''}\right\}\end{aligned} \tag{4.23}$$

$$\begin{aligned}\widetilde{[I_{1x}I_{2x}]}_{m,0} =& e^{i\lambda S_1}[I_{1x}I_{2x}]_{m,0}e^{-i\lambda S_1}\\ =& kG_{XX}^{(m)}[I_{1x}I_{2x}]_{m,0} + k_1^{n'}G_{XX}^{(m)}[I_{1x}I_{2x}]_{m,n'} + k_2^{n''}G_{XX}^{(m)}\left\{[I_{1z}I_{2x}]_{m,n''} + [I_{1x}I_{2z}]_{m,n''}\right\}\end{aligned} \tag{4.24}$$

Combining these expressions, the dipolar Floquet Hamiltonian in the RF interaction frame is represented by,

$$\begin{aligned}\tilde{H}_{F,dip} =& e^{i\lambda S_1}H_{F,dip}e^{-i\lambda S_1}\\ =& k\left\{G_{ZZ}^{(m)}[I_{1z}I_{2z}]_{m,0} + G_{XX}^{(m)}[I_{1x}I_{2x}]_{m,0}\right\} + G_{YY}^{(m)}[I_{1y}I_{2y}]_{m,0} +\\ & k_1^{n'}\left\{G_{ZZ}^{(m)}[I_{1z}I_{2z}]_{m,n'} + G_{XX}^{(m)}[I_{1x}I_{2x}]_{m,n'}\right\} +\\ & k_2^{n''}\left(G_{ZZ}^{(m)} + G_{XX}^{(m)}\right)\left\{[I_{1x}I_{2z}]_{m,n''} + [I_{1z}I_{2x}]_{m,n''}\right\}\end{aligned} \tag{4.25}$$

The scaling factors involved in the chemical shift and dipolar interactions are identical. To derive the effective Hamiltonian, the internal Hamiltonian is diagonalized using the contact transformation procedure. Accordingly, the internal Hamiltonian is re-expressed as a sum of zero-order and perturbing Hamiltonians.

$$\begin{aligned}\tilde{H}_{F,\mathrm{int}} =& H_0 + H_1\\ H_0 =& \omega_r I_F^{(m)} + \omega_m I_F^{(n)} + k\omega_1^{(0)}[I_{1z}]_{0,0} + k\omega_2^{(0)}[I_{2z}]_{0,0}\\ H_1 =& \tilde{H}_{F,dip} + \tilde{H}_{F,CS} + \tilde{H}_{F,CSA}\end{aligned} \tag{4.26}$$

In the above equation, the scaled isotropic chemical shift (unmodulated) interaction is included along H_0. Employing a second transformation function S_2, the Floquet Hamiltonian in the RF interaction frame is diagonalized.

$$\tilde{H}_{F,\mathrm{int}}^{eff} = e^{i\lambda S_2}\tilde{H}_{F,\mathrm{int}}e^{-i\lambda S_2} \tag{4.27}$$

The form of the transformation function (S_2) is deduced by the following equation,

$$H_1^{(1)} = H_1 + i\left[S_2, H_0\right] \tag{4.28}$$

or in other words, $i\,[S_2, H_0] = -H_1$. To second-order, the corrections to the effective Hamiltonian are derived using the standard procedure described in the thesis.

$$H_2^{(1)} = \frac{i}{2}\,[S_2, H_1] \tag{4.29}$$

The form of the effective Hamiltonian and the expressions employed in the calculations are similar to those derived in chapter-2. The validity of the analytic description presented in this section is discussed through simulations in the following section.

4.4 Results and Discussion

To describe the higher-order R^2 phenomenon (N=3, 4), polarization transfer from I_1 to I_2 in the model systems (see Fig. 3.5 in chapter-3) is depicted in Fig. (4.2). In the simulations depicted, polarization transfer is monitored as a function of spinning frequency under constant mixing time. Since the re-introduction of the dipolar interactions result from a second order effect, the time required for polarization transfer is longer in comparison to first-order based R^2 experiments (N=1 & N=2). As depicted, the width of the resonance profile is significantly reduced in the higher-order R^2 matching profiles depicted in Figures 4.2 & 4.3. In contrast to first-order R^2 experiments, the orientation and magnitude of CSA tensors play an important role in the higher-order R^2 exchange dynamics. The simulations depicted in Fig. (4.3) highlight the role of CSA interactions and corroborate well with the analytic predictions described in the previous section. From an experimental perspective, the implementation of resonance width experiments at higher R^2 conditions seems less practical owing to the narrower width (see Figures 4.4 & 4.5) observed in the profiles. This is illustrated through Figures 4.4 & 4.5 wherein the R^2width profiles corresponding to the N=1, 2, 3 & 4 conditions are depicted. The decrease in width is more profound in the weak-coupling limit. Hence, mixing time experiments (Fig. 4.6) seem to be a better option for the implementation of higher-order R^2 experiments. Additionally, since the exchange trajectories (at higher R^2 matching conditions) are extremely sensitive to the magnitude and orientation (of chemical shift tensors) of the CSA interactions, prior knowledge of their magnitudes /orientations is essential. Hence, higher-order R^2 experiments seem to be of lesser utility in the measurement of interatomic distances in solids.

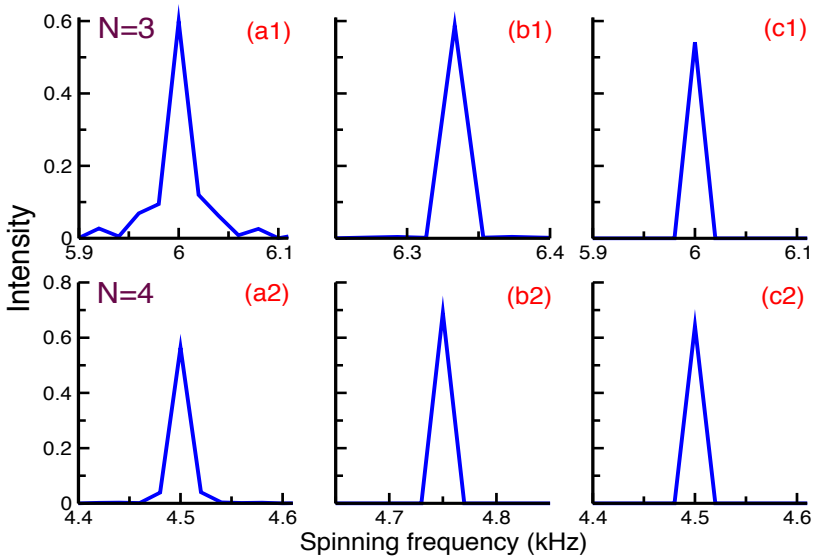

Figure 4.2: The figure depicts the spinning frequency dependent polarization transfer from V_{Co} to $V_{C\beta}$, 2.54 Å(a1, a2), from V_{Co} to $V_{C\gamma_1}$, 3.90 Å(b1, b2) and from Leu_{Co} to $V_{C\beta}$, 5.44 Å(c1, c2) represented in the model systems in figure 2.3. The analytic simulations in panels ((a1, Tmix=10ms), (b1, Tmix=80ms), (c1, Tmix=100ms)) represent the polarization exchange phenomenon for N=3 and the panels ((a2, Tmix=30ms), (b2, Tmix=100ms), (c2, Tmix=250ms)) for N=4, R^2 condition in a two-spin (C-C) system under constant mixing time. The analytic simulations are based on the Eqs. (2.17) & (2.18) in chapter-2. All the remaining simulation perimeters are given in Table 2.4 in Chapter 2.

As an alternative, multiple-pulse based techniques remain a better option for implementing higher-order R^2 experiments. In Figure 4.7, polarization transfer between spins based on the multiple-pulse scheme is depicted. Depending on the choice of the experimental parameters (spinning frequency, RF-offsets), both ZQ and DQ polarization transfer profiles are observed. As depicted, the efficiency of transfer is on par with the higher-order N=3, 4 R^2 matching conditions. Additionally, the polarization transfer takes place at a faster timescale. In the RF interaction frame, the isotropic chemical shifts are scaled resulting in modified resonance conditions. In addition to the dependence on the chemical shifts, the resonance conditions depend on the modulation frequency of the pulse sequence employed.

In the case of multiple-pulse based experiments, the resonance condition corresponds to $k\,(\omega_1 - \omega_2) = m\omega_r + n\omega_m$ (where $m = \pm 1, \pm 2$ and $n = \pm 1, \pm 2, \pm 3.....$), which in turn could also be expressed as $(\omega_1 - \omega_2) = k'\omega_r$ with k' being a real number.

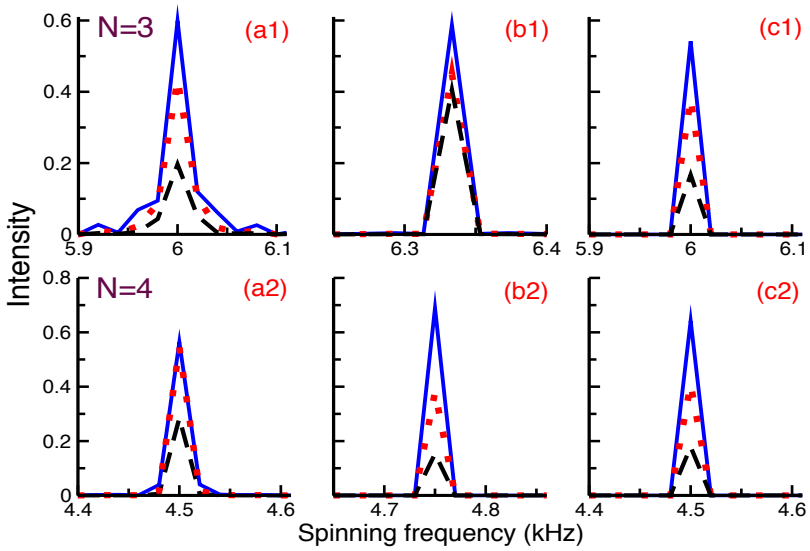

Figure 4.3: The figure depicts the CSA dependence of Carbonyl carbon in spinning frequency dependent polarization transfer from V_{Co} to $V_{C\beta}$, 2.54 Å (a1, a2), (δ_{Co}^{CSA}= -8589Hz), from V_{Co} to $V_{C\gamma_1}$, 3.90 Å (b1, b2), (δ_{Co}^{CSA}= 8589Hz) and from Leu_{Co} to $V_{C\beta}$, 5.44 Å (c1, c2), (δ_{Co}^{CSA}= -8500Hz) represented in the model systems in panels (a), (b) and (c) of figure 2.3, respectively. The magnitude of the CSA interactions are varied in all the simulations as the following: 100% (solid line), 60% (dotted line) and 30% (broken line). The simulations depicted in panels (a1, b1, c1) correspond to the N=3 condition, while the simulations correspond to the N=4 are illustrated in panels (a2, b2, c2). All the remaining simulation perimeters are given in Table 2.4.

Although, the efficiency of polarization transfer under fractional R^2 condition is promising, from a practical perspective, implementation of the scheme is very demanding owing to narrow resonance conditions. The resonance conditions are extremely sensitive to the precise setting of the sample spinning frequency. This aspect is highlighted in Fig. (4.10), through a set of simulations with wherein the mismatch in the spinning frequency about ± 25Hz. This trend is exhibited both in the strong and weak coupling regimes. The resonance conditions for a given sequence is determined only through precise evaluation of scaling factors based on higher-order (beyond second-order) perturbation theory. From a practical perspective, this extreme sensitivity to the spinning frequency, could be the main limiting factor in the implementation of fractional R^2 experiments in solid-state NMR.

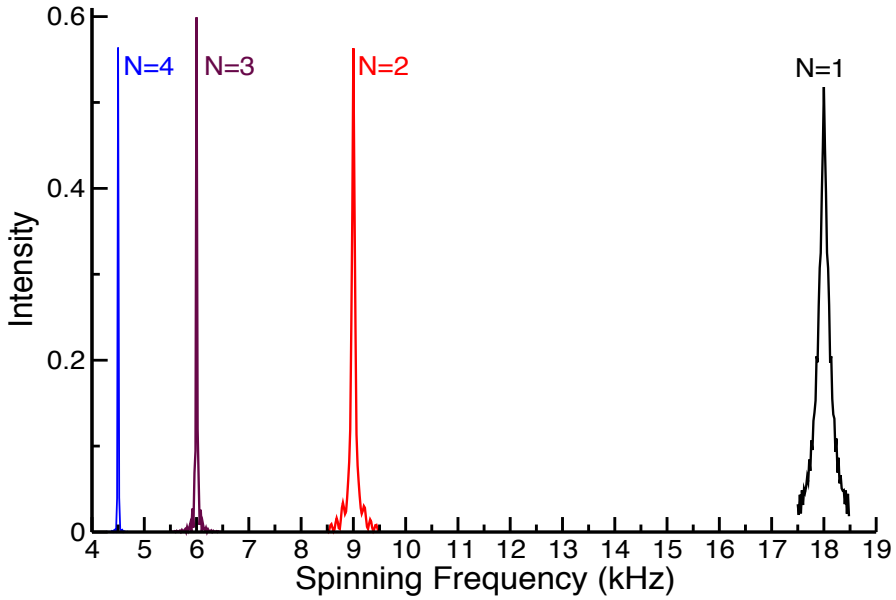

Figure 4.4: The figure depicts the spinning frequency dependent polarization transfer from valine carbonyl carbon to valine beta carbon ($V_{Co} \rightarrow V_{C\beta}$, 2.54 Å) in a two-spin (C-C) system under N=1, 2, 3 and 4, R^2 conditions.

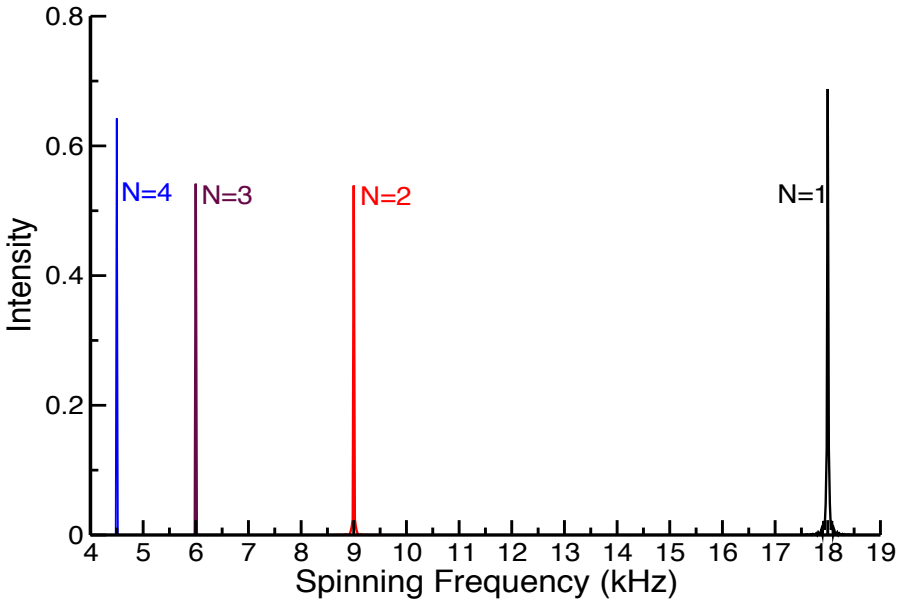

Figure 4.5: The figure depicts the spinning frequency dependent polarization transfer from leucine carbonyl carbon to valine beta carbon ($Leu_{Co} \rightarrow V_{C\beta}$, 5.44 Å) in a two-spin (C-C) system under N=1, 2, 3 and 4, R^2 conditions.

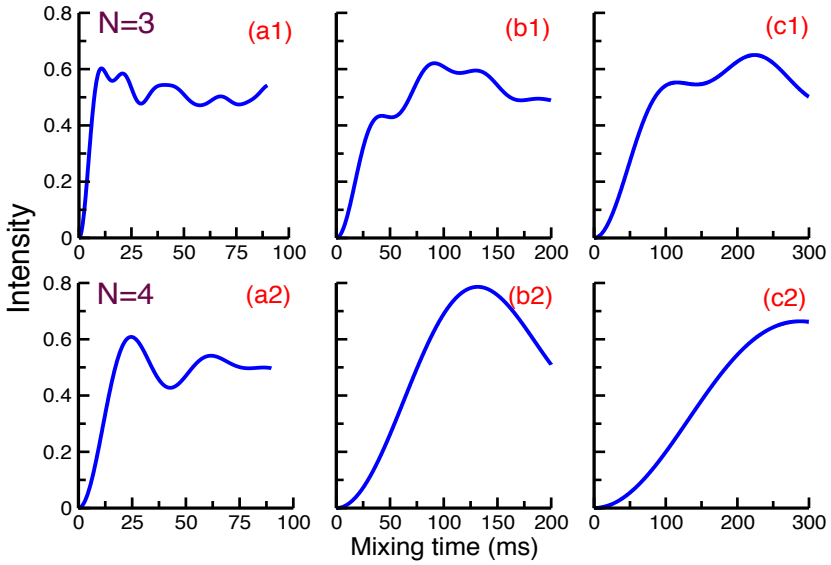

Figure 4.6: The figure depicts the mixing time dependent polarization transfer in the strong (V_{Co} to $V_{C\beta}$, 2.54 Å), medium (V_{Co} to $V_{C\gamma_1}$, 3.90 Å) and weak coupling (Leu_{Co} to $V_{C\beta}$, 5.44 Å) regimes in isolated two-spin systems under N=3 and N=4, R^2 conditions. All the remaining simulation perimeters are given in Table 2.4.

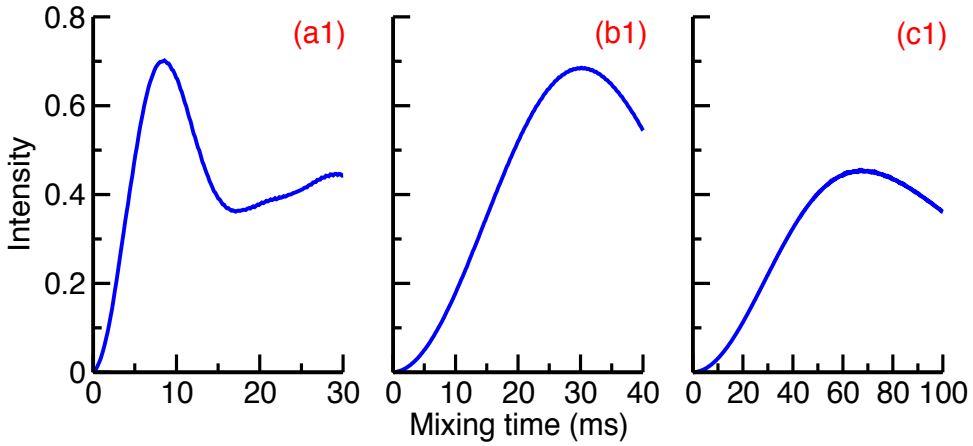

Figure 4.7: The figure depicts the polarization transfer from I_1 to I_2 ($V_{Co} \rightarrow V_{C\beta}$, 2.54 Å; panel a1), ($V_{Co} \rightarrow V_{C\gamma_1}$, 3.90 Å; pane b1) and ($Leu_{Co} \rightarrow V_{C\beta}$, 5.44 Å; panel c1) in two-spin systems under ZQ fractional R^2 conditions ((k'=3.144, $\beta = 270°$, $t_p = 15\mu s$, panel a1); (k'=3.1516, $\beta = 270°$, $t_p = 15\mu s$, panel b1) and (k'=3.144, $\beta = 270°$, $t_p = 15\mu s$, panel c1)) emerged from the multiple-pulse sequence (Figure 4.1) as a function of mixing time. All the remaining simulation perimeters are given in Table 2.4.

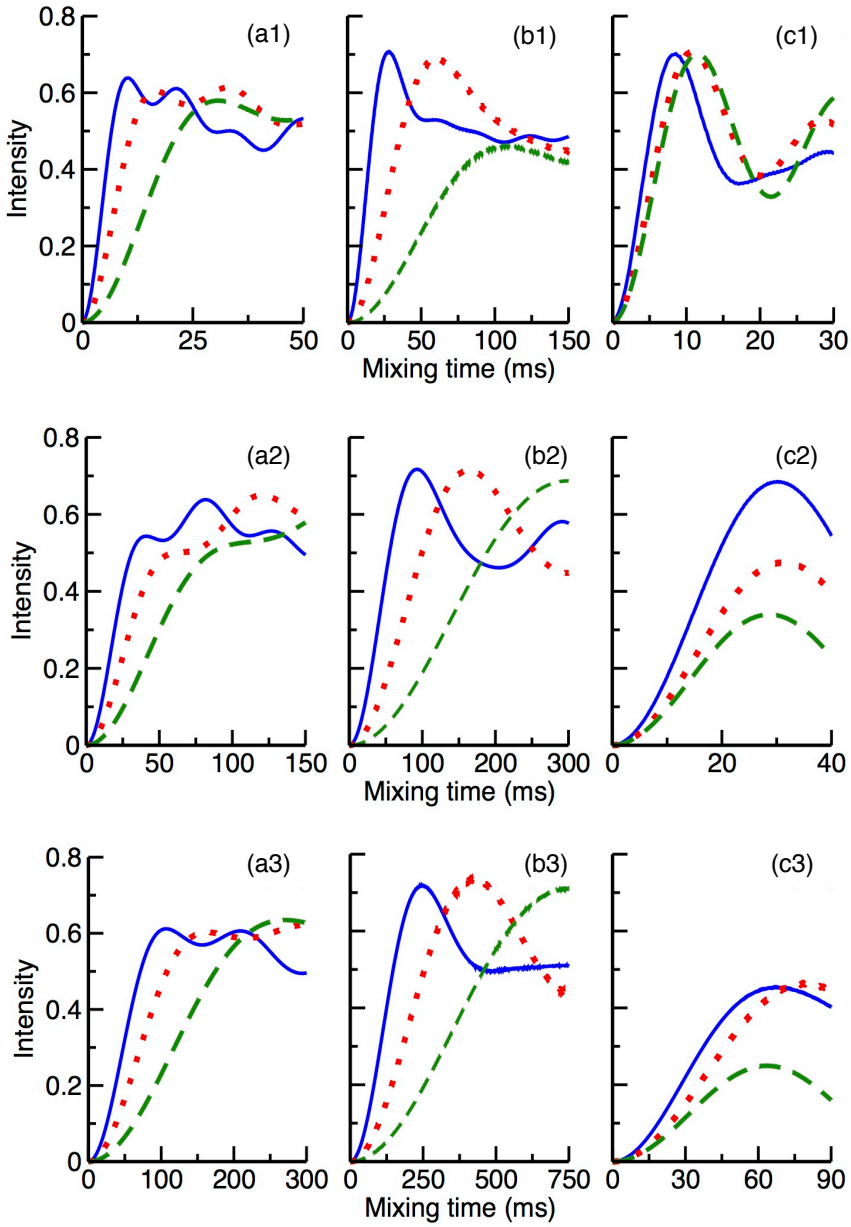

Figure 4.8: The figure depicts the role of the CSA interactions (CSA magnitude) in the polarization transfer from I_1 to I_2 ($V_{Co} \rightarrow V_{C\beta}$, 2.54 Å; panels (a1, b1, c1); δ_{Co}^{CSA}= -8589Hz), ($V_{Co} \rightarrow V_{C\gamma_1}$, 3.90 Å; panels (a2, b2, c2); δ_{Co}^{CSA}= 8589Hz) and ($Leu_{Co} \rightarrow V_{C\beta}$, 5.44 Å; panels (a3, b3, c3); δ_{Co}^{CSA}= -8500Hz) as a function of mixing time in two-spin systems under N=3 (a1, a2, a3), N=4 (b1, b2, b3) and fractional rotational resonance (k'=3.144, c1; k'=3.1516, c2; k'=3.144, c3) conditions. In the simulation depicted, the magnitude of the CSA interactions (carbonyl CSA) is varied as the following: 100% (solid line), 60% (dotted line) and 30% (broken line). All the remaining simulation perimeters are given in Table 2.4.

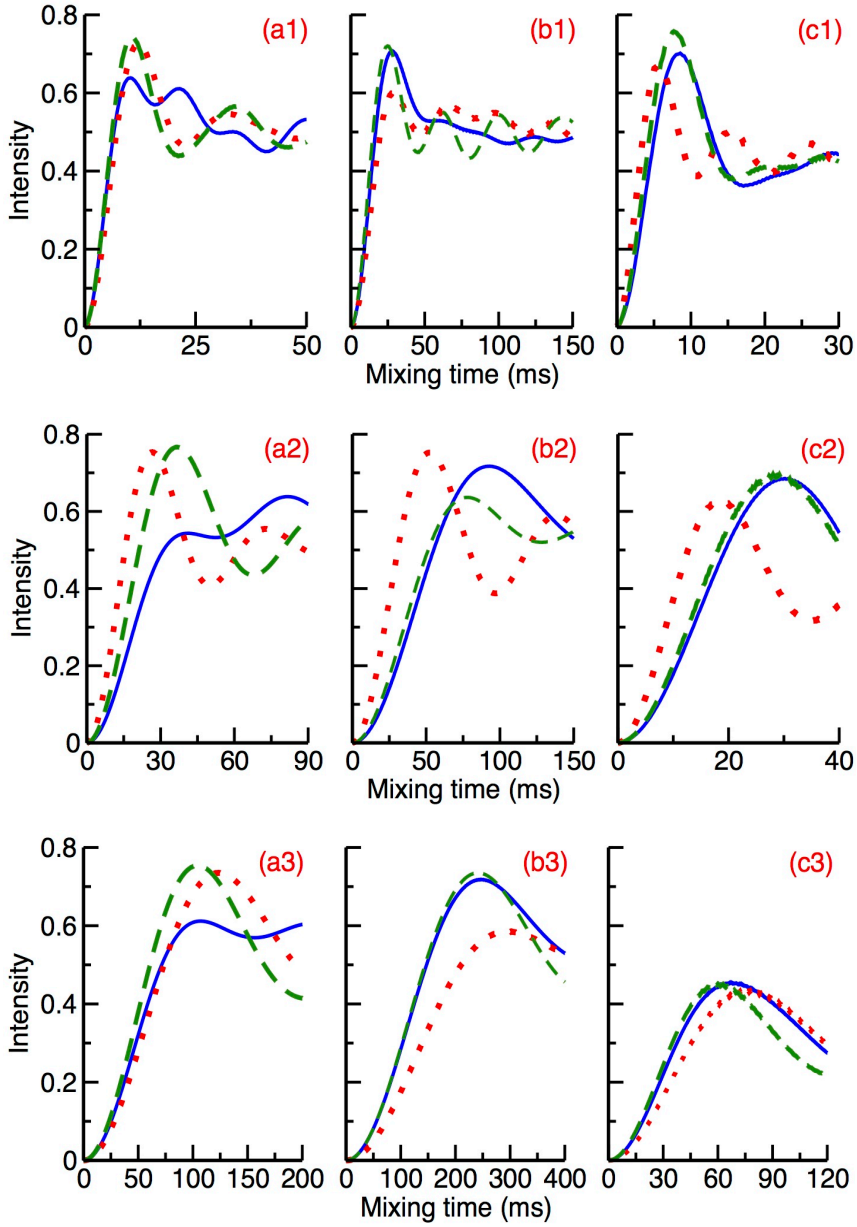

Figure 4.9: The figure depicts the role of the CSA interactions (CSA orientations) in the polarization transfer from I_1 to I_2 ($V_{Co} \rightarrow V_{C\beta}$, 2.54 Å; panels (a1, b1, c1)), ($V_{Co} \rightarrow V_{C\gamma_1}$, 3.90 Å; panels (a2, b2, c2)) and ($Leu_{Co} \rightarrow V_{C\beta}$, 5.44 Å; panels (a3, b3, c3)) as a function of mixing time in two-spin systems under N=3 (a1, a2, a3), N=4 (b1, b2, b3) and fractional rotational resonance (k'=3.144, c1; k'=3.1516, c2; k'=3.144, c3) conditions. In the simulations depicted, the CSA orientations (α, β, γ) of I_1 and I_2 are varied as the following: (0,0,0; 0,90,0)(dotted line), (0,90,0; 0,0,0) (broken line) and original (solid line). All the remaining simulation perimeters are given in Table 2.4.

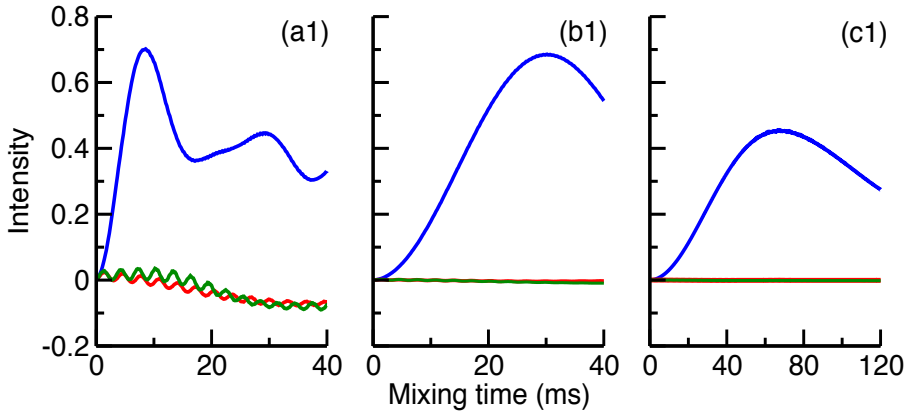

Figure 4.10: The figure depicts the role of the resonance condition in the polarization transfer from I_1 to I_2 in strong ($V_{Co} \rightarrow V_{C\beta}$, 2.54 Å; panel a1), medium ($V_{Co} \rightarrow V_{C\gamma_1}$, 3.90 Å; panel b1) and weak ($Leu_{Co} \rightarrow V_{C\beta}$, 5.44 Å; panel c1) coupling regimes under ZQ fractional R^2 conditions as a function of mixing time in two-spin systems. In all the panels, simulations correspond to the exact resonance (blue) conditions (k'=3.144, a1; k'=3.1516, b1; k'=3.144, c1) and with the mismatch in the spinning frequency about ± 25Hz (red, green) are depicted.

4.5 Conclusions

In summary, the analytic framework presented in this chapter is suitable for explaining the resonance conditions in higher-order and fractional based R^2 experiments. In contrast to first-order based R^2 experiments, the higher-order (N=3, 4) conditions are extremely sensitive to the CSA interactions (Figure 4.8 & 4.9). Although, multiple-pulse based R^2 experiments (or fractional R^2 conditions) have less dependence on the CSA interactions, precise setting of the spinning frequency seems to have a potential role in the efficiency of transfer. From a practical perspective, we believe that such schemes could be of limited potential when employed for distance measurements.

References

[1] K. Takegoshi, K. Nomura and T. Terao, *Chem. Phys. Lett.*, 1995, **232**, 424 – 428.

[2] K. Takegoshi, S. Nakamura and T. Terao, *Chem. Phys. Lett.*, 2001, **344**, 631 – 637.

[3] J. D. Ellett and J. S. Waugh, *J. Chem. Phys.*, 1969, **51**, 2851–2858.

[4] W. P. Aue, D. J. Ruben and R. G. Griffin, *J. Chem. Phys.*, 1984, **80**, 1729–1738.

[5] R. G. S. Spencer, K. W. Fishbein, M. H. Levitt and R. G. Griffin, *J. Chem. Phys.*, 1994, **100**, 5533–5545.

[6] G. Floquet, *Ann. Sci. Ecole Norm. Sup*, 1883, **12**, 47–89.

[7] J. H. Shirley, *Phys. Rev.*, 1965, **138**, 979–987.

[8] D. Zax, G. Goelman, D. Abramovich and S. Vega, in *Advances in Magnetic Resonance*, ed. W. S. Warren, Academic Press, 1990, vol. 14, pp. 219 – 240.

[9] S. Vega, *in Nuclear Magnetic Probes for Molecular Dynamics, edited by R. Tycko*, (Kluwer Academic, Amsterdam, 1994).

[10] S. Vega, *in Encyclopedia of NMR, edited by D. M. Grant and R. Harris*, (Wiley, New York, 1996).

[11] B. C. Filip, X. Filip, D. E. Demco and S. Hafner, *Mol. Phys.*, 1997, **92**, 757–772.

[12] R. Ramachandran and R. G. Griffin, *J. Chem. Phys.*, 2005, **122**, 164502.

[13] M. Leskes, P. Madhu and S. Vega, *Prog. Nucl. Magn. Reson. Spectrosc.*, 2010, **57**, 345 – 380.

[14] I. Scholz, J. D. van Beek and M. Ernst, *Solid State Nuclear Magnetic Resonance*, 2010, **37**, 39 – 59.

[15] R. Ramesh and M. S. Krishnan, *J. Chem. Phys.*, 2001, **114**, 5967–5973.

[16] E. Vinogradov, P. K. Madhu and S. Vega, *J. Chem. Phys.*, 2001, **115**, 8983–9000.

[17] D. Papousek and M. R. Aliev, *Molecular Vibrational-Rotational spectra*, Elsevier, Amsterdam, 1982.

[18] J. H. Van Vleck, *Phys. Rev.*, 1929, **33**, 467–506.

[19] M. Maricq and J. S. Waugh, *J. Chem. Phys.*, 1979, **70**, 3300–3316.

[20] M. M. Maricq, *Phys. Rev. B*, 1982, **25**, 6622–6632.

[21] M. M. Maricq, in *Advances in Magnetic Resonance*, ed. W. S. Warren, Academic Press, 1990, vol. 14, pp. 151 – 182.

[22] R. Ramachandran, J. R. Lewandowski, P. C. A. van der Wel and R. G. Griffin, *J. Chem. Phys.*, 2006, **124**, 214107.

Chapter 5

Summary and conclusions

In summary, an analytic framework integrating the concepts of effective Floquet Hamiltonians and the Reduced density matrix theory is proposed to account for the multi-spin effects observed in solid-state NMR experiments. Employing rotational resonance (R^2) experiments as a case study, the phenomenon of dipolar recoupling and the effects of depolarization arising from multi-spin interactions (mainly for $^{13}C-^{1}H$ dipolar interactions) are explained in terms of Rabi oscillations. To the best of our knowledge, no such descriptions exist in the literature. The theory presented in this thesis is well-suited to describe both homonuclear and heteronuclear dipolar recouping experiments in solid-state NMR. A brief summary of the problems addressed in thesis is presented in the following sections.

A. Description of R^2 phenomenon in terms of Rabi oscillations and Reduced density matrix theory.

To minimize the complexity in the description of spin dynamics in R^2 experiments, an analytic model based on the reduced density matrix theory is proposed to describe the magnetization exchange from spin I_1 to I_2. The effective Hamiltonian describing the magnetization exchange is derived from the contact transformation procedure.

$$H_{eff} = \sum_{i=1}^{2} A_i I_{iz} + \left[D_{12,PM} I_1^+ I_2^- + D_{12,MP} I_1^- I_2^+ \right] \tag{5.1}$$

The polarization transfer from spin I_1 to I_2 in R^2 experiments is described through the following equations.

$$\langle I_{1z}(t) \rangle = 1 - \frac{|D_{12}|^2}{x^2} \sin^2 xt \tag{5.2}$$

$$\langle I_{2z}(t)\rangle = \frac{|D_{12}|^2}{x^2}\sin^2 xt \tag{5.3}$$

The coefficient $x = \sqrt{|D_{12}|^2 + \left(\frac{(A_1-A_2)}{2}\right)^2}$, comprises of the dipolar and chemical-shift offset terms. The analytic expressions described above resemble to those derived by Rabi. In Fig. (5.1), the polarization transfer in the strong and weak coupling regimes in two-spin systems (from Figure 5.2) is presented both in single crystal and powder samples. The damping observed in the powder sample results from the interference effects arising from the different orientations present in a powder sample. Hence, phenomenological damping terms are not essential to observe the damping observed in real samples.

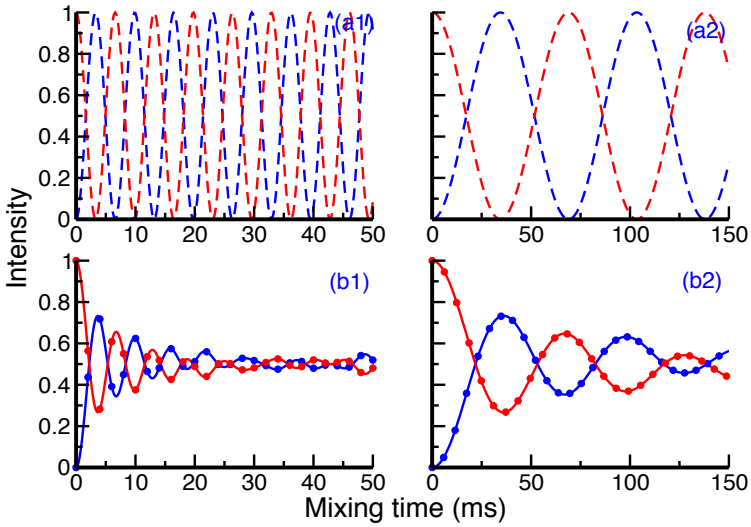

Figure 5.1: The figure depicts the polarization exchange between the carbons (C-C=2.54 Å: a1, b1) and (C-C=5.44 Å: a2, b2) as a function of mixing time in a two-spin (C-C) system. The panels (a1, a2) represent the polarization exchange without powder averaging (single crystal) and the panels (b1, b2) represent the polarization transfer with powder averaging (powder sample) under N=1, R^2 condition. The analytic simulations (dots) presented here are based on Eqs. 5.2 & 5.3.

B. Description of multi-spin effects in R^2 experiments.

To improve the accuracy of the estimated $^{13}C - ^{13}C$ distances from R^2 experiments, an analytic model based on reduced density matrix theory is proposed to describe the magnetization exchange between spins, I_1 & I_2 coupled to a bath of surrounding

protons. Employing a model system $I_1 - I_2 - S_N$, polarization transfer between spins

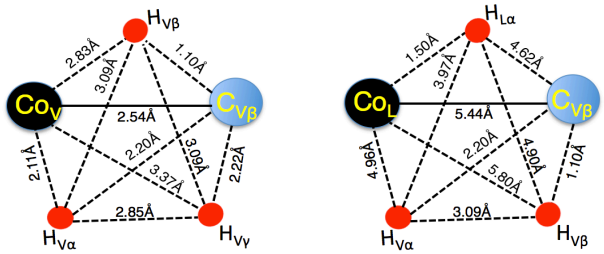

(a) (b)

Figure 5.2: The figure depicts the five-spin model systems correspond to the strong (Fig. a) and weak (Fig. b) C-C coupling regimes.

I_1 and I_2 in the presence of CW decoupling field is described in a reduced dimension through the expressions give below. The equations describing the polarization transfer resemble to those derived for an isolated spin pair and are computationally robust.

$$H_{eff} = \sum_{i=1}^{2} A_{I_i} I_{iz} + \left[D_{I_1 I_2, PM} I_1^+ I_2^- + D_{I_1 I_2, MP} I_1^- I_2^+ \right] + \sum_{i=1}^{2} \sum_{j=1}^{N} D_{I_i S_j} I_{iz} S_{jz} \tag{5.4}$$

$$\langle I_{1z}(t) \rangle = 1 - \frac{|D_{I_1 I_2}|^2}{(2)^{K-2}} \sum_{i=1}^{2^N} \frac{\sin^2 x_i t}{{x_i}^2} \tag{5.5}$$

$$\langle I_{2z}(t) \rangle = \frac{|D_{I_1 I_2}|^2}{(2)^{K-2}} \sum_{i=1}^{2^N} \frac{\sin^2 x_i t}{{x_i}^2} \tag{5.6}$$

As described in the above equations, for a system (K=total number of spins) comprising of N-protons, the 2^N 'x_i' coefficients have the following definitions with 'y_i' representing the heteronuclear dipolar ($^{13}C - {}^1H$) coefficients.

$$x_i = \sqrt{|D_{I_1 I_2}|^2 + \left(\frac{2(A_{I_1} - A_{I_2}) + y_i}{4} \right)^2} \tag{5.7}$$

The analytic expressions depicted in Eqs. 5.5 & 5.6 could be employed to fit experimental exchange curves employing multiple fit parameters such as $^{13}C - {}^{13}C$ distance, the orientation, magnitude of CSA tensors (both carbons and protons) and $^{13}C - {}^1H$ distances.

C. Effect of heteronuclear decoupling in R^2 experiments.

To improve the efficiency of transfer in R^2 experiments, an analytic theory based on effective Floquet Hamiltonians is proposed to elucidate the factors responsible for

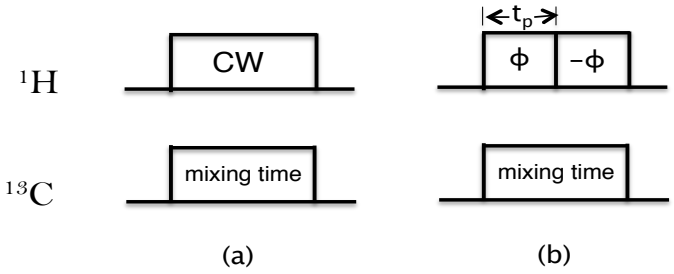

Figure 5.3: Schematic diagram depicting the CW (Fig. a) and TPPM (Fig. b) decoupling during the dipolar mixing time in R^2 experiments

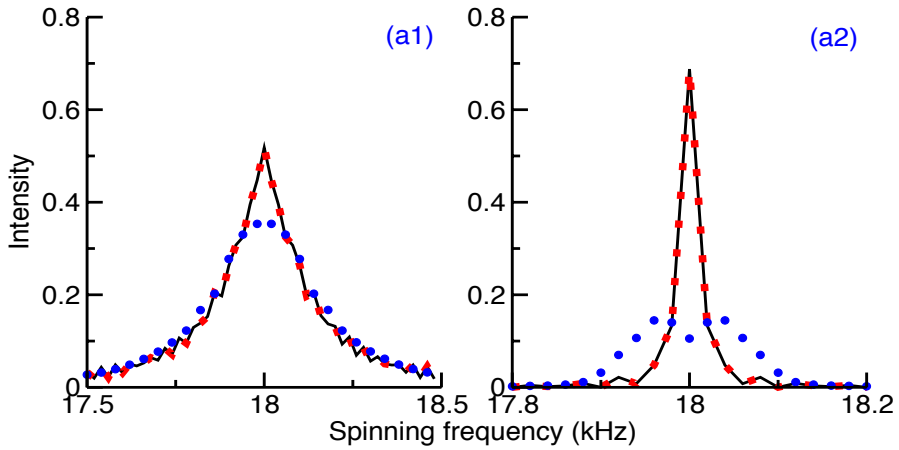

Figure 5.4: The figure depicts the polarization transfer from I_1 to I_2 (C-C=2.54 Å, a1) and (C-C=5.44 Å, a2) as a function spinning frequency in model five-spin systems depicted in Figure 5.2. The simulations depict the polarization transfer under CW (blue, circles) as and TPPM (solid line) decoupling schemes. For illustrative purposes, the polarization transfer in an isolated two-spin system (red, dots) is depicted in both the panels.

depolarization observed in R^2 experiments. In contrast to CW decoupling schemes, the improved transfer efficiency (see Fig. 5.4) observed in R^2 experiments in the presence of TPPM decoupling is explained through better compensation of second-order terms emerging from ^{1}H-CSA and $^{13}C-{}^{1}H$ dipolar interactions.

D. Description of higher-order and fractional R^2 experiments.

An analytic framework is presented to explain the reintroduction of dipolar interactions observed at higher-order (N=3, 4) R^2 matching conditions. The dependence of CSA interactions on the higher-order R^2 matching conditions is discussed in model systems with strong, medium and weak C-C coupling regimes. Employing Multi-

mode Floquet theory (MMFT), the phenomenon of fractional R^2 matching conditions observed in multiple-pulse based R^2 experiments (Fig. 5.5) is discussed and illustrated with few examples (FIg. 5.6). The optimum conditions required for the implementation of ZQ and DQ fractional R^2 experiments are discussed in terms of operators and are described elaborately.

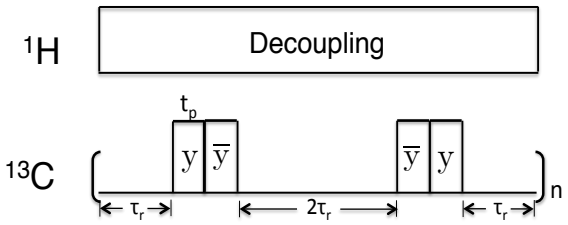

Figure 5.5: The schematic diagram depicting the multiple-pulse sequence employed for the implementation of fractional R^2 experiments.

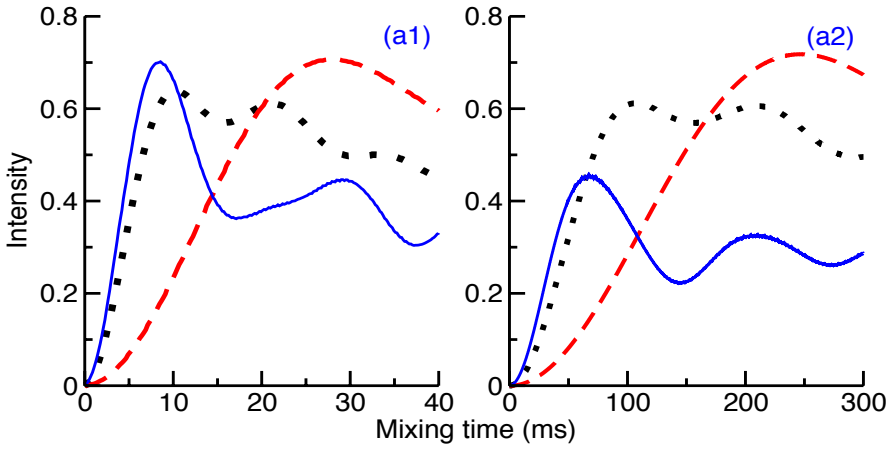

Figure 5.6: The figure depicts the polarization transfer from I_1 to I_2 (C-C=2.54 Å, a1) and (C-C=5.44 Å, a2) as a function of mixing time in two-spin systems. The simulations depicted in dotted line (N=3, black) and broken line (N=4, red) correspond to integer R^2 conditions, while solid line (k'=3.144, blue) denotes ZQ fractional rotational resonance.

We believe that the analytic theory presented in this thesis would be beneficial in improving the accuracy of $^{13}C - {}^{13}C$ distances estimated from R^2 experiments. Furthermore, the analytic framework should provide the necessary impetus for quantifying experiments involving broadband dipolar recouping experiments and would enable in the better design of SSNMR experiments.